UNIVERSITY OF MANITOBA

Magnetic Fields and Ultracold Neutron Production:

Studies Towards the Neutron Electric Dipole Moment Experiment at TRIUMF

by

Taraneh Andalib

A Thesis submitted to the Faculty of Graduate Studies of

The University of Manitoba

in partial fulfilment of the requirements of the degree of

Doctor of Philosophy

Department of Physics and Astronomy

University of Manitoba

Winnipeg

Abstract

The existence of a non-zero neutron electric dipole moment (nEDM) confirms the theoretical models of Physics beyond the Standard Model which provide extra sources of CP violation. Based on the Sakharov Criteria, CP violation is one of the main ingredients to create the baryon asymmetry in the universe. The current upper limit of the neutron EDM is 3.0×10^{-26} e·cm, which is below the theoretical model predictions. As a result, there is a worldwide quest to find a non-zero nEDM.

The typical experimental method to measure the nEDM uses ultracold neutrons (UCN) and employs the Ramsey method of separated oscillatory fields. In this method, the Larmor precession frequency of UCN is measured in the presence of aligned electric and magnetic field orientations. Such precision measurements require high UCN statistics and very stable and homogeneous magnetic fields. The work presented in this thesis is focused on the magnetic field and UCN studies for the future nEDM measurement at TRIUMF.

The TUCAN (TRIUMF UltraCold Advanced Neutron source) collaboration's goal is to measure the nEDM to the sensitivity of 10^{-27}. For this measurement, the < 1 pT magnetic stability requirement could be met by using magnetic shields with high magnetic permeability (μ) to reduce the external magnetic fields. However, external sources such as ambient temperature fluctuations could give rise to a change in the magnetic properties such as μ. The result of the temperature dependence of μ measurements and related simulations are presented here. These measurements set a limit on the temperature control level for the future nEDM measurement at TRIUMF.

The TUCAN collaboration's goal is to design a next-generation UCN source to in-

crease the UCN statistics and reach the required nEDM sensitivity. In 2016, the vertical UCN source that was previously developed at RCNP was shipped to TRIUMF. In early 2017, we significantly improved the control system for data acquisition. In November 2017, the first UCN experiments were conducted with the source. The status of the current UCN facility at TRIUMF and the result of the first UCN production tests are presented here.

Contents

List of Figures

List of Tables

Chapter 1

Introduction

The work presented in this thesis is focused on two important factors for successfully measuring the neutron electric dipole moment (nEDM) at TRIUMF: a very stable magnetic field environment, and high ultracold neutron (UCN) statistics. The TRIUMF Advanced Ultracold Neutron source (TUCAN) collaboration's goal is to measure the nEDM to the 10^{-27} e·cm sensitivity level.

This chapter provides some information on the interest in the nEDM measurement from a physics perspective. Finding a nonzero nEDM would provide a mechanism to explain the matter-antimatter or baryon asymmetry of the universe. The nEDM measurement method and a brief overview of the UCN and nEDM facilities worldwide are also presented here. Chapter 2 gives a description of the future nEDM measurement at TRIUMF and its experimental setup. Chapter 3 is focused on work towards the temperature dependence of magnetic permeability μ, needed to define the temperature stability requirements for the nEDM measurement. Chapter 4 presents the current UCN facility at TRIUMF, where the first UCN were produced with the vertical UCN source. Chapter 5 presents the result of those measurements with UCN. The final remarks and notes are available in Chapter 6.

1.1 History of Fundamental Symmetries

Studies of discrete symmetries have revealed interactions of the elementary particles and helped develop the underlying theories. There are three discrete symmetries in physics: charge conjugation (C), parity (P) and time-reversal (T). C-symmetry simply describes a particle-antiparticle transformation. Parity transformation is simply the inversion of spatial coordinates, and time-reversal transformation is changing the arrow of time. Tests of C, P and T symmetries helped establish the structure of the Standard Model (SM) [1]. The Standard Model of particle physics is a theory that describes how fundamental particles interact with three of the four fundamental fources: electromagnetism, weak and strong interactions.

In 1956, symmetry breaking started with the famous $\theta-\tau$ paradox in K-meson decay. The paradox was that two particles previously known as θ^+ and τ^+, which had the same mass and lifetime, decayed into products with different parities (the intrinsic parity of pion is -1 and it is a multiplicative quantum number. Therefore, the parity of the first interaction is +1 and for the second interaction is -1)

$$\begin{aligned} \theta^+ &\rightarrow \pi^+ + \pi^0 \\ \tau^+ &\rightarrow \pi^+ + \pi^+ + \pi^- \ . \end{aligned} \tag{1.1}$$

At first, it was assumed that the initial states should also have different parities (while all other physical properties were the same) but, precise measurements revealed that this is not the case. Yang and Lee suggested that the paradox originated from P violation in the weak interactions [2]. Immediately after, an experimental search was suggested for Parity violation in the β decay of Co-60. Within a few months, P violation was demonstrated by three different experiments [3–5]. After the observation of P violation, Landau showed that electric dipole moments (EDMs) are forbidden by T symmetry [6], and it was suggested that T symmetry should also be checked experimentally [7].

The fundamental CPT theorem in physics states that the sequential operation of C, P and T leave the system unchanged in quantum field theories. To date, there is

no experimental evidence for CPT symmetry breaking. Because of CPT invariance, breakdown of CP symmetry is equivalent to violation of time-reversal symmetry.

A non-zero neutron EDM may exist if parity and time-reversal symmetries are violated. There are two sources of CP violation in the Standard Model: in the CKM (Cabibbo-Kobayashi-Maskawa quark mixing matrix) matrix, and a CP-violating term in the QCD Lagrangian. The CKM contribution to the nEDM occurs in higher order and predicts $d_n \sim 10^{-31}$ e·cm. Furthermore it cannot explain the observed baryon asymmetry of the universe (see Section 1.2). The CP-violating term in the QCD Lagrangian contains a dimensionless parameter θ which is constrained to be small by nEDM measurements. This is discussed further in Section 1.3.

Beyond the Standard Model (BSM) theories provide extra sources of CP violation. The nEDM rising from these theories is in the range of $10^{-25} - 10^{-28}$ e·cm [1]. Although occurring at a higher energy scale than the CKM contributions, these sources can contribute in leading order, giving rise to a larger contribution. This is also mentioned briefly in Section 1.3

The search for EDMs can be traced back to 1950, when Purcell and Ramsey tested the possibility of finding EDMs for particles and nuclei [8]. Smith, Purcell and Ramsey performed an experiment to search for the neutron EDM d_n, and they achieved the upper limit of $d_n < 5 \times 10^{-20}$ e $\cdot$ cm [9]. Over the years, the upper limit on the neutron EDM has been improved by many orders of magnitude (see Section 1.11). Measurement of particle EDMs provide some of the tightest constraints on the extensions to the Standard Model providing CP violation. The most recent upper limit on the neutron EDM is $|d_n| < 3.0 \times 10^{-26}$ e· cm [10, 11].

1.2 Baryon Asymmetry of the Universe

The neutron EDM provides a highly sensitive measurement for CP violation [1, 12], which is an important element for the observed baryon asymmetry in the universe (see Sakharov criteria below). The dominance of matter over antimatter in the universe can

be characterized by [13]

$$\eta = \frac{n_b - \bar{n_b}}{n_\gamma} \simeq 6 \times 10^{-10} \tag{1.2}$$

where n_b is the number of baryons, $\bar{n_b}$ is the number of anti-baryons, and n_γ is the number of photons in the cosmic microwave background.

It is plausible to assume that the universe is baryon symmetric in a very large scale, and it is split into regions that are made of only baryons or anti-baryons. But, even in the least dense regions of the space, there are hydrogen gas clouds. So if there were regions of only baryon or anti-baryons in the universe, an excess of gamma rays in between these separated regions would be expected, due to annihilation. Since this is not observed, it might indicate that these regions are as large as the scale of the observed universe. Howerve, there is no plausible way of separating baryon and anti-baryons in such large scales [13].

Sakharov Criteria

There are three key ingredients needed in a theory to create a baryon asymmetry, known as the Sakharov criteria [14]:

- Baryon number violation
- C and CP violation
- Departure from the thermal equilibrium.

If the baryon number is conserved in each reaction, then it will always be conserved globally. Therefore there must be a reaction such as

$$X \to Y + B \ , \tag{1.3}$$

where the net baryon number is $B > 0$. Here the baryon number for X and Y are zero and B is the excess baryons.

If symmetric under C, the rate for the C-conjugation process $\bar{X} \to \bar{Y} + \bar{B}$ to happen is the same

$$\Gamma(X \to Y + B) = \Gamma(\bar{X} \to \bar{Y} + \bar{B}) \ . \tag{1.4}$$

Since the rate is the same, the net baryon number would be zero over long periods of time. However, C violation by itself is not enough and we need CP violation. To see this, consider X decaying to two left-handed or right-handed particles

$$X \to q_L q_L \ \ , \ \ X \to q_R q_R \ . \tag{1.5}$$

Under CP, $q_L \to \bar{q_R}$ and under C-conjugation $q_L \to \bar{q_L}$. Even though under C violation we have

$$\Gamma(X \to q_L q_L) \neq \Gamma(\bar{X} \to \bar{q_L}\bar{q_L}) \ , \tag{1.6}$$

under CP conservation we get

$$\Gamma(X \to q_L q_L) + \Gamma(X \to q_R q_R) = \Gamma(\bar{X} \to \bar{q_R}\bar{q_R}) + \Gamma(\bar{X} \to \bar{q_L}\bar{q_L}) \ . \tag{1.7}$$

Therefore, to get non-zero net baryon number,CP should be violated as well.

If the system is in thermal equilibrium we would have

$$\Gamma(X \to Y + B) = \Gamma(Y + B \to X) \ . \tag{1.8}$$

Therefore, the inverse process will destroy the excess baryon number created, and so a departure from thermal equilibrium is required.

1.3 CP violation Beyond the Standard Model

A testable scenario to create the baryon asymmetry in the universe is Electroweak Baryogenesis (EWBG) [15]. The initial condition for this process is a hot radiation-dominated early universe with zero net baryon number. This scenario requires a first-order electroweak phase transition in order to form bubbles of broken electroweak phase that nu-

cleate within the surrounding plasma. The baryon asymmetry is generated near the walls of these expanding bubbles.

EWBG satisfies all Sakharov criteria using processes that are naively permitted in the Standard Model. However, there are two problems with this model: the first-order phase transition is not strong enough, and it does not provide enough CP violation to create the baryon asymmetry currently observed in the universe [16]. As a result, beyond the Standard Model physics is necessary, such as Minimal Supersymmetric Standard Model (MSSM) [17].

Supersymmetry (SUSY) is a symmetry under the interchange of bosonic and fermionic degrees of freedom. In MSSM, for each particle, a superpartner is introduced with spin differing by a half unit. In SUSY breaking, the masses of the superpartners can be large (at the TeV scale), thereby explaining why they have not yet been observed. The motivation for postulating the existence of the superpartners is that corrections to the Higgs mass from the SM particles and their superpartners cancel [18].

New CP-violating phases may also appear in SUSY models. These sources would give contributions to the nEDM at 1-loop order and hence the contributions are potentially quite large. The fact that such sources have not been observed already indicates that these phases must be relatively small (for superpartner masses at the TeV scale). This is known as the SUSY CP problem, since a priori the phases could have any value [18].

The CP symmetry may be violated in QCD. The QCD Lagrangian consists of two terms

$$\mathscr{L} = \mathscr{L}_{cp} - \theta \frac{n_f g^2}{32\pi^2} F_{\mu\nu} \tilde{F}^{\mu\nu} \ , \tag{1.9}$$

where the first term is CP conserving and the second is CP violating with an angular parameter θ. Here $F_{\mu\nu} = \partial_\mu A_\nu + \partial_\mu A_\nu + i[A_\mu, A_\nu]$, and $\tilde{F}^{\mu\nu} = 1/2\epsilon^{\mu\nu\alpha\beta} F_{\alpha\beta}$ are the gluon field strength tensor and dual field strength tensor respectively. The first term $\mathscr{L}_{cp}$ describes the gluons, quarks, and their interaction, and the second term describes the interaction of the gluons with vacuum. The existing strong bound on the nEDM (3×10^{-26} e·cm) requires the angle θ to be very small ($\theta < 10^{-9}$). Since θ is dimensionless, it would be natural to have a value of order unity. The discrepancy between the measured

value (essentially zero) and the natural expectation (unity) is known as the the "Strong CP problem".

A solution to the strong CP problem was proposed by Peccei and Quinn [19]. They proposed a new symmetry to explain the CP conservation of strong interactions, which in turn predicts a new particle named the axion. To date the axion has never been discovered although there is still a strong link between axion and nEDM experiments. For example, there are theories that predict an oscillating value of the neutron EDM could be caused by the presence of the axion [20]. If θ is found to be small but non-zero, it is possible that it could be generated by dynamical processes from BSM physics [1].

1.4 Neutron Electric Dipole Moment and Symmetry Breaking

A very intuitive way of describing the neutron EDM is to think of it as the separation of the positive and negative charges along its spin axis. However, those charges add to zero since neutron is not a charged particle. Experiments already limit this separation to be very small as the current upper limit for nEDM is 3×10^{-26} e·cm as previously stated. The interaction of the EDM of a spin-1/2 particle with spinor ψ with the electromagnetic field $F^{\mu\nu}$, with a magnetic moment μ_n, and an electric dipole moment d_n can be written as a relativistic invariant [21]:

$$H_d = \frac{d_n}{2}\bar{\psi}\gamma_5\sigma_{\mu\nu}\psi F^{\mu\nu} \ , \tag{1.10}$$

where γ_5 and $\sigma_{\mu\nu}$ are related to γ matrices. Similarly, the interaction of a magnetic moment with the electromagnetic field is given by

$$H_\mu = \frac{\mu_n}{2}\bar{\psi}i\sigma_{\mu\nu}\psi F^{\mu\nu} \ . \tag{1.11}$$

In the nonrelativistic limit, the sum of these contributions to the hamiltonian is

$$H = -\mu_n \frac{\mathbf{J}}{J} \cdot \mathbf{B} - d_n \frac{\mathbf{J}}{J} \cdot \mathbf{E}. \tag{1.12}$$

The fact that $\mathbf{d_n}$ must point along $\mathbf{J}$ (the form of Eqns. 1.10 and 1.12) may be argued from the Wigner-Eckart theorem [22].

The properties of the Hamiltonian (Eqn. 1.12) under discrete symmetries are summarized in Table 1.1. Based on this, the first term is CP-even and T-even, and the second term is CP-odd and T-odd. The fact that both terms are even under CPT is a consequence of the CPT theorem. Furthermore, the EDM term in Equation 1.12 is P-odd. A nonzero EDM implies that both parity and time-reversal symmetries are broken, and through the CPT theorem (or quantum field theories in general) that CP symmetry is broken.

	C	P	T
B	-	+	-
E	-	-	+
$\boldsymbol{\mu_n}$	-	+	-
$\mathbf{d}_n$	-	+	-

Table 1.1: Symmetry properties of different components of the EDM Hamiltonian

1.5 Ultracold Neutrons

The nEDM measurement technique and a brief survey of nEDM measurements conducted worldwide are presented in this chapter. Ultracold neutrons are the main tool in the measurement of nEDM and their properties are discussed below.

Table 1.2 shows vaious energy regimes of neutrons, their corresponding velocities, and de Broglie wavelengths which are related via

$$E = \frac{1}{2} m_n v^2 = \frac{h^2}{2 m_n \lambda^2} \ , \tag{1.13}$$

where m_n is the mass of the neutron, v is the neutron velocity, h is the Planck's constant, and λ is the de Broglie wavelength.

Neutrons	Energy range E	Velocity v [m/s]	Wavelength λ [Å]
Fast	>0.8 MeV	$>12.3\times10^6$	<0.0003
Intermediate	1 eV - 0.8 MeV	13.8×10^3- 12.3×10^6	0.0003-0.28
Epithermal	100 meV - 1 eV	4374 - 13.8×10^3	0.9 - 0.28
Thermal	12 meV - 100 meV	1515 - 4374	2.6 - 0.9
Cold	0.12 meV - 12 meV	152 – 1515	26.1 - 2.6
Very cold	300 neV - 0.12 meV	7.5 - 152	52.2 – 26.1
Ultracold	≤300 neV	≤8	≥500

Table 1.2: Commonly used names for neutrons in different energy ranges and their corresponding velocity and wavelength

Ultracold neutrons are neutrons with kinetic energies $\lesssim$ 300 neV, corresponding to velocities $\lesssim$ 8 m/s. UCN move so slowly that they reflect from the surfaces of materials. Each material has an optical potential for neutrons whose value depends on the neutron-nucleus interaction (see Section 1.5.4). The largest of these is for ^{58}Ni and the value of the neutron optical potential in this case is 335 neV, dependent on the density of the material. This defines the typically upper limit on the UCN energy. With this low energy, UCN can populate traps made of matter, magnetic, and gravitational fields, and can be stored and manipulated for several hundreds of seconds in such traps. Because of their properties, UCN are a valuable tool for precise measurements in fundamental physics.

High precision studies of UCN and their interactions provide important data for particle physics and cosmology. In addition, they enable sensitive searches for new physics. Examples of the experiments using UCN, which aim to discover new physics, are searches for a permanent EDM of the neutron [10, 23–26], precision measurements of the neutron lifetime [27–32], and β-decay correlation parameters [33–35], as well as quests for dark matter candidates [36, 37], axion-like particles [38–40], Lorentz invariance violations [41], and the measurements of the quantum states of UCN in the gravitational field of the Earth [42].

The neutron is an electrically neutral hadron, and it participates in all four fundamental interactions which are described below.

1.5.1 The Gravitational Interaction

A neutron has a mass of $m_n \approx 940$ MeV/c^2, and therefore, it has a potential in the Earth's gravitational field as

$$V_g = m_n g h \ . \tag{1.14}$$

Here h is the vertical displacement, and $g = 9.8$ m/s^2 is the acceleration due to the Earth's gravitational field. In experiments using thermal or cold neutrons, the effects of gravity can usually be neglected due to the large kinetic energies of the neutrons. However, with the UCN experiments, since they have such low kinetic energy, gravity has a significant influence.

Here

$$mg = 102 \text{ neV/m} \ , \tag{1.15}$$

which is comparable to the UCN kinetic energy for human-scale traps. This means, a UCN of energy 200 neV can rise by at most 2 m.

1.5.2 The Weak Interaction

The weak interaction governs the radioactive β-decay of neutrons. A neutron decays into a proton, an electron, and an electron antineutrino via exchange of W^-

$$n \longrightarrow p + e^- + \bar{\nu_e} \ . \tag{1.16}$$

The value of the neutron lifetime sets the upper limit for UCN storage times. The current value of the neutron lifetime is 880.2 ± 1.0 s [43] which is comparable to trapping times for UCN. This sets the ultimate upper bound on the experiment measurement cycle time scale (see section 1.6.1).

1.5.3 The Electromagnetic Interaction

Neutrons are electrically neutral, spin-1/2 particles that possesses a magnetic dipole moment due to their internal structure, through which they interact with a magnetic

field **B**. This interaction is described by the first part of the Eqn. 1.12:

$$H_B = V_m = -\boldsymbol{\mu}_n \cdot \mathbf{B} \ . \tag{1.17}$$

where, for neutrons

$$|\boldsymbol{\mu}_n| = 60.3 \text{ neV/T} \ . \tag{1.18}$$

In an inhomogeneous magnetic field, UCN experience a force described by

$$\mathbf{F}_m = -\boldsymbol{\nabla} V_m = \pm|\boldsymbol{\mu}_n|\boldsymbol{\nabla}\mathbf{B} \ . \tag{1.19}$$

The last equal sign in the equation above is only true for an adiabatic case where the neutrons are moving so slowly that their magnetic moment is always in the same direction as the magnetic field. This will happen when the changes of the inhomogeneous magnetic field over time in the rest frame of the neutron is much slower than the neutron's Larmor precession frequency ω_L as described by

$$\omega_L \gg \frac{\frac{d\mathbf{B}}{dt}}{\mathbf{B}} \ . \tag{1.20}$$

The Larmor precession is the precession of the neutron's magnetic moment around the applied external magnetic field (see section 1.8). Since UCN move very slowly, this condition is easily fulfilled.

In Eqn. 1.19, the sign $\pm$ corresponds to the relative orientation between the magnetic moment and the magnetic field. UCN of anti-parallel spin to the magnetic field (magnetic moment parallel) are accelerated into the magnetic field with the force $\mathbf{F}_m = |\boldsymbol{\mu}_n|\boldsymbol{\nabla}\mathbf{B}$ and are therefore called "high field seekers". UCN with parallel spin (and thus magnetic moment anti-parallel) to the magnetic field, are called "low field seekers".

In our nEDM measurements, the interaction of UCN with the magnetic field is used to polarize UCN, and to measure their polarization at the end of the measurement cycle (see Section 1.9). Polarization can be achieved by passing the UCN through a strong ~ 6 T magnetic field. In such magnetic field, the magnetic potential would be about 360 neV

which is large enough to prevent the passage of low-field seekers. High-field seekers, on the other hand, may pass, resulting in highly polarized UCN after passage through the magnetic field region. It is important during this process that the UCN spins adiabatically track the magnetic field so that erroneous spin-flips do not occur which would reduce the polarization achieved.

1.5.4 The Strong Interaction

Neutrons and protons are bound in the nucleus by the strong interaction. However, this interaction has a short range, and it only a effects the neighbouring nuclei. Fermi realized that it is possible to introduce an effective potential $V(\mathbf{r}) \sim \delta(\mathbf{r})$ which can be used to calculate the small changes in the wavefunction outside the range of the interaction by perturbation theory. This approximation works in the limit that the neutron wavelength λ is much larger than the range of the neutron-nucleus potential.

The scattering of a neutron from a nucleus can be described as a superposition of an incoming plane wave and a scattered spherical wave:

$$\psi(r,\theta) = e^{ikr} + f(\theta)\frac{e^{ikr}}{r} \ , \tag{1.21}$$

where $f(\theta)$ is the angle dependent scattering amplitude and is determined by the boundary condition at $r = R$. Since the wavelength of the UCN is much larger than the range of the strong interaction R, there is no angular momentum transfer, and the process is dominated by the s-wave ($l = 0$) scattering. In this case, the scattering amplitude f does not depend on the incident angle

$$f(\theta) = const. = -a \ . \tag{1.22}$$

The differential cross-section is then given by $\frac{d\sigma}{d\Omega} = |f(\theta)|^2 = a^2$, where a is the scattering length, a quantity that can be experimentally measured.

The interaction of an incident neutron with a nucleus can be replaced with a suitable potential that produces the same scattering length, and as mentioned earlier, the Fermi

potential, proportional to a single delta-function [44] is a suitable choice:

$$V(\mathbf{r}) = \frac{2\pi\hbar^2}{m_n} a\delta^{(3)}(\mathbf{r}) \ , \tag{1.23}$$

where m_n is the mass of neutron, and a is the scattering length. Therefore, the interaction of an incident neutron with a liquid or a solid can be described by sum of equivalent δ functions

$$V(\mathbf{r}) = \frac{2\pi\hbar^2}{m_n} \sum_i a_i \delta(\mathbf{r} - \mathbf{r_i}) \ , \tag{1.24}$$

where r_i is the position of the ith nucleus, a_i is the scattering length with the ith nucleus, and the sum is over all the nuclei. This is the Fermi pseudopotential. Since UCN have a large wavelength compared to the atomic spacing, this equation can be written as

$$V(\mathbf{r}) = \frac{2\pi\hbar^2}{m_n} \sum_{\text{domain } i} N_i a_i \Theta_i(\mathbf{r}) \ , \tag{1.25}$$

where $\theta_i(\mathbf{r})$ is one when $\mathbf{r}$ is within the region (domain) of material i. Here the sum is over the domains of nuclei with the same scattering length a_i and uniform density N_i. In neutron physics, this potential is typically called the neutron optical potential, since if the energy of the neutron is less than the optical potential $E < V$, the neutron will be fully reflected from the material surface under any angle of incidence. This sets an upper limit on the UCN velocity.

UCN can be lost when reflected from the material walls. This can be due to the upscattering in which UCN absorb energy, or absorption in which UCN get captured by a nucleus in the reflecting material. To include these losses in the potential, the optical potential is usually written as a complex potential given by

$$U(r) = V(r) - iW(r) \ . \tag{1.26}$$

If we solve the Schrödinger equation with this potential including losses (as compared to solving while considering only $V(r)$), we get an additional decay of probability density as

$$\rho = \rho_0 e^{-2Wt/\hbar} \ . \tag{1.27}$$

We set

$$W(\mathbf{r}) = \frac{\hbar}{2} \sum_{\text{domain } i} N_i \sigma_l^i v \Theta_i(\mathbf{r}) \tag{1.28}$$

with N_i being the number density in the material i, σ_l^i being the loss cross-section (absorption plus inelastic scattering) of material i, and $v = \frac{\hbar k}{m_n}$ being the neutron velocity. Therefore we get a correct description of absorption

$$1/\tau_{abs} = 2W/\hbar = \sum_i N_i \sigma_l^i v \Theta_i(\mathbf{r}) \ . \tag{1.29}$$

Comparing Eqn. 1.25, and 1.28 and writing for one domain with a homogeneous material with all the same nuclei in it , Eqn. 1.26 becomes

$$U = V - iW = \frac{2\pi\hbar}{m_n} N(a_r - ia_i)\Theta_i(\mathbf{r}) \ , \tag{1.30}$$

where a_r is the real part of the scattering length and $a_i = \frac{\sigma_l k}{4\pi}$ is the imaginary part of the scattering length. The ratio $f = \frac{W}{V} = \frac{\sigma_l k}{4\pi a_r}$ is the UCN loss coefficient, where as earlier, σ_l is the total loss cross-section for neutrons with wavenumber k, and a is the scattering length [44].

For almost all materials $V \gg W$. The total energy of UCN satisfies $E < V$ for many materials and therefore, they are reflected from material surfaces at all angles of incidence. For $V > E$, the mean probability of neutron loss on reflection from an abrupt potential step ($V \gg W$), averaged over all angles of incidence, is given by [45]

$$\mu(E) = 2f \left[\frac{V}{E} \arcsin\left(\sqrt{\frac{V}{E}}\right) - \sqrt{\frac{(V-E)}{E}} \right] \ , \tag{1.31}$$

where f is the UCN loss coefficient as described above.

The strong interaction plays a crucial role in the nEDM measurements. Choosing certain materials with high potential enables us to store and guide UCN to the measure-

ment cell. The highest known value for the optical potential is $V_F = 335$ neV for ^{58}Ni. The strong interaction is also responsible for neutron capture, which is used for neutron detection.

1.6 Superthermal UCN sources

In thermal UCN sources, neutrons are extracted from the tail of a distribution almost in thermal equilibrium with a moderation system. The UCN turbine source at the Institute Laue-Langevin (ILL) extracted very cold neutrons vertically from a cold source (liquid deuterium), and slowed them down using the mechanical action of a turbine [46, 47]. Here cold neutrons with velocities of ~ 40 m/s are decelerated by reflection from a set of curved turbine blades moving with a velocity ~ 20 m/s in the same direction as the neutrons. A UCN density of ~ 40 UCN/cm^3 was achieved typically for storage experiments conducted at the exit of the ILL turbine [44, 48].

In 1975 it was shown that, it is possible to achieve higher steady state UCN densities corresponding to temperatures much lower than the temperature of the moderator [49]. These are called the "superthermal converters". Here thermal or cold neutrons are inelastically scattered and transfer their kinetic energy to an excitation of the converter medium (e.g., to a phonon). Superthermal sources have the ability to provide much higher UCN densities than conventional sources such as the ILL turbine source. The best candidates for the superthermal converters to date are liquid ^{4}He and solid deuterium [44].

1.6.1 Basic Idea of Superthermal UCN Sources

The mechanism of a superthermal UCN source is the following. An incident neutron can lose almost its entire energy in a single scattering event by creating excitations (e.g., phonons) in a converter medium [44, 49]. Because of the loss in the kinetic energy, this process is called downscattering. The reverse process is called upscattering, where a UCN gains kinetic energy from the excited medium.

Consider a simple model for the medium as a two-level system with an energy gap

E_0^*. A neutron can excite a quasi-particle from the lower state to the higher state by transferring the energy E_0^*. A quasi-particle from the higher state can fall down to the lower state by transfer of the energy E_0^* to a neutron. The principle of detailed balance links the cross-section for upscattering $\sigma(E_{\rm UCN} \rightarrow E_{\rm UCN}+E_0^*)$ and downscattering $\sigma(E_{\rm UCN} + E_0^* \rightarrow E_{\rm UCN})$ [44]

$$\sigma(E_{\rm UCN} \rightarrow E_{\rm UCN} + E_0^*) = \frac{(E_{\rm UCN} + E_0^*)}{E_{\rm UCN}} e^{-\frac{E_0^*}{k_B T}} \sigma(E_{\rm UCN} + E_0^* \rightarrow E_{\rm UCN}) \tag{1.32}$$

where T is the temperature of the medium, $E_{\rm UCN}$ is the energy of the UCN, and k_B is the Boltzmann constant. The cross-sections σ are short-hand notation for differential cross sections in the final state energy

In general, $\sigma(E_{\rm UCN} + E_0^* \rightarrow E_{\rm UCN})$ is practically independent of T since it is a scattering cross-section (see section 1.6.2), so that for $E_0^* \gg k_B T \gg E_{\rm UCN}$, the upscattering cross-section for UCN can be made arbitrarily small by decreasing the temperature. If the converter is now placed in a neutron flux of average energy $T_n \geq E_0^*$, there will be a significant number of downscattering events, and a negligible number of upscattering events.

If the converter is contained in a vessel whose walls are good UCN reflectors with potential $V \gg V_m$, where V_m is the UCN potential of the converter, and the walls are transparent to neutrons of energy $> E_0^*$, then UCN will build up in the moderator to a density until the rate of loss is equal to the rate of UCN production.

The steady-state UCN density in the source is given by

$$\rho_{\rm UCN} = P_{\rm UCN} \tau, \tag{1.33}$$

where $P_{\rm UCN}$ (UCN/cm^3·s) is the UCN production rate, and τ (s) is the UCN mean lifetime in the system. The mean lifetime τ of the UCN in the vessel is restricted by a variety of possible loss mechanisms

$$\frac{1}{\tau} = \frac{1}{\tau_a} + \frac{1}{\tau_W} + \frac{1}{\tau_{up}} + \frac{1}{\tau_\beta}, \tag{1.34}$$

where $1/\tau_a$ is the UCN absorption rate in the medium, $1/\tau_W$ is the rate of the UCN loss on the walls, $1/\tau_{up}$ is the neutron loss due to the upscattering in the medium, and $1/\tau_\beta$ is the losses due to neutron lifetime.

Pure deuterium and liquid ^{4}He are good candidates for superthermal conductors, possessing a balance of high production rate, and small neutron absorption cross-section, and upscattering rate.

1.6.2 UCN Production by Superfluid ^{4}He

Superfluid ^{4}He Definition

^{4}He is an isotope of helium with two protons and two neutrons and has zero spin, which makes it a boson. As a result, it follows the Bose-Einstein statistics, which means when cooled to very low temperatures, it concludes into the lowest accessible quantum state resulting in a new form of matter.

Liquid helium has two states known as He-I and He-II. The He-I phase is the normal fluid phase. The He-II phase can be described by the so-called "two-fluid model", which consists of normal liquid helium and superfluid helium. Figure 1.1 shows the phase transition diagram of ^{4}He. The two phases are separated by the λ-line. The phase transition happens at 2.172 K. Below 1 K, the liquid is mostly the superfluid component of the two-fluid model. In this thesis, I use the term "superfluid helium" generally to refer to He-II cooled significantly below the lambda point, which is nearly synonymous with that component of the two-fluid model.

Because of its zero viscosity, superfluid helium has the ability to flow through very small capillaries or narrow channels without experiencing any friction at all. The climbing of He-II along the surface is called "film flow".

Superfluid Helium Converter

Superfluid ^{4}He is an attractive candidate as a UCN source, and was studied in Ref. [50]. It has zero neutron absorption cross-section, resulting in $\tau_a \to \infty$. The dominant UCN production mechanism in superfluid helium is the excitation of a single phonon at the

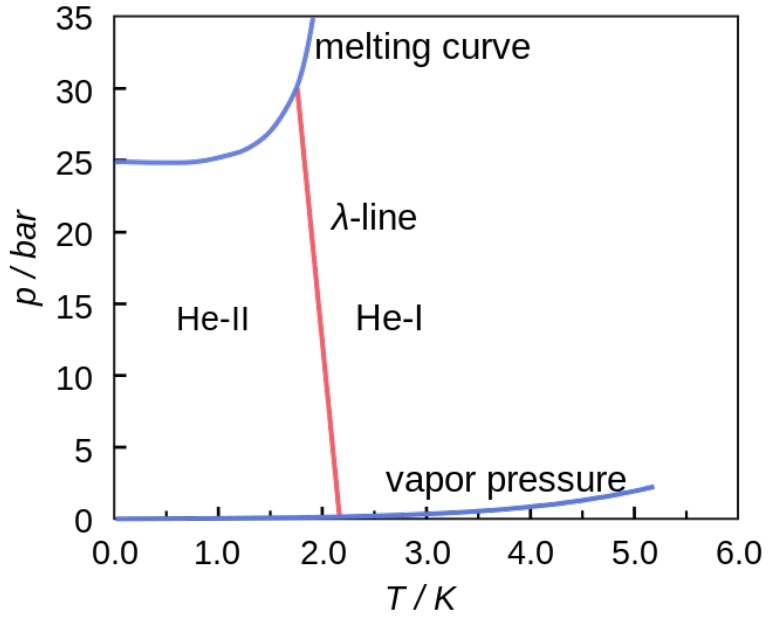

Figure 1.1: The phase diagram of ^{4}He. Here the normal fluid phase or He-I and the superfluid phase or H-II are shown.

crossing of the free neutron and phonon dispersion curves in Fig. 1.2, with wavenumber $q \sim 0.7$/Å [51], and energy ∼1 meV corresponding to a neutron wavelength 8.9 Å. The availability of 8.9 Å cold neutrons is crucial and their flux must be maximized.

There are two types of UCN sources based on superfluid helium: sources where experiment and source are combined in one apparatus [52, 53], and the measurement is performed inside the superfluid helium, and extracted-UCN sources where the source is an apparatus on its own, and delivers neutrons to experiments at room temperature connected to it by UCN guides (see section 1.7).

UCN Production Rate with Single Phonon scattering in Superfluid helium

UCN can be produced in superfluid helium when the energy of the incident neutrons is equal to that of the one phonon excitation in the converter medium [50, 54, 55]. The incident neutrons then downscatter to UCN in the converter medium while creating a phonon.

Figure 1.2 shows the dispersion relation of superfluid helium and a free neutron. The

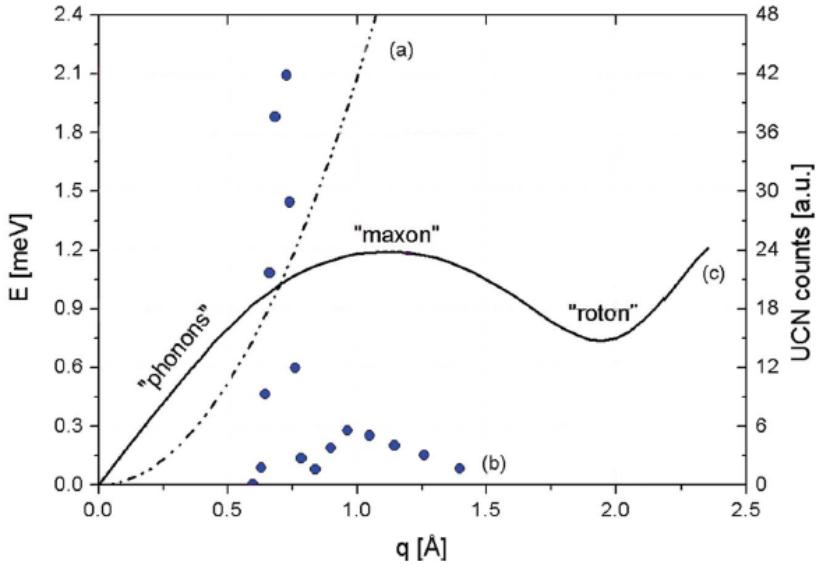

Figure 1.2: [56] Dispersion relation of superfluid helium (c) and of the free neutron (a). Neutrons with $E \simeq 1$ meV and wavenumber $q \simeq 0.7/\text{Å}$ can excite a single phonon with the same energy and momentum and be downscattered to UCN energy range. The UCN production rate (b)(circles) shows the dominance of this single phonon process with respect to multiphonon processes at higher momentum q.

neutron dispersion relation obeys

$$E_k = \frac{\hbar^2 q^2}{2m} = \hbar\omega \ , \tag{1.35}$$

where the neutron energy is $\hbar\omega$ and its momentum is $\hbar q$. For low-momentum phonons

$$\omega = \omega(q) \simeq cq \ , \tag{1.36}$$

where c is the speed of sound in the moderator. This equation is an approximation to simplify the discussion. The neutrons can only come to rest by emission of a single phonon, if they have the resonant energy E_0^* given by the intersection of the curves in Fig. 1.2 where Eqns. 1.36 and 1.35 are equal to one another

$$\omega(q) = cq = \frac{\hbar q^2}{2m} \ , \tag{1.37}$$

and so

$$q^* = \frac{2mc}{\hbar} \ . \tag{1.38}$$

The differential cross-section for neutron scattering is given by the dynamic scattering function $S(q,\omega)$, which is the Fourier transform of the Van Hove correlation function $G(r,t)$ in space and time of the superfluid helium [57]:

$$\frac{d\sigma}{d\omega} = b^2 \frac{k_2}{k_1} S(q,\omega) d\Omega \ . \tag{1.39}$$

Where b is the bound neutron scattering length for ^{4}He, $\hbar k_1$ is the momentum of the incident neutrons, and $\hbar k_2 = \hbar k_{\mathrm{UCN}}$ is the momentum of the UCN. The quantity $S(q,\omega)$ has been measured in great detail for different pressures, temperatures, q and ω values in Ref. [58–60]. Performing the change of variables,

$$d\Omega = 2\pi \sin\theta d\theta = 2\pi \frac{qdq}{k_1 k_2} \tag{1.40}$$

gives

$$\frac{d\sigma}{d\omega} = 2\pi b^2 \frac{k_2}{k_1} S(q,\omega) \frac{qdq}{k_1 k_2} = 2\pi b^2 S(q,\omega) \frac{qdq}{k_1^2} \ . \tag{1.41}$$

This may be integrated over the limits on q which are

$$k_1 - k_2 < q < k_1 + k_2 \ . \tag{1.42}$$

Since

$$k_2 = k_{\mathrm{UCN}} \ll k_1 \ , \ \ q \sim k_1 \ , \tag{1.43}$$

we may write $dq = 2k_{\mathrm{UCN}}$. This results in the cross-section being related to $S(q,\omega)$ evaluated on the incident neutron's dispersion curve:

$$\frac{d\sigma}{d\omega} = 4\pi b^2 \frac{k_{\mathrm{UCN}}}{k_1} S\left(k_1, \omega = \frac{\alpha k_1^2}{2}\right), \tag{1.44}$$

where $\alpha = \frac{\hbar^2}{m} = 4.14$ meVÅ^2, and $S(q,\omega)$ is assumed to be constant over the narrow

range dq. The approximation

$$\omega = \frac{\hbar(k_1^2 - k_2^2)}{2m} = \frac{\alpha}{2}(k_1^2 - k_2^2) \approx \frac{\alpha}{2}k_1^2 \tag{1.45}$$

has also been used.

The UCN production rate is given by

$$P(E_{\rm UCN})dE_{\rm UCN} = N_{\rm He}\int \frac{d\Phi(E_1)}{dE}\cdot\frac{d\sigma}{d\omega}(E_1 \to E_{\rm UCN})dE_1 dE_{\rm UCN}\ , \tag{1.46}$$

where $\frac{d\Phi(E_1)}{dE}$ is the differential incident neutron flux, $N_{\rm He}$ is the atomic density in the liquid helium, and $\frac{d\sigma}{d\omega}(E_1 \to E_{\rm UCN})$ is the energy differential cross-section for the inelastic neutron scattering or the probability of the incident neutrons with energy E_1 to scatter from the helium nucleus and become UCN. Then

$$\begin{aligned}\int_0^{E_c} P(E_{\rm UCN})dE_{\rm UCN} &= N_{\rm He}4\pi b^2\alpha^2\left[\int \frac{d\Phi(k_1)}{dE}S\left(k_1,\omega=\frac{\alpha k_1^2}{2}\right)dk_1\right]\int_0^{k_c} k_{\rm UCN}^2 dk_{\rm UCN}\\ &= N_{\rm He}4\pi b^2\alpha^2\left[\int \frac{d\Phi(k_1)}{dE}S\left(k_1,\omega=\frac{\alpha k_1^2}{2}\right)dk_1\right]\frac{k_c^3}{3}\ {\rm UCN/cm^3 s},\end{aligned} \tag{1.47}$$

where E_c and k_c are the critical UCN energy and wave vector of the walls of the storage chamber for total reflection. This way of writing the UCN production rate is more general, and it is useful to calculate the single phonon and multiphonon contributions to the UCN production rate. Korobkina *et al.*, [54] found the one phonon production rate by evaluating Eqn. (1.47) over the one phonon peak ($q^* = 0.7/$Å, see Fig. 1.3). Thus

$$P_{\rm UCN} = 9.44\times10^{-9}\frac{d\Phi(E_1^*)}{dE_1^*}\ {\rm UCN/cm^3}, \tag{1.48}$$

where E_1^* is the energy of the incident neutrons at the one phonon peak.

Multiphonon Scattering Contribution in UCN Production in Superfluid helium

For polychromatic neutron sources, UCN can also be produced by multiphonon processes in superfluid ^{4}He [54, 55]. Multiphonon production of UCN with various energy spectra of the neutron flux has been studied in Ref. [54] which is summarized here. Figure. 1.3 shows the energy spectra $\frac{d\phi}{dE}$ for three sources as a function of momentum q, compared to the dynamic scattering function $S(q, \omega = \hbar q^2/2m)$ [54]. The peak at $q = 0.7/\text{Å}$ in the dynamic scattering function corresponds to the one phonon excitation by superfluid helium. The values of S above $1.2/\text{Å}$ are extrapolated, taking into account the known value of $S(q)$ for the one phonon and multiphonon contributions [54]. The value of S above $q = 2/\text{Å}$ is essentially zero [54]. The UCN production rates from one phonon and multiphonon processes have been calculated for three input neutron spectra: the SNS ballistic guide, the PULSTAR MC flux, and the HMI polarized flux. The multiphonon contribution to the UCN production is calculated using Eqn. (1.47), and calculating $\int \Phi(E_1) S(k_1, \omega = \frac{\alpha k_1^2}{2}) dk_1$. The result showed that, for sources where He-II is exposed to the total thermal flux or at a dedicated spallation source, the multiphonon contribution can amount to slightly more than a factor of 2 increase in the UCN production.

UCN production by multiphonon excitation in superfluid helium under pressure was studied in Ref. [55] which is summarized here. The dynamic scattering function $S(q, \omega)$ of the superfluid helium strongly depends on pressure, leading to a pressure-dependent differential UCN production rate. The expression for the multiphonon part of S describing UCN production is derived from inelastic neutron scattering data. Application of pressure to superfluid helium increases the velocity of sound, such that the dispersion curves of the ^{4}He and of the free neutron cross at shorter neutron wavelength.

For neutron beams from a liquid deuterium cold source, the differential flux density $\left(\frac{d\Phi}{dE}\right)$ in the range 8-9 Å normally increases for decreasing wavelength of the cold neutron flux. Also, the pressure increases the density of He-II. Therefore, it was expected to observe an increase in the single phonon UCN production rate, and different multiphonon contribution with pressure increase. It was observed however that both, the single and

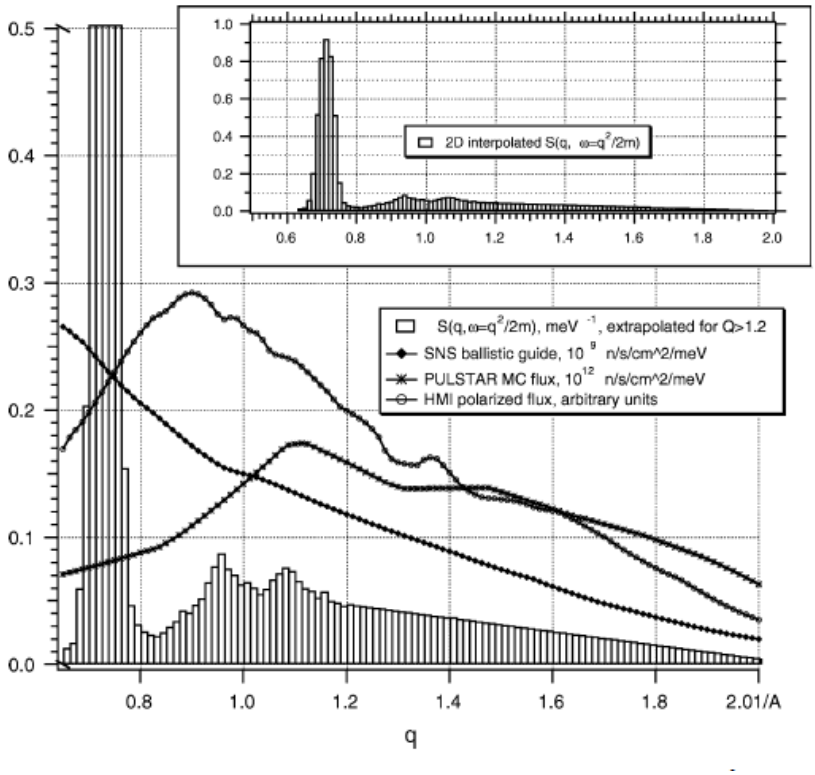

Figure 1.3: [54]The energy spectrum of the incident cold neutron flux from three sources compared to the dynamic scattering function $S(q, \omega = \frac{\alpha k_1^2}{2})$ /meV as a function of q /Å.

the multiphonon scattering functions change with pressure. The single phonon excitation moves to a shorter wavelength (see Fig. 1.4) and the value for S decreases. It leads to a reduction in one-phonon UCN production. The multiphonon excitations increase with pressure, and the peak of the scattering function S moves to shorter incident-neutron wavelengths, as seen in Fig. 1.4. However, the UCN production rate decreases with an increase in pressure. Only if the cold neutron flux at 8.3 Å exceeds that at 8.7 Å by more than a factor of 2.5, can one expect an increase in the UCN production rate. However, it has to be considered that the application of pressure requires a window for UCN extraction which causes severe UCN losses. Therefore, UCN production in superfluid helium under pressure was concluded not to be attractive [55].

UCN upscattering and lifetime in superfluid helium

Superfluid ^{4}He has a zero neutron absorption cross-section, and if the converter is kept at sufficiently low temperatures (typically $\lesssim 1$ K), thermal upscattering of UCN is suffi-

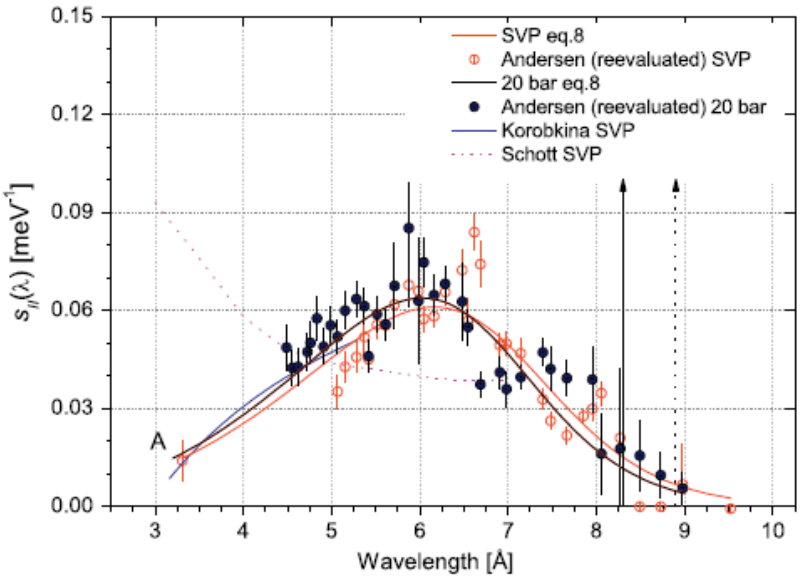

Figure 1.4: [55] Multiphonon scattering function at SVP (Saturated Vapour Pressure) and 20 bar in He-II. The extrapolation to short wavelength of Korobkina *et al.* [54] at SVP is linear in k, whereas the calculation of Schott *et al.* [61] is based on the static structure factor of the superfluid helium. The data point (A) is taken from Ref. [62]. The one-phonon peaks are indicated by vertical arrows: SVP (dotted line) and 20 bar (solid line).

ciently suppressed. This allows the produced UCN to survive in the converter for times dominated by the wall losses of the vessel, typically >100 s [63].

The upscattering of neutrons is caused by the interactions between a neutron at rest, and excitations in superfluid helium at different temperatures. These excitations can be categorized in three groups: one phonon absorption, two-phonon scattering, and roton-phonon scattering [63]. Following the discussion in Ref. [63], the total upscattering rate can be written as

$$\frac{1}{\tau_{up}} = \frac{1}{\tau_{1-ph}} + \frac{1}{\tau_{2-ph}} + \frac{1}{\tau_{rot-ph}} \, . \tag{1.49}$$

Where

$$\frac{1}{\tau_{1-ph}} = Ae^{-(12K)/T} \tag{1.50}$$

is the one phonon absorption contribution,

$$\frac{1}{\tau_{2-ph}} = BT^7 \tag{1.51}$$

is the two-phonon scattering contribution (one phonon absorbed and one phonon emitted), and

$$\frac{1}{\tau_{rot-ph}} = CT^{3/2}e^{-(8.6K)/T} \tag{1.52}$$

is the contribution from roton-phonon scattering with the absorption of one roton followed by a phonon emission.

The values of A, B and C were extracted from data for temperature ranges of up to 2.4 K [63]. The comparison between the UCN production and upscattering rate to the theoretical temperature dependence of these processes showed that, the main contribution is from two-phonon scattering $\frac{1}{\tau_{up}} = BT^7$ with $B = 0.0076$ /(s K^7) at 1 K and $B = 0.0088$ /(s K^7) at 0.6 K[63].

1.6.3 UCN production by Solid Deuterium

Solid deuterium (sD_2) is a material with small capture cross-section, small incoherent scattering cross-section (to minimize upscattering), and has numerous phonon modes, which can inelastically scatter neutrons down to UCN energies. A converter based on sD_2 should be operated at temperatures below 10 K in order to avoid subsequent upscattering of UCN by phonons within solid deuterium [64].

The different molecular species, ortho-D_2 and para-D_2, have significantly different UCN-phonon annihilation cross-sections [65, 66]. The presence of even small concentrations of para-D_2 can dominate the upscattering rate which gives rise to reduced UCN lifetimes in the solid and orders of magnitude reduction in the achievable UCN density. Since the elimination of para-D_2 is necessary to achieve UCN lifetimes comparable to the nuclear absorption time in solid deuterium, using a para-D_2 to ortho-D_2 converter is crucial.

Theoretically and experimentally, it has been shown that sD_2 at sufficiently low temperatures (around 5K) with high enough purity (less than 0.2% ordinary hydrogen) and

with high ortho concentration ($c_0 > 0.98$) can be used to produce high density UCN [67].

UCN upscattering and UCN lifetime in sD_2

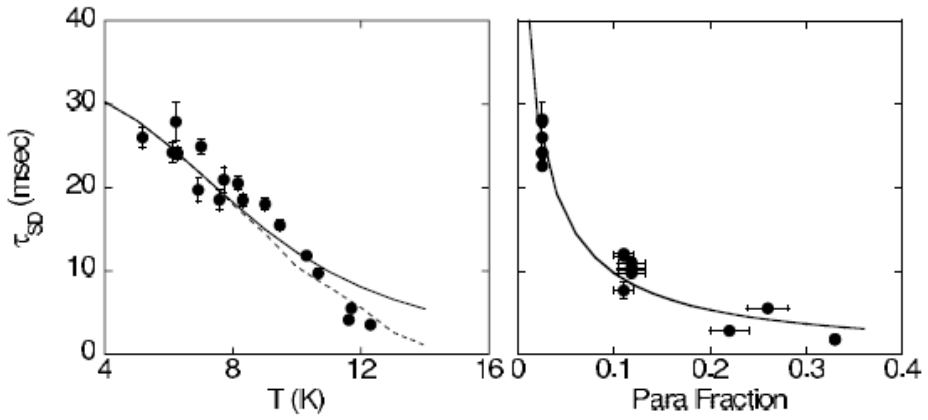

Figure 1.5: [66] Left- Data points are measured sD_2 lifetimes as a function of temperature, with the para-fraction fixed at 2.5%. Only the statistical errors are shown. Solid lines show the predicted temperature dependence. The dashed line is the predicted effect of departure from the solid lifetime model due to the upscattering from the D_2 gas in the guide. Right- sD_2 lifetimes as a function of para-fraction for all of the data taken below 6 K. The solid line is the model prediction of the para-fraction dependence at an average temperature of 5.6 K.

The lifetime of the UCN in sD_2 is limited by factors such as upscattering from phonons in the solid, upscattering from para-D_2 contamination, and absorption inside the vessel. Reducing the time UCN spend inside the sD_2 can reduce the average absorption rate. This led to the proposal of a thin-film source where a thin layer of solid D_2 coats the inside of a storage bottle that is embedded in a cold neutron flux [68]. The possibility of a smaller source volume combined with the higher operating temperature of the thin film source offers significant technical simplification. In Ref. [69] losses in frost layers on the surface of the deuterium crystal and the role of annealing have been quantified.

The UCN lifetime in the solid deuterium as a function of the temperature and para/ortho fractions has been measured [66]. The total loss rate can be written as

$$\frac{1}{\tau_{SD}} = \frac{1}{\tau_{phonon}} + \frac{1}{\tau_{para}} + \frac{1}{\tau_{Dabs}} + \frac{1}{\tau_{Habs}}, \tag{1.53}$$

where $\frac{1}{\tau_{phonon}}$ is the upscattering rate from phonons in SD_2, $\frac{1}{\tau_{para}}$ is the upscattering

rate from para deuterium molecules in the solid, $\frac{1}{\tau_{Dabs}}$ is the upscattering rate from the absorption on deuterium and $\frac{1}{\tau_{Habs}}$ is the upscattering rate from the absorption on the hydrogen impurities in the solid.

The results for UCN lifetimes τ_{SD} in sD_2 as a function of the sD_2 temperature and para/ortho fractions are shown in Fig. 1.5. The difference between the solid and dashed line demonstrates the need to include the effect of deuterium vapour in the guide on the lifetime at higher temperatures. With this correction, the measured lifetimes agree well with theoretical predictions of the upscattering rate.

1.6.4 Comparison between sD_2 and superfluid helium sources

The main differences between sD_2 and superfluid helium sources are the UCN lifetime and the UCN production rate. While UCN can stay in superfluid helium until they beta-decay, UCN in solid deuterium are lost typically 30 ms after they are produced 1.5 Once a superfluid helium source is cooled down to temperatures below 0.75 K, the upscattering rate is suppressed to a level comparable to neutron β-decay rate. Solid deuterium has a production rate two orders of magnitude greater than superfluid helium, due to the presence of more phonon modes. Therefore, solid deuterium sources output higher UCN flux compared to superfluid helium sources. However, the lifetime in superfluid helium can be four orders of magnitude longer than sD_2. Thus, even with a smaller UCN production rate, superfluid ^{4}He can in principle achieve a UCN density larger than that of solid deuterium. The superthermal enhancement in solid deuterium is limited by the large nuclear absorption loss, and thus further cooling below 5 K will not significantly enhance the UCN yield.

Anghel *et. al.,* [69] showed that in addition to the quality of the bulk sD_2, the quality of its surface is essential for UCN yield. They showed that the surface is deteriorating due to a build-up of D_2 frost-layers under pulsed operation which leads to a subsequent loss in UCN yield.

Isotope	σ_a(barns)	σ_s/σ_a
^{2}D	0.000519	1.47 $\times 10^4$
^{4}He	0	∞
^{15}N	0.000024	2.1 $\times 10^5$
^{16}O	0.00010	2.2 $\times 10^4$
^{208}Pb	0.00049	2.38 $\times 10^4$

Table 1.3: Candidates for a superthermal source

1.6.5 Other UCN Sources

Superthermal UCN sources are compared by

$$\sigma_s/\sigma_a, \tag{1.54}$$

where σ_s is the elastic scattering cross-section, and σ_a is the absorption cross-section [70–72]. At low energies (< 1 eV) $\sigma_a \propto 1/v$ where v is the speed of the neutrons. This means, the absorption cross-section is much larger at lower energies. Table 1.3 shows a list of possible superthermal UCN sources [72]. The values of σ_a are for thermal neutrons.

Solid $\alpha-^{15}N_2$ (in the α phase where $T < 35$ K) is a potential alternative to deuterium [70]. Its absorption cross-section is only 5% of that of D_2, and it has a negligible incoherent scattering cross-section. Additionally, rotation of the N_2 molecules in the lattice is inhibited due to the anisotropy of the N_2 inter-molecular potential. This leads to dispersive modes for the rotational degrees of freedom (librons), which provide additional channels for neutron downscattering, and eliminates the rotational incoherent upscattering. Measurements [70] show that, the production cross-section peaks near 6 meV, and that the optimal incident cold neutron temperature is 40 K. It was found that the variation in the cross-section is no more than 18% in the range from 5 to 25 K (increasing slightly with increasing temperature). The measured cross-section was found to be somewhat lower than that of D_2 and O_2. A nitrogen-based source may benefit from operating at lower temperatures, if the upscattering cross-section can be further reduced at lower temperatures ($\sim$1 K) [70].

^{208}Pb and solid deuterium have similar nuclear absorption cross-sections. The natural

solid form of ^{208}Pb would avoid the difficulties of growing cryogenic solids such as deuterium and oxygen.However, its heavy mass prevents any substantial neutron momentum transfer. The heavy mass reduces the phonon creation cross-section by $1/M$. As a result, one would expect its UCN yield to be two orders of magnitude less than solid deuterium.

As other options, the properties of the new candidate converter materials including solid heavy methane (CD_4) and solid oxygen (O_2) have been investigated in the temperature range 8 K to room temperature by measuring the production of UCN from a cold neutron beam and cold neutron transmission through the converter materials [71]. Liquid O_2, D_2 and CD_4 have similar neutron scattering cross-sections.

^{4}He and D_2 are still the best commonly pursued options, although there is a chance that other materials could lead to a breakthrough.

1.7 Current Status of UCN Sources Worldwide

New UCN sources using superthermal technology are under development at various laboratories across the world. Neutrons are usually produced by two methods: proton-induced spallation off a heavy nuclear target (e.g., tungsten), and fission where neutrons are produced by a nuclear reactor. Table 1.4 shows a list of present and future UCN sources worldwide.

Reactor sources place the moderators close to the reactor core (FRM II and Gatchina [73]), or use existing Cold Neutron (CN) beam lines (ILL [74]). At FRM II, the sD_2 will be placed around a solid hydrogen cold-moderator close to the fuel element. The Gatchina superfluid ^{4}He source will be placed inside their thermal column, using immense pumping power to cool the converter to 1.1 K, making rapid extraction necessary due to increased UCN upscattering at this temperature.

The SuperSUN and SUN-2 experiments are the logical extensions of the early superthermal source geometry at ILL. A novel feature of the SuperSUN source at ILL [75] is a magnetic multipole reflector for a drastic enhancement of the UCN density with respect to an existing prototype superfluid helium UCN source installed in a cold neutron

Name	Source Type	Technology	Status
ILL	Turbine	Reactor, CN beam	Running
ILL SUN-2	LHe	Reactor, CN beam	Running
ILL SuperSUN	LHe	Reactor, CN beam	Future
RCNP/TRIUMF/KEK	LHe	Spallation	Running/Upgrading
PNPI Gatchina	LHe	Reactor	Future
LANL	sD_2	Spallation	Running
PSI	sD_2	Spallation	Running
Mainz	sD_2	Reactor	Running
FRM II, Germany	sD_2	Reactor	Future
NCSU PULSTAR	sD_2	Reactor	Installing
SNS, Oakridge	LHe	Spallation	Future
J-PARC	Doppler Shifter	CN beam	Running

Table 1.4: Existing and future UCN sources worldwide. The existing or proposed sources at the following sites is listed: Institute Laue-Langevin (ILL) in France, Research Centre for Nuclear Physics (RCNP) in Japan, KEK and J-PARC in Japan, TRIUMF in Canada, Petersburg Nuclear Physics Institute (PNPI) in Russia, Los Alamos National Lab (LANL), PULSTAR at NCSU and SNS at ORNL in the US, Mainz and FRM II at TÜM in Germany.

beam. A multipole magnet can lead to a large gain in the saturated density of low-field-seeking UCNs because the presence of the field reduces the number of neutrons hitting the material walls and reduces the energy and wall collision rate of those that do. In addition, it acts as a source-intrinsic UCN polarizer without need to polarize the incident beam, and hence reducing associated losses.

The Los Alamos solid deuterium source [76] uses a proton beam of 900 MeV and a W target to produce neutrons. The neutrons get cooled down in a polyethylene cold moderator. There is a flapper valve to isolate the neutrons from the sD_2 after the proton beam pulse.

The PSI UCN source [77] uses a 600 MeV proton beam to hit a Pb/Zr target for neutron production. They use a 30 L volume of sD_2 at 5 K as the moderator and converter to produce UCN. This volume is surrounded by a D_2O thermal moderator. They also use a flapper valve for UCN extraction between the proton beam pulses to limit the losses. The UCN production has been running since 2012 with an on-going EDM experiment, with a peak density of 23 UCN/cm^3.

The Mainz UCN source [78] is the only source that operates at a low power university

reactor, and is the newest production source. The solid deuterium converter, with a volume of $V = 160$ cm^3, is exposed to a thermal neutron fluence of 4.5 $\times 10^{13}$ n/cm^2, and delivers up to 240000 UCN ($v \leq 6$ m/s) per pulse outside the biological shield at the experimental area. UCN densities of $\approx 10/$ cm^3 were obtained in stainless-steel bottles of $V \approx 10$ L. Their pulsed operation permits the production of high densities for storage experiments.

At the SNS UCN source, they are planning to use a monochromator to select 8.9 $\mathring{A}$ cold neutrons, which will then be transported through neutron guides to two cells made out of acrylic (ultraviolet transmitting) and separated by a high voltage electrode. The neutrons entering the cell will be polarized. Within the cell, the cold neutrons are downscattered to UCN via ^{4}He single-phonon process [79].

The UCN source at J-PARC is a Doppler-shifter type of pulsed UCN source [80]. Very cold neutrons (VCNs) with velocity 136 m/s in a neutron beam supplied by a pulsed neutron source are decelerated by reflection on a wide-band multi-layer mirror, yielding pulsed UCN. The mirror is fixed to the tip of a 2,000 rpm rotating arm moving with 68 m/s velocity in the same direction as the VCN. The repetition frequency of the pulsed UCN is 8.33 Hz and the time width of the pulse at production is 4.4 ms. In order to increase the UCN flux, a supermirror guide, wide-band monochromatic mirrors, focus guides, and a UCN extraction guide have been newly installed or improved. This source will be used to search for a nEDM.

The current UCN source at TRIUMF uses a W target to produce spallation neutrons from a 500 MeV proton beam on site. The cold neutrons are converted to UCN in superfluid helium. The future UCN source is projected to compete with the capabilities of the best planned future UCN sources. If TRIUMF's estimated UCN density of 680 UCN cm^{-3} is achieved, it will be a new world record.

Other sources and nEDM experiments aim at similar goals of hundreds to thousands of UCN cm^{-3} in the measurement volume. However, to date, superthermal sources have not produced considerably more UCN than the ILL turbine source.

1.8 Measurement of the nEDM

To measure the nEDM, an ensemble of polarized UCN are put in the presence of aligned electric and magnetic fields. The Hamiltonian of the interaction of the UCN with electric and magnetic fields is given in eqn. (1.12). The Larmor precession frequency of UCN is then measured in two orientations of parallel and anti-parallel electric and magnetic fields. For the parallel **E** and **B** fields, the Larmor precession frequency of UCN is written as

$$h\nu_{\uparrow\uparrow} = 2\mu_n|\mathbf{B}^{\uparrow\uparrow}| + 2d_n|\mathbf{E}^{\uparrow\uparrow}| \ , \tag{1.55}$$

and for anti-parallel **E** and **B** fields it is

$$h\nu_{\uparrow\downarrow} = 2\mu_n|\mathbf{B}^{\uparrow\downarrow}| + 2d_n|\mathbf{E}^{\uparrow\downarrow}| \ . \tag{1.56}$$

Here $\uparrow\uparrow$ indicates the parallel electric and magnetic fields and $\uparrow\downarrow$ represent the anti-parallel orientation of those fields. A nonzero nEDM would then be extracted from an observed frequency shift between these two measurements:

$$d_n = \frac{h\left(\nu_{\uparrow\uparrow} - \nu_{\uparrow\downarrow}\right) - 2\mu_n\left(|\mathbf{B}^{\uparrow\uparrow}| - |\mathbf{B}^{\uparrow\downarrow}|\right)}{2\left(|\mathbf{E}^{\uparrow\uparrow}| - |\mathbf{E}^{\uparrow\downarrow}|\right)} \ . \tag{1.57}$$

The main reason to employ this method is because it is impossible to completely eliminate the **B** field to extract the neutron EDM. These measurements are either performed in two adjacent volumes with $|E^{\uparrow\uparrow}| = -|E^{\uparrow\downarrow}|$, and $|B^{\uparrow\uparrow}| - |B^{\uparrow\downarrow}| = 0$, and/or measured in the same volume where the configuration of the fields changes in time. In the first case, it is essential to make sure that the magnitude of the magnetic fields inside both volumes are the same, i.e. there is no field gradient. In the second method it is essential to make sure that the magnetic field is stable in time.

1.9 Ramsey's Method of Separated Oscillating Fields

The Ramsey method of separated oscillating fields is the well-known measurement technique to extract the nEDM. Ramsey obtained an expression for the quantum mechanical transition probability of a system between two states, when the system is subjected to separated oscillating fields [81]. Figure 1.6(left) [82] shows a measurement cycle. An ensemble of polarized UCN with the initial spin $|\uparrow\rangle$ are exposed to a DC magnetic field B_0 and an electric field. A first RF pulse $B_1 \cos(\omega_{rf} t)$, perpendicular to the B_0 field, tips the spin of the neutrons into the transverse plane. The neutrons precess freely with their Larmor precession frequency ω_0 for some time T, while accumulating a phase $\phi = \gamma_n BT$, with γ_n being the gyromagnetic ratio of neutron. Then again, a second coherent oscillating magnetic field pulse of $B_1 \cos(\omega_{rf} t)$ is applied to the neutron ensemble to completely flip the spin. The essential idea is to compare the phase ϕ with $\omega_{rf} T$, which are identical if $B = \omega_{rf}/\gamma_n$.

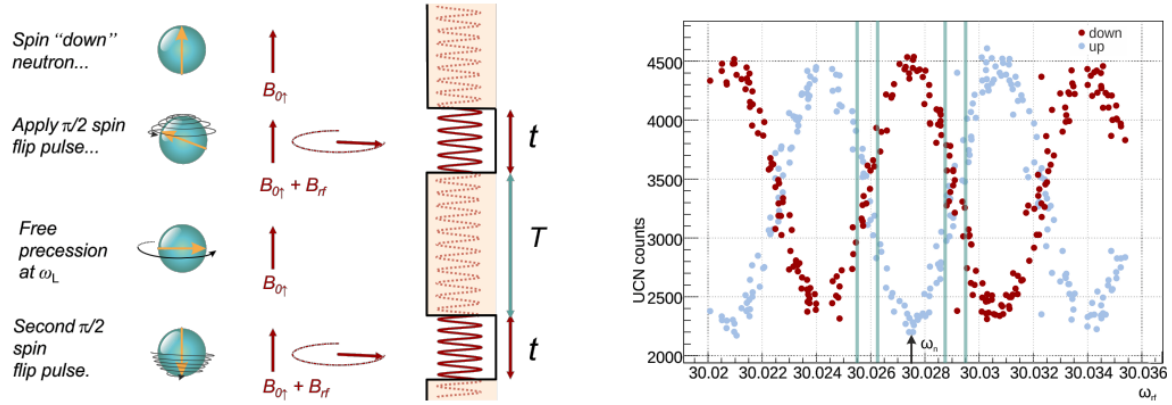

Figure 1.6: [83] Ramsey method of separated oscillating fields. Left shows the scheme of a measurement procedure and right shows the data points. The blue points are the UCN counts with the spin up and the red points are the UCN with spin down (data from the PSI-nEDM collaboration). The width at half height $\Delta\nu$ of the central fringe is approximately $1/2T$, the four vertical lines indicate the working points (see text).

The probability to find the UCN with spin up is

$$P(T, \omega_{rf}) = |\langle\uparrow| U(T, \omega_{rf}) |\uparrow\rangle|^2 \tag{1.58}$$
$$= 1 - \frac{4\omega_1^2}{\Omega^2} \sin^2 \frac{\Omega t_{\pi/2}}{2} \left[\frac{\Delta}{\Omega} \sin \frac{\Omega t_{\pi/2}}{2} \sin \frac{T\Delta}{2} - \cos \frac{\Omega t_{\pi/2}}{2} \cos \frac{T\Delta}{2} \right]^2 ,$$

where $U(T, \omega_{rf})$ is the time evolution operator, $\omega_1 = -\gamma_n B_1$, $\Delta = \omega_{rf} - \omega_0$, $\omega_0 = \gamma B_0$, and $\Omega = \sqrt{\Delta^2 + \omega_1^2}$. The spin-flipping pulses are optimized when $\gamma_n B_1 t_{\pi/2} = \pi/2$. In this case, the central fringe range Δ is much smaller than ω_1, and Eqn. 1.58 simplifies to

$$P(T, \omega_{rf}) = \frac{1}{2}\left(1 - \cos(T\Delta)\right) \ . \tag{1.59}$$

In a real measurement with N UCN inside a magnetic field region this becomes

$$N^{\uparrow} = \frac{N}{2}\left\{1 - \alpha(T)\cos\left[(\omega_{rf} - \omega_0)\cdot\left(T + \frac{T + 4t_{\pi/2}}{\pi}\right)\right]\right\} \ , \tag{1.60}$$

where α is the visibility of the central fringe with spin either up or down

$$\alpha^{\uparrow/\downarrow} = \frac{N_{max}^{\uparrow/\downarrow} - N_{min}^{\uparrow/\downarrow}}{N_{max}^{\uparrow/\downarrow} + N_{min}^{\uparrow/\downarrow}} \ . \tag{1.61}$$

The term $4t_{\pi/2}/\pi$ is necessary since the pulse length $t_{\pi/2}$ is finite. The graph in Fig. 1.6 (right) shows the Ramsey interference pattern by scanning ω_{rf}, while everything else is kept the same [83]. In actual nEDM measurements, only 4 points (for w_{rf}) with the highest sensitivity are measured. These points are referred to as the working points. For each configuration of the electric and magnetic fields (parallel or anti-parallel), Eqn. 1.60 is fitted to the data to extract the Larmor frequency ω_0. Taking the differences of those Larmor frequencies then give access to the nEDM

$$d_n = \frac{\hbar(\omega_0^{\uparrow\uparrow} - \omega_0^{\uparrow\downarrow})}{2(E^{\uparrow\uparrow} - E^{\uparrow\downarrow})} = \frac{\hbar\Delta\omega}{4E} \tag{1.62}$$

with the assumption that, the magnitude of the magnetic field is constant (see eqn. 1.57).

1.10 Statistical and Systematic Errors

1.10.1 Statistical Sensitivity

The statistical sensitivity of the nEDM measurement is given by

$$\sigma(d_n) = \frac{\hbar}{2\alpha T E\sqrt{N}} \ , \tag{1.63}$$

where N is the number of detected UCN, T is the free precession time, and E is the electric field. The visibility $\alpha = e^{-T/T_2}$ depends on the transverse spin relaxation time (T_2), which arises due to a combination of effects such as dephasing in inhomogeneous fields and relaxation processes that occur during wall collisions.

1.10.2 Systematic Errors

Improved sensitivity of the nEDM experiments gave rise to discovery of new systematic effects incorporated by Pendlebury *et al.,* in Ref. [26] briefly described in this section. The dominant systematic errors in the previous best experiment arose due to magnetic field instability and magnetic field inhomogeneity which can give rise to a false EDM for particle traps [84].

Following the discussion from Ref. [84], UCN move with velocity v in the cell in the presence of an electric field E, creating an effective magnetic field $\mathbf{B_v} = (\mathbf{E} \times \mathbf{v})/\mathbf{c^2}$. This field is much smaller than the applied $B_0\hat{z}$ field and lies in the xy plane considering the z direction along the axis of symmetry of a cylindrical EDM cell, the electric field pointing in the z-direction and particles in the trap (neutrons and Hg atoms) generally circulating in the xy plane on average. Another magnetic field which lies in the xy plane comes from the inhomogeneity of the B_0 field $B_{0xy} = -\left(\frac{\partial B_{0z}}{\partial z}\right)\frac{\mathbf{r}}{2}$ in a cylindrical coordinate system. Therefore, the total magnetic field in the radial direction is $\mathbf{B_{xy}} = \mathbf{B_{0xy}} + \mathbf{B_v}$. If we imagine a particle circulating the cell in the midplane of the cell, in the rest frame of the particle, it will experience circulating magnetic field of magnitude B_{xy}. This field will be far from magnetic resonance with the particle, but will nonetheless induce a Bloch-

Siegert shift on the particle's resonant frequency. The frequency shift is proportional to the square magnitude of B_{xy}. Since B_{xy} is composed of two contributions, it is the cross-term which will be proportional to E and hence give rise to a false EDM.

This false EDM could was corrected using the frequency ratio of the neutrons to the co-magnetometer atoms (^{199}Hg) used to sense the gradient (see section 2.1.5). This is because, inside the nEDM cell, there is no direct measurement of the magnetic field gradients. But, since the neutrons have lower centre of mass than the thermal mercury atoms, any change in the magnetic field grandient results in a change in the neutron to mercury frequency ratio [26]. Graphing the measured neutron EDM as a function of this frequency ratio then allowed to interpolate to zero gradient and hence discover the true neutron EDM. This was also supplemented by gradient determination using surrounding Cs magnetometers [85].

1.11 nEDM Status Worldwide

In 1950, the first upper limit on the neutron EDM was presented by Purcell and Ramsey to be 3×10^{-18} e·cm [8]. Since then many groups around the world measured the nEDM with increased sensitivity (see Fig. 1.7).

The most recent nEDM measurement at ILL reduced the upper limit to $d_n < 3.0 \times 10^{-26}$ e·cm (90% CL) [10, 26]. The most recent ^{199}Hg EDM measurement [86] constrains the nEDM better than direct nEDM measurements, giving $d_n < 1.6 \times 10^{-26}$ e·cm, although subject to uncertainty from Schiff screening.

There are several ongoing experiments seeking to measure the nEDM. Most groups are aiming initially for an improvement of the limit on d_n to the 10^{-27} e·cm level, ultimately improving to the 10^{-28} e·cm level over time.

The PSI nEDM experiment uses an improved version of the former Sussex-RAL-ILL single-cell apparatus [25]. The ILL nEDM aparatus, where the current upper limit on the nEDM was measured, was moved to PSI in 2009 to improve the sensitivity of the nEDM. The improvements include a higher UCN intensity, improved magnetometery and

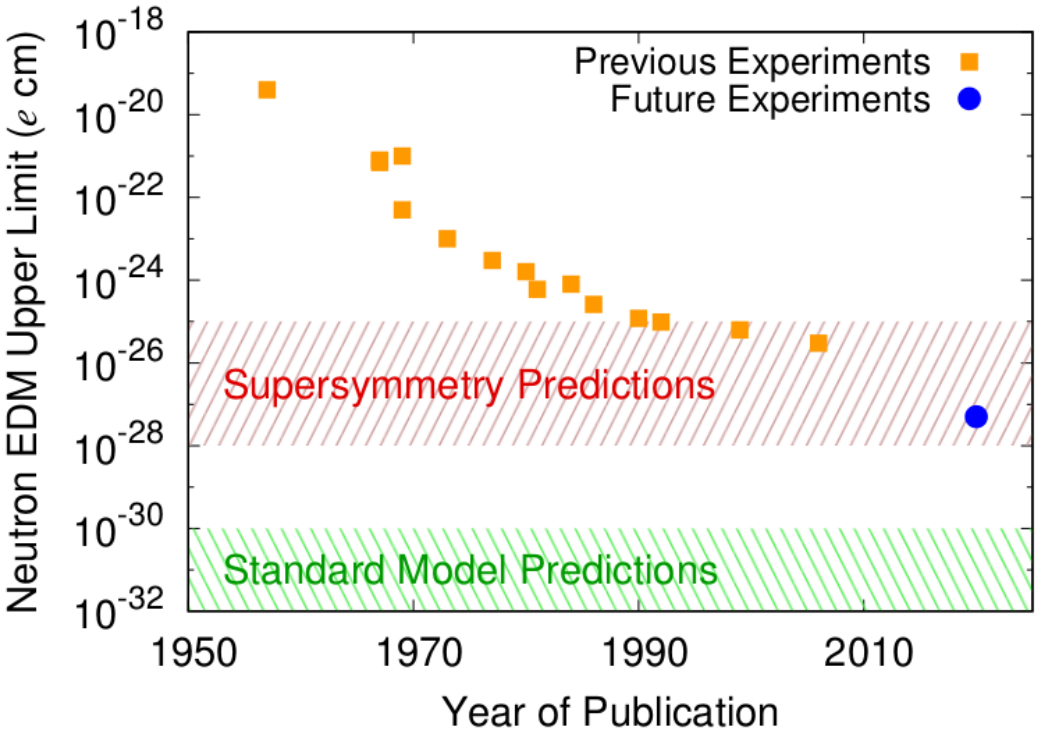

Figure 1.7: [87]The timeline of the upper bound on the neutron EDM from previous and future experiments. The yellow squares are the previous bounds, and the blue dot is the sensitivity target of next generation experiments. In the standard model, the expected size of nEDM is more than 5 orders of magnitude below the current experimental bound, as shown by the green shaded area in the plot. In extensions of the standard models, however, the expected size of nEDM covers the regions of the current and future experimental bound, as shown by the red shaded area. TUCAN intends to provide an error bar of 10^{-27} e·cm by about 2024-5.

magnetic field control. Several innovations have been made at PSI, including a new SD_2 spallation-driven UCN source. The experiment employs several Cs magnetometers outside the EDM cell, and a ^{199}Hg comagnetometer. Active magnetic shielding and other environmental controls have been improved. A new detector that can simultaneously count both spin states of UCN has also been implemented (see section 1.9 and chapter 2). Their final expected sensitivity is $\simeq 10^{-26}$ e·cm [82]. Some of the chief improvements made at PSI recently have been in the area of nearby alkali atom (Cs) magnetometry, Hg comagnetometry, and neutron magnetometry [88]. A recent achievement at PSI is the understanding of the Cs magnetometer signals in terms of magnetic field gradients. This has led to a detailed understanding of the false EDM of the Hg comagnetometer [89]. PSI also aims to improve their magnetometry with ^{3}He magnetometers inside the elec-

trodes of the double EDM measurement cells for their future n2EDM effort. They have performed R&D using Cs magnetometers to sense the free-induction decay signal from ^{3}He, which resulted in a new high-precision magnetometer possessing excellent long-term stability [90]. The precision goal for n2EDM is 5×10^{-28} e· cm [91, 92].

The nEDM collaboration at SNS plans to measure down to the limit of $d_n \approx 2 \times 10^{-28}$ e·cm, two orders of magnitude improvement over the current limit [93]. They plan to use a unique experimental technique. A CN beam from the SNS will impinge upon a volume of superfluid ^{4}He creating UCN. The nEDM measurement will then be conducted in the superfluid He. A small amount of polarized ^{3}He introduced into the superfluid ^{4}He will act as both a comagnetometer and spin analyzer for the UCN. The ^{3}He neutron capture rate is strongly spin dependent. A non-zero EDM would change the beat frequency with E-reversal. Scintillation light produced in the superfluid will be used to detect the capture products. The false EDM of the ^{3}He comagnetometer may be reduced by collisions in the surrounding ^{4}He [94]. The group aims to commission the experiment at SNS by 2022.

A new room-temperature nEDM experiment will be conducted using the upgraded LANL UCN source [95]. The aim of the project is to increase the UCN density by a factor of five to ten, which could then be used to carry out a $\sim 10^{-27}$ e·cm limit of the nEDM. The experiment aims for a 10^{-27}-level result, to be completed in the years prior to the SNS nEDM experiment.

Two other room temperature nEDM experiments are being pursued at ILL by a group from Munich [96] and a group from Russia [97], where the Russian experiment will be moved to the UCN source being developed in Gatchina. Both experiments feature double measurement cells and Cs magnetometers internal to the innermost magnetic shield. The Munich experiment features an impressive active and passive magnetic shielding system [98–100], and uses ^{199}Hg comagnetometry. Both groups are at the stage of constructing major equipment and upgrades.

1.12 Summary

Precision experiments involving the UCN provide an attractive avenue to investigate physics beyond the standard model. Measurement of the neutron EDM is an example of such experiments. For such studies high densities of UCN are needed.

UCN are very slow neutrons with velocities < 8 m/s that can be trapped in matter, magnetic and gravitational fields. Superthermal UCN sources have the potential to produce high densities of UCN. Such sources should have a very small neutron absorption cross-section and upscattering rate, while having a high UCN production rate. So far, the best candidates are superfluid helium and solid deuterium.

Both ^{4}He and solid D_2 UCN sources use quantum excitations in the converter medium to create the UCN; these are phonons in the case of superfluid ^{4}He and phonons and rotons in the case of sD_2. Since ^{4}He does not capture neutrons, and has a small upscattering probability for UCN, a superfluid ^{4}He source can be operated at lower fluxes for longer times, allowing a large density of neutrons to accumulate. In the case of superfluid helium, storage times of hundreds of seconds are achievable. The production rate in sD_2 is higher than in supefluid ^{4}He; however, the neutron storage lifetime is only tens of milliseconds.

The TRIUMF UCN project is a spallation-driven superfluid-^{4}He source [101]. The spallation-driven UCN sources at PSI [77] and LANL [76] use the phonons in solid deuterium as an alternative method of UCN production. The TRIUMF's UCN source uses an optimum proton beam structure (see section 4.1) on the minute scale to produce the highest density of UCN in the world, while sD_2 spallation sources benefit from pulsing the beam and isolating any UCN produced as quickly as possible to achieve high UCN densities. Details of the present UCN facility at TRIUMF are described in Chapter 4 and the result of the first UCN production with a vertical UCN source (since UCN are extracted vertically) is discussed in Chapter 5.

The neutron EDM can be measured using the Ramsey method of separated oscillatory fields. In this technique, polarized UCN are trapped in a material bottle in the presence of aligned electric and magnetic fields. The Larmor precession frequency of UCN is measured with the E and B fields parallel and anti-parallel. Any frequency shift in the

Larmor frequency of UCN is then indicative of a non-zero nEDM. The components of the future nEDM measurement at TRIUMF are described in Chapter 2.

My Contribution

My research on R&D projects for the future nEDM experiment at TRIUMF focused on the magnetic field stability and UCN production.

From September 2013 to February 2017, I worked on measuring the temperature dependence of magnetic permeability μ of the prototype magnetic shields available at the University of Winnipeg using various methods. The result of my work is presented in chapter 3 and Ref. [102].

In February of 2017, I moved to TRIUMF in Vancouver to contribute to the UCN project. I started by working on the DAQ system. I made Altium drawings for the sensors, and wired them in the PLC (see section 4.4). The first cryostat cool down happened in April 2017 (with no proton beam), and the first UCN production happend in November 2017. Running the cryostat requires extensive manpower, since it has to be monitored at all times. Therefore, all collaborators including students had to take 8-9 hour shifts. I took shifts during all cool down and UCN experimental runs, including the 2018 UCN production run, which will be presented in future publications. The UCN data presented in chapter 5 were collected by all the members of the TUCAN collaboration. I performed all the UCN data analysis for the storage lifetime and UCN yield measurements presented in chapter 5.

Chapter 2

Future nEDM Measurement at TRIUMF

As described in chapter 1 , a non-zero neutron electric dipole moment (nEDM) is directly linked to extra sources of CP violation beyond the Standard Model. The next generation of nEDM experiments aim to measure d_n with a proposed upper limit of $\delta d_n \lesssim 10^{-27}$ e·cm [92, 103–109]. The TUCAN (TRIUMF UltraCold Advanced Neutron source) collaboration is developing a world-leading experiment to measure the limit on the nEDM, improving the limit by a factor of thirty compared to the present world's best experimental result. The current nEDM experiments suffer from low UCN statistics and a key goal is to build the strongest UCN source in the world. To achieve this goal, extensive studies of the current vertical UCN source have been conducted.

2.1 TRIUMF nEDM Components

In 2016, the vertical UCN source from RCNP in Japan was shipped to TRIUMF for the research towards the development of the new upgraded UCN source. The details of the current UCN facility at TRIUMF are presented in Chapter 4. The results of the first set of UCN measurements with the vertical UCN source are available in Chapter 5.

The future nEDM experiment at TRIUMF will use a room-temperature nEDM apparatus, connected to an upgraded cryogenic UCN source shown in fig. 2.1. A proton beam

with an energy of 480 MeV and a current of 40 μA impinges on a tungsten spallation target, liberating neutrons. A room-temperature neutron moderator/reflector system composed of Pb, graphite, and D_2O, positioned above the target, thermalizes the neutrons. Liquid deuterium (LD_2) at 20 K creates a large flux of CN in a bottle containing superfluid ^{4}He below 1 K. In the superfluid helium, the CN excite phonon transitions, losing virtually all their kinetic energy to become UCN. Once a sufficient density of UCN is built up, the proton beam is turned off, and a cryogenic UCN valve opens. The UCN are transported out of the source by specular reflection from the surfaces of the UCN guides. A superconducting magnet (SCM) accelerates polarized UCN through barrier foils to a vacuum chamber at room temperature. The UCN are then transported to the nEDM experiment through additional guides.

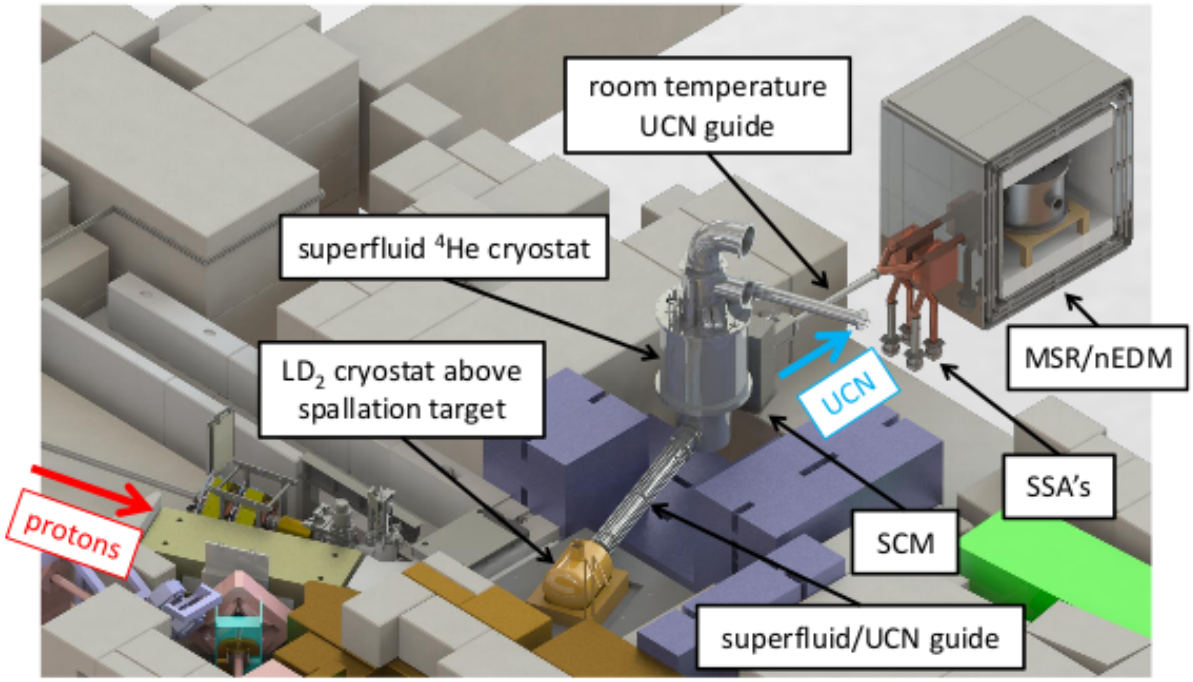

Figure 2.1: Conceptual design of the proposed UCN source and nEDM experiment. Protons strike a tungsten spallation target. Neutrons are moderated in the LD_2 cryostat and become UCN in a superfluid ^{4}He bottle, which is cooled by another cryostat located farther downstream. UCN pass through guides and the superconducting magnet (SCM) to reach the nEDM experiment located within a magnetically shielded room (MSR). Simultaneous spin analyzers (SSA's) detect the UCN at the end of each nEDM experimental cycle.

A brief description of the main components of the future nEDM apparatus at TRIUMF is presented below.

2.1.1 New UCN Source

The future nEDM experiment at TRIUMF will use an upgraded UCN source, with some differences compared to our prototype vertical UCN source described in Chapter 4. A conceptual design of the next generation UCN source is shown in fig. 2.2. The upgraded source is referred to as "the new horizontal source", because the UCN exit in a near-horizontal direction. When the UCN exit the He-II into vacuum, they gain a kinetic energy equivalent to the superfluid helium optical potential of only 18.5 neV (compared to 100 neV for sD_2 sources). This corresponds to a height of 18.1 cm in Earth's gravity field. If the energy gain of UCN after exiting superfluid helium was larger, we would need to put a vertical extraction guide piece to decelarate the UCN in order to keep them in the guides. Otherwise, since their energy would be higher than the optical potential of the guide surface, they would leave the guides. Therefore near-horizontal extraction of UCN is a reasonable development for He-II sources.

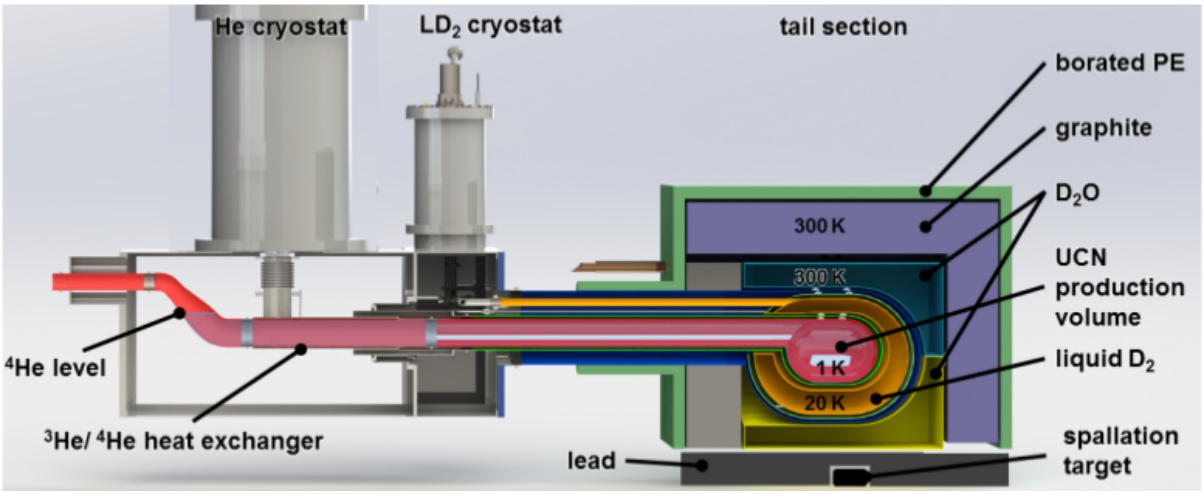

Figure 2.2: Conceptual design of the next generation UCN source planned for TRIUMF. Neutrons are liberated by proton-induced spallation in a target located beneath the He-II, and LD_2 and D_2O moderators. Neutrons are reflected and moderated in surrounding materials, then enter superfluid ^{4}He (He-II), where they are downscattered. Cooling for the superfluid is provided by heat exchanger within the He-II cryostat. UCN created in the He-II are transported out through the heat exchanger passing through the He-II surface into vacuum in a vertical rise, and to the experiment which is conducted at room temperature.

The heavy-water moderator at room temperature is a thermal pre-moderator for fast neutrons. The thermal moderator is placed around the cold moderator to reflect thermal

neutrons back into it. Additional graphite blocks serve as reflectors. The spallation target is covered with a layer of lead, which has a low neutron-absorption cross section and shields the cold moderator and converter from γ radiation.

The purpose of the cold moderator system is to produce the maximum number of 1 meV neutrons, with the minimum number of neutron captures in the material. Minimizing the neutron captures is important to prevent production of gamma rays which would heat the He-II in the UCN production volume, as well as to minimize neutron loss. For this reason, deuterated materials are preferable. Higher energy $>$ 1 meV neutrons can also be used, since multiphonon excitations in the superfluid can potentially produce UCN as discussed in Section 1.6.2 [54, 55]. The new UCN source uses an LD_2 cryostat to produce cold neutrons during the experiment, as opposed to the solid D_2O moderator in the vertical source. LD_2 increases the UCN production by a factor of 2-3, and reduces the heat load and the uncertainty in the UCN source performance.

The UCN production of the new source are estimated in detail, based on a Monte Carlo N-Particle (MCNP) model of the source, an analytical model of UCN production based on Ref. [54], and UCN transport simulations based on Ref. [110] including losses on walls and within the He-II and the vapour pressure above it. The simulations indicate that when driven by a 40 μA proton beam, the source will produce 2×10^7 UCN/s, with beam heating of the He-II $<$ 10 W, a design goal for our refrigerator. At the end of target irradiation, 3.4×10^8 UCN would be in the source prior to opening the room-temperature valve (not shown in fig. 2.2) to the nEDM experiment. The simulations also include transport into the nEDM experiment. A total of 6.5×10^6 UCN would be loaded into the EDM measurement cells prior to initiating the Ramsey cycle. Using reasonable values for lifetimes and spin-coherence times of the UCN (storage lifetime of 120 s or higher, and $T_1 = 1000$ s and $T_2 = 500$ s [111]), this corresponds to a statistical sensitivity to the nEDM of $\sigma(d_n) = 3 \times 10^{-25}$ e·cm per cycle. With reasonable assumptions for the running time available per day, a statistical sensitivity of $\sigma(d_n) = 10^{-27}$ e·cm would be achieved in 400 days.

The new UCN source will have several key improvements. Foremost of these is im-

proved heat exchanger design and improved cooling efficiency. Also to be improved are the internal neutron guides. We plan to use an Al-Be alloy bottle which will present a lower heat load on the He-II. Gamma and beta heating from the present Al bottle walls is projected to dominate the heat load to the superfluid. Extraction of UCN from the source will also be improved by near-horizontal extraction.

2.1.2 UCN Handling and Transport

Efficient transport of polarized UCN from the source to the nEDM cell is one of the major requirements for the nEDM measurement. This efficiency depends mainly on three parameters: UCN guide reflectivity, surface roughness of the UCN guides, and UCN depolarization. These are described below.

The first parameter is the capacity of the guide walls to reflect the UCN. As discussed in chapter 1, UCN have a large wavelength compared to the lattice constants in solid matter (50 to 130 nm compared to 0.3 nm). Therefore, during a scattering process, a UCN interacts with hundreds of nuclei. The mean nuclear potential experienced during the scattering (optical potential) depends on the material. In order to reflect UCN, the optical potential must be as high as possible.

The second parameter is the roughness of the surface. Transport is more efficient if the roughness is low because the probability of specular reflection is increased. Ideally, the roughness should be lower than the UCN wavelength of ~ 40 nm but, in practice this is challenging to achieve.

The last parameter is the depolarization. UCN can be depolarized during a collision due to different processes, such as spin incoherent nuclear scattering, paramagnetic scattering or large magnetic field gradients. When selecting materials for UCN components, the mean depolarization rate per bounce should be as small as possible. In practice this means nonmagnetic coatings should be used for polarized UCN traps.

The main task of the UCN handling parts is to transport a large fraction of the phase-space of the UCN to achieve the highest possible UCN density and thus statistical sensitivity of the experiment.

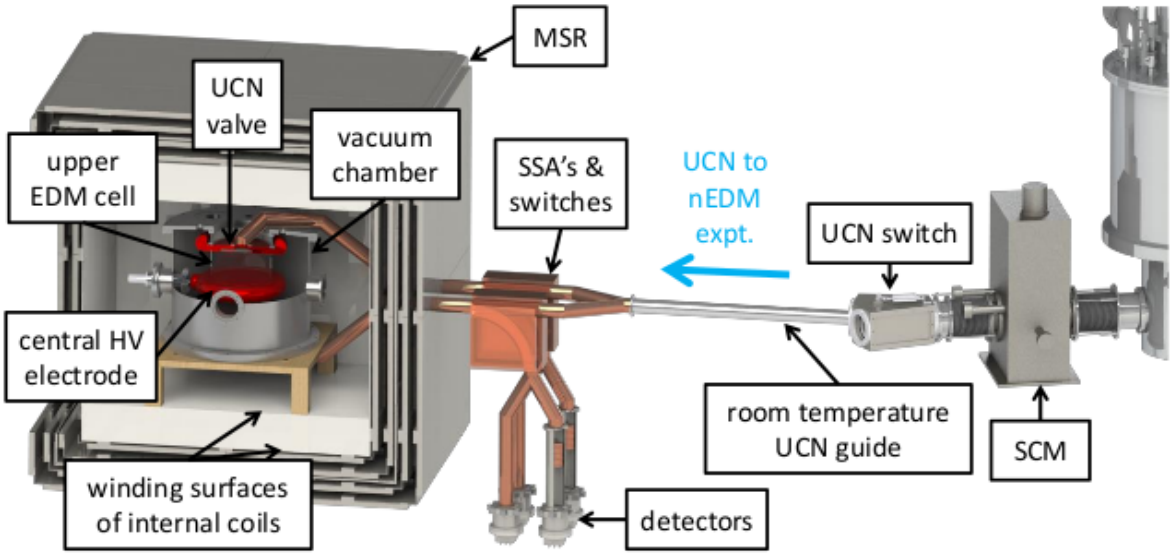

Figure 2.3: A 3D model of the UCN delivery and the future nEDM experiment at TRIUMF. UCN exit the source by passing through the SCM spin polarizer, and UCN switch and detector system, where they then enter the proposed nEDM experiment. UCN are loaded into the measurement cells within a MSR/coil system. At the end of the measurement cycle, UCN are counted by simultaneous spin analyzers (SSA's) including detectors. An ambient magnetic compensation system, and thermally controlled room, will surround the nEDM apparatus (not shown). For scale, the innermost layer of the MSR is a 1.8 m side-length cube.

The parts that come in contact with UCN on the way from the UCN source to the EDM experiment, and the UCN detectors, constitute the neutron handling hardware: UCN guides, valves, switches and the simultaneous spin analyzer (SSA) system. Figure 2.3 shows the neutron handling parts for the future nEDM experiment at TRIUMF. UCN exiting the source are polarized by a superconducting magnet (SCM), and then enter the nEDM experiment.

Suitable guides and valves have optimized geometries: wall materials with large optical potentials, low upscattering and absorption cross sections for neutrons, and low roughness and depolarization. The plan is to use Be in the UCN production volume, and NiMo coatings on glass and Cu substrates for most of the other surfaces, where non-magnetic polarization preserving guides are required.

UCN spins will be measured by two separate simultaneous spin analyzer (SSA) systems (one for each cell, described in section 2.1.4). This configuration allows simultaneous counting of both UCN spin states, and maximizes the visibility of the Ramsey fringes and

counting efficiency. The UCN switches load the UCN into the nEDM experiment, and divert UCN exiting the experiment into the detectors. A prototype detector, based on scintillating lithium glass, which is capable of handling the highest rates of UCN expected with the TRIUMF source, has been developed and tested in the highest rate UCN beam available at PSI [112] (See Chapter 4).

2.1.3 Magnetic Fields in the nEDM Experiment

To achieve the desired nEDM limit of 10^{-27} e·cm, an extremely stable and homogeneous B_0 magnetic field is required. The upper limit of the magnetic stability for TUCAN's nEDM measurement is 1 pT (for hundreds of seconds) and the upper limit of the magnetic homogeneity is 1 nT/m. To achieve this challenging level of magnetic stability, a ^{199}Hg co-magnetometer will be used to correct for the B_0 field fluctuations. To achieve these specifications, both active and passive shielding will be utilized to reduce the uncontrolled and time-varying external fields. The desired internal magnetic field will be generated by using B_0 and shim coils. Figure 2.4 shows the schematic drawing of the magnetic components of the TUCAN nEDM experiment. Each magnetic component is explained below.

Active Shielding

The magnetic environment at the location of the planned nEDM experiment at TRIUMF is dominated by a static field due to the main cyclotron at TRIUMF which can be as large as 100-400 μT, with 1 to 100 nT fluctuations due to the other external magnetic sources such as nearby beam line magnets or the displacement of large magnetic objects (e.g., the crane in the Meson Hall).

The plan for TUCAN is to reduce the static field to less than 50 μT using dedicated compensation coils and constant-current supplies, and to reduce the remaining static field and fluctuations by up to a factor of 100 through a separate set of compensation coils and current supplies, using fluxgate magnetometers for magnetic feedback. The fluxgate sensors will be placed in the region between the compensation coils and the

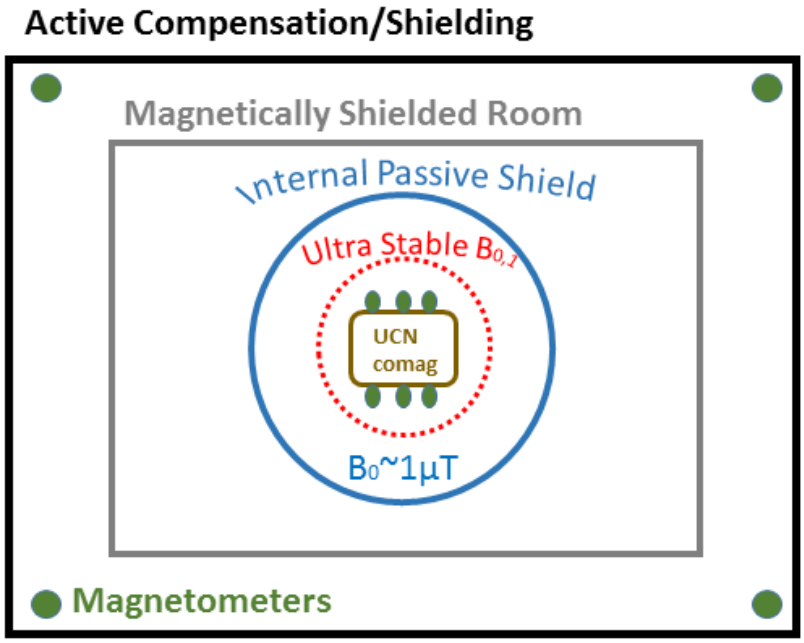

Figure 2.4: Schematic drawing for the TUCAN nEDM magnetics. From outside in: The active compensation system followed by several layers of magnetically shielded room and passive shields reduce the environmental magnetic field. The magnetometers inside the active shielding monitor the changes in the magnetic field internal to that region. The internal coil system (B_0 and B_1 coils) generate the magnetic fields for the Ramsey cycle. The UCN and the co-magnetometers are internal to the coils.

passive shields as shown in Fig. 2.4. A prototype active compensation system has been built at the University of Winnipeg based on Refs. [113, 114]. The system employs a set of coils centred around a cylindrical passive magnetic shield system, using four 3-axis fluxgates for feedback (see Fig. 2.5). Overall, the active shielding system should be able to reduce the net background magnetic field to the level of tens of nT over the passive shields.

Passive Shielding

A passive magnetic shielding system is generally composed of a multi-layer shield formed from thin shells of material with high magnetic permeability (e.g., mu-metal). The outer layers of the shield are normally cylindrical [92, 103] or form the walls of a magnetic shielded room [98, 100]. The innermost magnetic shield is normally a specially shaped shield, where the design of the coil in relation to the shield is carefully taken into account to achieve adequate homogeneity [10, 105, 106]. Figure 2.6 shows a picture of a prototype

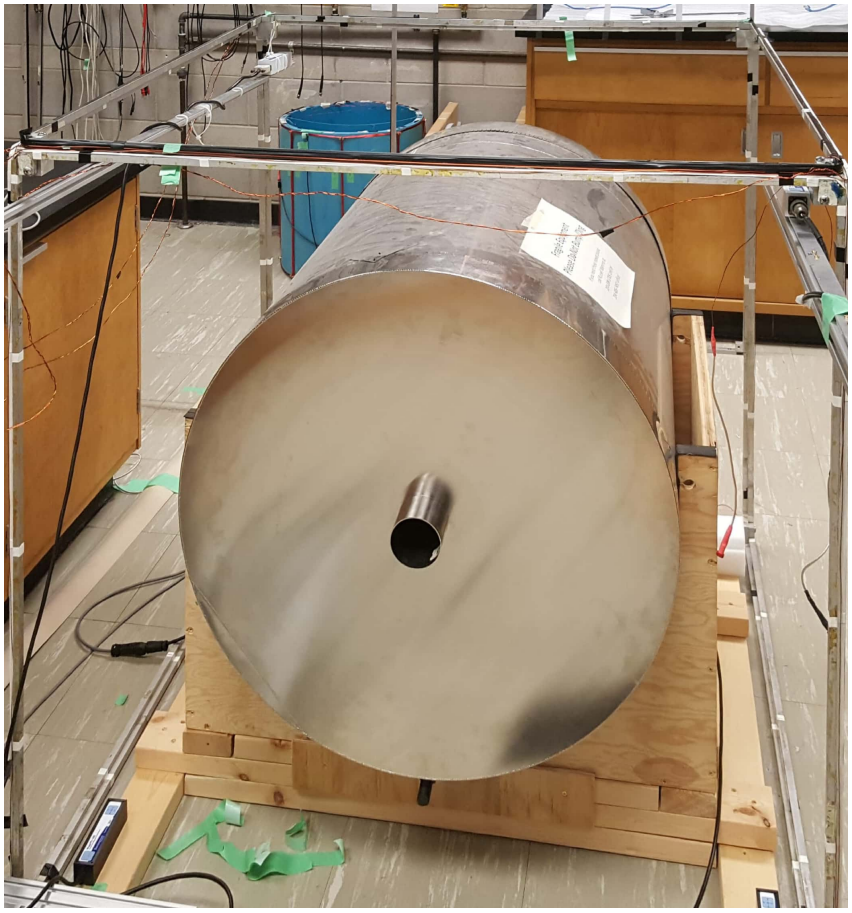

Figure 2.5: The prototype active compensation system at the University of Winnipeg.

passive shield at the University of Winnipeg, which is being used to develop precision magnetic field research for the future nEDM experiment to be conducted at TRIUMF. The shield system is a four-layer mu-metal shield formed from nested right-circular cylindrical shells with endcaps. The inner radius of the innermost shield is 18.44 cm, equal to its half-length. The radii and half-lengths of the progressively larger outer shields increase geometrically by a factor of 1.27. Each cylinder has two endcaps which possess a 7.5 cm diameter central hole. A stove-pipe of length 5.5 cm is placed on each hole, and was designed to minimize leakage of external fields into the progressively shielded inner volumes. The design is similar to another smaller prototype shield discussed in Ref. [115].

The TUCAN passive shielding system will reduce the magnetic field to the pT level. A magnetically shielded room (MSR) with a quasi-static shielding factor of $\sim$ 100,000 is sufficient to reduce the magnetic fluctuations to the $\sim$ pT level. A four-layer MSR with an inner cubic space of side-length 1.8 m and outer side-length 2.8 m produces this

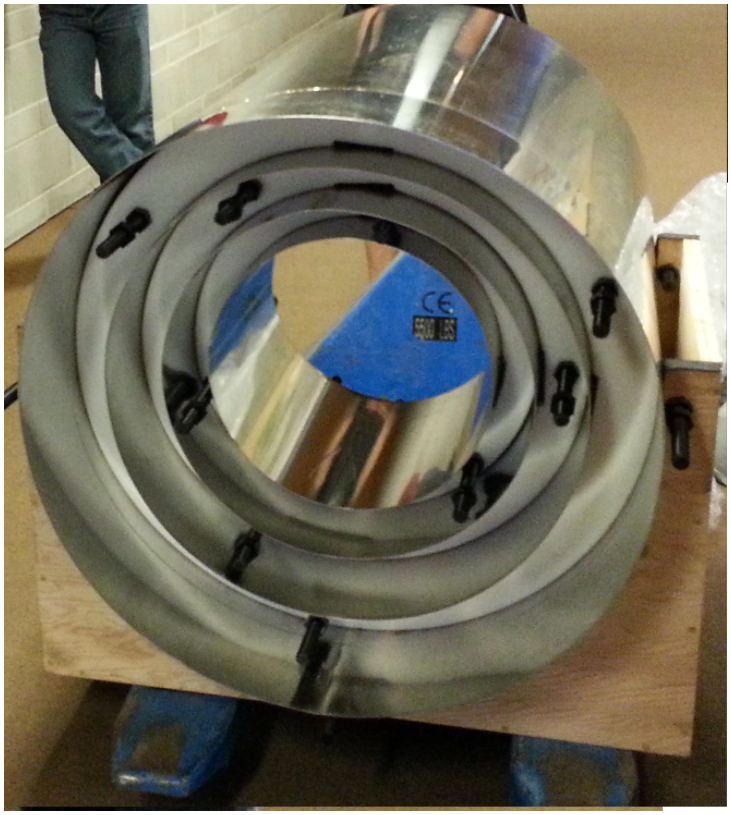

Figure 2.6: Three layers of the prototype passive magnetic shield at the University of Winnipeg. The 4th layer is not shown in this picture.

shielding factor, with mu-metal wall thicknesses 2 mm, 6 mm, 4 mm, 4 mm (inner to outer), equally spaced.

The innermost layer of the internal passive shields may also serve as a return yoke for the magnetic flux generated by the internal coils for the shield-coupled coil designs. A degaussing (idealization, equilibration) system will be used to demagnetize the shields. A combined DC shielding factor on the order of 10^6 is expected.

In the case of the shield-coupled coils, if the properties of the shields change, the internally measured magnetic field will change. Changes in the temperature of the magnetic shields give rise to a change in the magnetic permeability μ, which then causes the internal magnetic field to change. This effect is studied in Chapter 3 using two methods. The result of those measurements showed that, to achieve the 1 pT stability goal over hundreds of seconds for the internal magnetic field for the nEDM measurement, the temperature of the innermost shield should be controlled to < 0.004 K. This is very difficult to achieve. As a result, we decided to pursue the nEDM measurement using self-shielded

coils [116].

To summarize, in principle, by utilizing both active and passive shielding, the magnetic field from external sources will be significantly reduced over the volume of the nEDM cell. These are two prototype four-layer mu-metal passive shields at the University of Winnipeg. The shields are used to facilitate a variety of magnetic field R&D projects. In addition, there are three small witness cylinders which are made of the same material and annealed in the same oven as the large passive shields. The design principles behind the small shield, shielding factor measurements, and comparison to simulation are described in Ref. [115]. The witness cylinders were used to evaluate the temperature dependence of the shield material properties, which could be an important consideration for internal field stability (see Chapter 3).

Internal Coils

For internal coils, self-shielded B_0 coils and shim coils are considered, since they provide immunity from the field perturbations induced by changes in the magnetic permeability of the passive shields arising from temperature fluctuations (see chapter 3). High-precision current supplies will be used to drive all internal coils, regardless of design. AC coils will apply $\pi/2$ pulses for the UCN and comagnetometer species, to initiate free spin precession.

2.1.4 EDM Cells and High Voltage System

The nEDM measurement volume consists of two storage cells to enable simultaneous measurements with both up and down orientations of the electric field (see Fig. 2.7). The storage cells will be housed inside a non-magnetic vacuum chamber, providing insulation for the high voltage applied to the central electrode, which separates the two cells. The cells are bounded by a cylindrical wall of dielectric insulator. The insulator must have a large dielectric strength and low permittivity. An electric field of 12 kV/cm will be created between the electrodes with minimal leakage current (< 10 pA). The optical readout of the comagnetometer requires UV-transparent windows in the insulating side

wall. The use of two cells with a central electrode will allow first-order compensation of magnetic field drifts and a measurement of the magnetic field gradient.

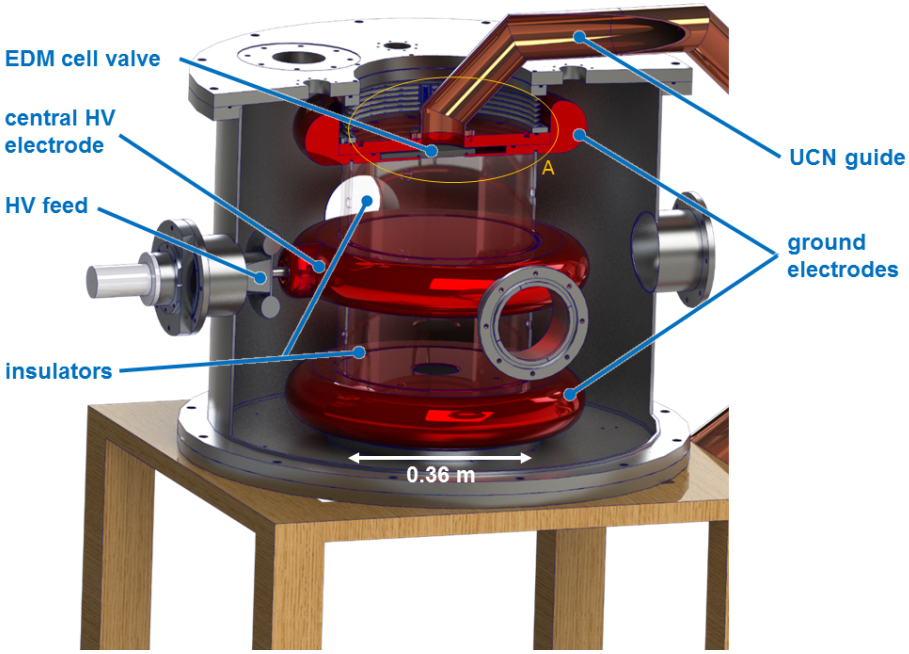

Figure 2.7: 3D drawing of the double EDM cell with vacuum chamber and UCN guides. All parts are labelled in the figure.

2.1.5 Comagnetometry

A typical problem of nEDM experiments is that if the magnetic field B_0 drifts over the course of the measurement period, it degrades the statistical precision with which d_n limit can be measured. If the magnetic field over one measurement cycle is determined to $\delta B_0 = 10$ fT, it implies an additional error of $\delta d_n \sim 10^{-26}$ e·cm (assuming an electric field of $E = 10$ kV/cm, which is reasonable for a neutron EDM experiment). Over 100 days of averaging, this would make a $\delta d_n \sim 10^{-27}$ e·cm measurement possible. Unfortunately, the magnetic field in the experiment is never stable to this level. For this reason, experiments use a comagnetometer and/or surrounding atomic magnetometers to measure and correct the magnetic field to this level [10, 114, 117]. Drifts of 1-10 pT in B_0 may be corrected using the comagnetometer technique, setting a goal magnetic stability for the B_0 field generation system in a typical nEDM experiment.

As described in Section 1.10.2, a false nEDM signal may arise due to a combination of

a magnetic field gradient along the cell (axis of symmetry of the cell is in the $\hat{z}$ direction, which is the same as the direction of the B_0 field) $\partial B_z/\partial z$, and motion in the electric field when species (neutrons and ^{199} Hg atoms) are confined in the measurement cells. The false EDM from this effect is larger for the comagnetometer atoms. Comagnetometry also offers the only way to correct for false EDMs caused by leakage currents. Each ^{199}Hg atom is polarized using optical pumping techniques. Polarized atoms are introduced into the nEDM cell at the same time as UCN, and the spin-precession frequencies are measured simultaneously. The atoms are expected to have smaller EDMs (usually due to Schiff screening) [1] than the neutrons, and so their precession frequencies may be used to normalize magnetic field drifts. The design of the ^{199}Hg comagnetometer will be similar to that employed in the previous ILL experiment [10, 118].

Chapter 3

Temperature Dependence of Magnetic Permeability

This chapter is based on a study of the sensitivity of fields generated within magnetically shielded volumes to changes in magnetic permeability presented in Ref. [102].

The previous best nEDM measurement [10, 26] showed that the dominant systematic uncertainty is related to the magnetic field homogeneity and instability. As a result, much of the research and development efforts for these experiments are focused on careful design and testing of various magnetic shield geometries with precision magnetometers [98, 114, 117, 119]. As an example, mechanical and temperature changes of the passive magnetic shielding [120, 121], and the degaussing procedure [100, 121, 122] (also known as demagnetization, equilibration, or idealization), affect the stability of the magnetic field within magnetically shielded rooms. Using a shield-coupled coil, since the B_0 coil is magnetically coupled to the innermost magnetic shield, any change in the magnetic properties of the innermost shield will result in a change in the internal magnetic field. This chapter focuses on this effect and characterize one possible source of instability: changes of the magnetic permeability μ of the material with temperature when the magnetic shield is used as a return yoke for the internal coil system. This shield-coupled coil design was used in the previous best nEDM experiment.

The chapter proceeds in the following fashion:

- The dependence of the internal field on magnetic permeability of the innermost shielding layer for a typical nEDM experiment geometry is estimated using a combination of analytical and finite element analysis techniques. This sets a scale for the stability requirement.

- New measurements of the temperature dependence of the magnetic permeability are presented. The measurements were done in two ways in order to study a variety of systematic effects that were encountered.

- Finally, the results of the calculations and measurements are combined to provide a range of temperature sensitivities that takes into account sample-to-sample and measurement-to-measurement variations.

3.1 Sensitivity of Internally Generated Field to Permeability of the Shield $B_0(\mu)$

In nEDM experiments conducted in the past, the presence of a coil inside the innermost passive shield turns the shield into a return yoke, and generally results in an increase in the magnitude of B_0. The ratio of the field inside the coil in the presence of the magnetic shield to that of the coil in free space is referred to as the reaction factor C, and can be calculated analytically for spherical and infinite cylindrical geometries [123, 124]. The key issue of interest for this work is the dependence of the reaction factor on the permeability μ of the innermost shield. Although this dependence can be rather weak, the constraints on B_0 stability are very stringent. As a result, even a small change in the magnetic properties of the innermost shield can result in an unacceptably large change in B_0.

To illustrate, consider here the model of a sine-theta surface current on a sphere of radius a, inside a spherical shell of inner radius R, thickness t, and linear permeability μ. The uniform internal field generated by this ideal spherical coil is augmented by the reaction factor in the presence of the shield, but is otherwise left undistorted. The general

reaction factor for this model is given by Eqn. (38) in Ref. [123]. In the high-μ limit, with $t \ll R$, the reaction factor can be approximated as

$$C \simeq 1 + \frac{1}{2}\left(\frac{a}{R}\right)^3 \left(1 - \frac{3}{2}\frac{R}{t}\frac{\mu_0}{\mu}\right), \tag{3.1}$$

which highlights the dependence of B_0 on the relative permeability $\mu_r = \mu/\mu_0$ of the shield.

Fig. 3.1 (upper) shows a plot of B_0 versus μ_r for coil and shield dimensions similar to the ILL nEDM experiment [10, 125]: $a = 0.53$ m, $R = 0.57$ m, and $t = 1.5$ mm. In addition to analytic calculations, the results of two axially symmetric simulations conducted using FEMM [126] are included to assess the effects of geometry and discretization of the surface current. The differences are small, suggesting that the ideal spherical model of Ref. [123] and the high-μ approximation of Eqn. (3.1) provide valuable insight for the design and analysis of shield-coupled coils.

In the first simulation, the same spherical geometry was used as for the analytic calculations. However, the surface current was discretized to 50 individual current loops, inscribed onto a sphere, and equally spaced vertically (i.e. a discrete sine-theta coil). A square wire profile of side length 1 mm was used. As shown in Fig. 3.1, this simulation gave excellent agreement with the analytic calculations. In the second simulation, a solenoid coil and cylindrical shield (length/radius = 2) were used with the same dimensions as above. Similarly, the coil was modelled as 50 evenly spaced current loops, with the distance from an end loop to the inner face of the shield endcap being half the inter-loop spacing. In the limit of tight-packing (i.e., a continuous surface current) and infinite μ, the image currents in the end caps of the shield act as an infinite series of current loops, giving the ideal uniform field of an infinitely long solenoid [127, 128]. As shown in Fig. 3.1, the result is similar to the spherical case, with differences of order one part per thousand and a somewhat steeper slope of $B_0(\mu_r)$.

Fig. 3.1 (lower) shows the normalized slope $\frac{\mu}{B_0}\frac{dB_0}{d\mu}$ of the curves from Fig. 3.1 (upper). In ancillary measurements of shielding factors (discussed briefly in Section 3.2.1), we found $\mu_r = 20,000$ to offer a reasonable description of the quasistatic shielding factor of

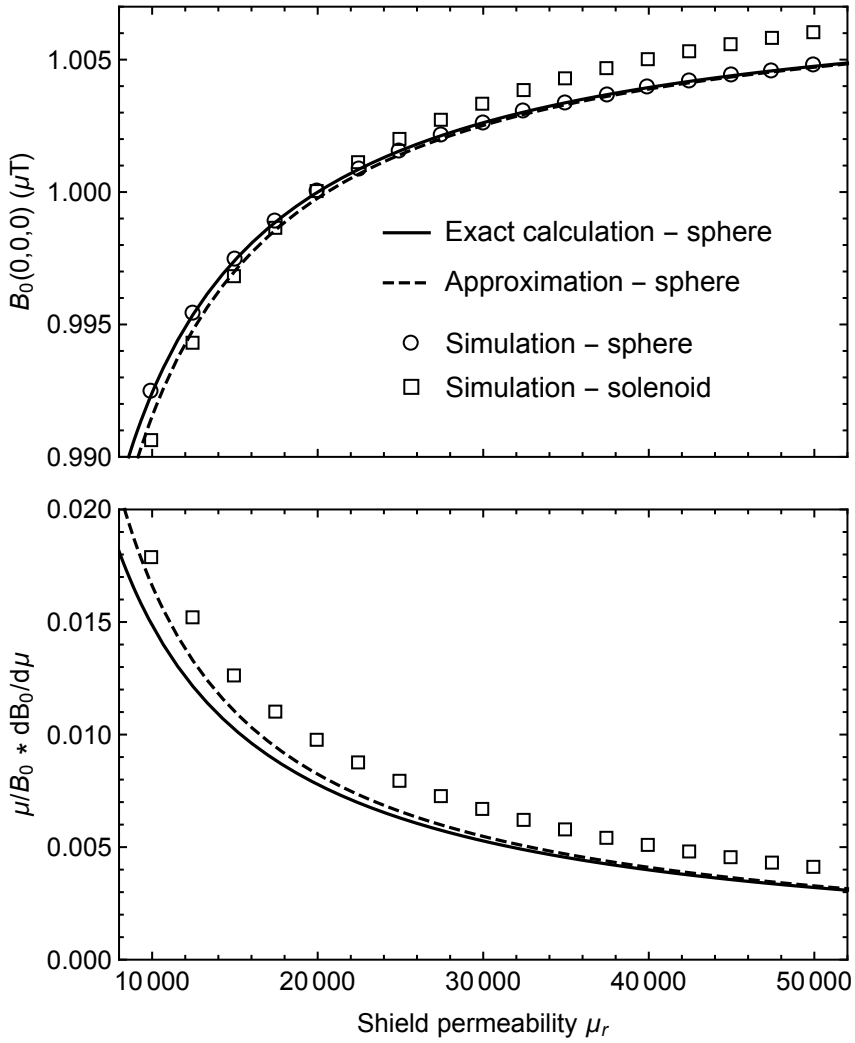

Figure 3.1: Upper: Magnetic field at the coil center as a function of magnetic permeability of the surrounding magnetic shield for a geometry similar to the ILL nEDM experiment as discussed in the text. Lower: $\frac{\mu}{B_0}\frac{dB_0}{d\mu}$ vs. permeability. The solid curve is the exact calculation for the ideal spherical coil and shield from Ref. [123]; the dashed curve is the approximation of Eqn. 3.1. The circles and squares are the FEMM-based simulations for the spherical and solenoidal geometries with discrete currents. Since the spherical simulation was in agreement with the calculation, it is omitted from the lower graph. For the exact calculation and the two simulations, currents were chosen to give $B_0 = 1$ μT at $\mu_r = 20,000$.

our shield. Using this value as the magnetic permeability of our shield material, Fig. 3.1 (lower) shows that $\frac{\mu}{B_0}\frac{dB_0}{d\mu}$ varies by about 20% (from 0.008 to 0.01) for the spherical vs. solenoidal geometries. We adopt the value $\frac{\mu}{B_0}\frac{dB_0}{d\mu} = 0.01$ as an estimate of this slope in our discussions in Section 3.3, acknowledging that the value depends on the coil and shield design.

For a high-μ innermost shield, the magnetic field lines emanating from the coil all

return through the shield. This principle can be used to estimate the magnetic field B_m inside the shield material, and our studies gave good agreement with FEA-based simulations. For the solenoidal geometry previously described and used for the calculations in Fig. 3.1, B_m is largest in the side walls of the solenoidal flux return, attaining a maximum value of 170 μT. If we assume μ_r=20,000, the H_m field is 0.007 A/m. Typically the shield is degaussed (idealized) with the internal coil energized. After degaussing, B_m must be approximately the same, since essentially all flux returns through the shield. However, the H_m field may become significantly smaller because after degaussing, it falls on the ideal magnetization curve in $B_m - H_m$ space. (For a discussion of the ideal magnetization curve, refer to Ref. [129] and see Fig. 3.2.) In principle, the H_m field could be reduced by an order of magnitude or more, depending on the steepness of the ideal magnetization curve near the origin and far from saturation. Thus $B_m = 170$ μT and $H_m < 0.007$ A/m set a scale for the relevant values for nEDM experiments. Furthermore, the field in the nEDM measurement volume, as well as in the magnetic shield, must be stable for periods of typically hundreds of seconds (corresponding to frequencies < 0.01 Hz). This sets the relevant timescale for magnetic properties most relevant to nEDM experiments.

3.2 Measurements of $\mu(T)$

3.2.1 Previous Measurements and their Relationship to nEDM Experiments

Previous measurements of the temperature dependence of the magnetic properties of high permeability alloys have been summarized in Refs. [129, 131, 132]. These measurements are normally conducted using a sample of the material to create a toroidal core, where a thin layer of the material is used in order to avoid eddy-current and skin-depth effects [132, 133]. A value of μ is determined by dividing the amplitude of the sensed B_m-field by the amplitude of the driving AC H_m-field (similar to the method described in Section 3.2.3). Normally the frequency of the H_m-field is 50 or 60 Hz. The value of μ is then quoted either at or near its maximum attainable value by adjusting the amplitude of H_m. Depending on

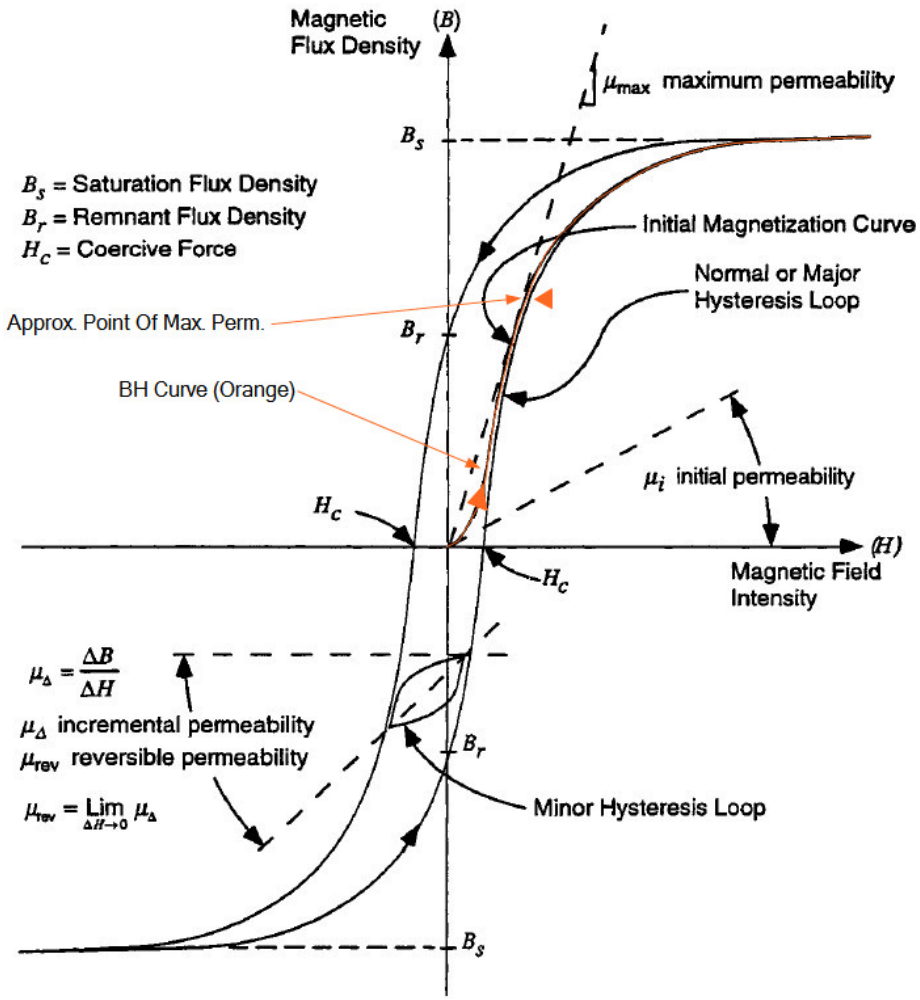

Figure 3.2: [130]The hysteresis or $B - H$ curve. Some commonly used terminology is shown. H_c or coercivity is a measure of the ability of the material to withstand external magnetic fields and is at $B = 0$. Initial permeability or μ_i is the slope of the initial magnetization curve. The initial magnetization or idealization curve is traced after degaussing the high μ material.

the details of the $B_m - H_m$ curve for the material in question, this normally means that μ is quoted for the amplitude of H_m being at or near the coercivity of the material [131, 133], resulting in large values up to $\mu_r = 4 \times 10^5$.

It is well known that μ measured in this fashion for toroidal, thin metal wound cores depends on the annealing process used for the core. There is a particularly strong dependence on the take-out or tempering temperature after the high-temperature portion of the annealing process has been completed [131–133]. Such studies normally suggest a take-out temperature of 490-500°C. This ensures that the large $\mu_r = 4 \times 10^5$ is furthermore maximal at room temperature. Slight variations around room temperature, and

assuming the take-out temperature is not controlled to better than a degree, imply a scale of possible temperature variation of μ of approximately $\left|\frac{1}{\mu}\frac{d\mu}{dT}\right| \simeq 0.3\text{-}1\%/\text{K}$ at room temperature [131, 133].

A challenge in applying these results to temperature stability of nEDM experiments is that, when used as DC magnetic shielding, the high-permeability alloys are usually operated for significantly different parameters (B_m, H_m, and frequencies).

For example, when used in a shielding configuration, the effective permeability is often measured to be typically $\mu_r = 20,000$ rather than 4×10^5. This arises in part because H_m is well below the DC coercivity. As noted in Section 3.1, a more appropriate H_m for the innermost magnetic shield of an nEDM experiment is < 0.007 A/m, whereas the coercivity is $H_c = 0.4$ A/m [133]. The frequency dependence of the measurements could also be an issue. Typically, nEDM experiments are concerned with slow drifts at < 0.01 Hz timescales whereas the previously reported $\mu(T)$ measurements are performed in an AC mode at 50-60 Hz. The goal of the experiments discussed in this chapter was to develop techniques to characterize the material properties of our own magnetic shields post-annealing, in regimes more relevant to nEDM experiments.

The magnetic shielding factors of each of our prototype four cylindrical shells, and of various combinations of them, were measured and found to be consistent with $\mu_r \sim 20,000$. In our studies of the material properties of these magnetic shields, two different approaches to measure $\mu(T)$ were pursued. Both approaches involved experiments done using witness cylinders made of the same material and annealed at the same time as the prototype magnetic shields. We therefore expect they have the same magnetic properties as the larger prototype shields, and they have the advantage of being smaller and easier to perform measurements with.

The two techniques employed to determine $\mu(T)$ were the following:

1. measuring the low-frequency AC axial magnetic shielding factor of the witness cylinder as a function of temperature, and

2. measuring the temperature dependence of the slope of a minor $B - H$ loop, using the witness cylinder as a transformer core, similar to previous measurements of the

temperature dependence of μ, but for parameters closer to those encountered in nEDM experiments.

The details and results of each technique are presented below.

3.2.2 Axial Shielding Factor Measurements

In these measurements, a witness cylinder was used as a magnetic shield. The shield was subjected to a low-frequency AC magnetic field of ~ 1 Hz. The amplitude of the shielded magnetic field B_s was measured at the center of the witness cylinder using a fluxgate magnetometer. Changes in B_s with temperature signify a dependence of the permeability μ on temperature. The relative slope of $\mu(T)$ can then be calculated using

$$\frac{1}{\mu}\frac{d\mu}{dT} = -\frac{\frac{1}{B_s}\frac{dB_s}{dT}}{\frac{\mu}{B_s}\frac{dB_s}{d\mu}}. \tag{3.2}$$

The numerator was taken from the measurements described above. The denominator was taken from finite-element simulations of the shielding factor for this geometry as a function of μ.

This measurement technique was sufficiently robust to extract the temperature dependence of the shielding factor with some degree of certainty. Possible drifts and temperature dependence of the fluxgate magnetometer offset were mitigated by using an AC magnetic field. Any temperature coefficients in the rest of the instrumentation were controlled by performing the same measurements with a copper cylindrical shell with the similar size and shape as the mu-metal witness cylinders in place of the mu-metal witness cylinder.

This technique is quite different than the usual transformer core measurements conducted by other groups. As shall be described, it offers an advantage that considerably smaller B_m and H_m fields can be accessed. Measuring the temperature dependence of the shielding factor is also considerably easier than measuring the temperature dependence of the reaction factor, since the sensitivity to changes in $\mu(T)$ is considerably larger in magnitude for the shielding factor case where $\frac{\mu}{B_s}\frac{dB_s}{d\mu} \sim -1$ compared to the reaction

factor case where $\frac{\mu}{B_0}\frac{dB_0}{d\mu} \sim 0.01$.

Experimental Apparatus for Axial Shielding Factor Measurements

The witness cylinder was placed within a homogeneous AC magnetic field. The field was created within the magnetically shielded volume of the prototype magnetic shielding system (described previously in Section 3.2.1 and chapter 2) in order to provide a controlled magnetic environment. A short solenoid inside the shielding system was used to produce the magnetic field. The solenoid has 14 turns with 2.6 cm spacing between the wires. The solenoid was designed so that the field produced by the solenoid plus innermost shield approximates that of an infinite solenoid. The magnetic field generated by the solenoid was typically 1 μT in amplitude. The solenoid current was varied sinusoidally at typically 1 Hz.

The witness cylinder was placed into this magnetic field generation system as shown schematically in Fig. 3.3. The cylinder was held in place by a wooden stand.

A Bartington fluxgate magnetometer Mag-03IEL70 [134] (low noise) measured the axial magnetic field at the center of the witness cylinder. The fluxgate was a "flying lead" model, meaning that each axis was available on the end of a short electrical lead, separable from the other axes. One flying lead was placed in the center of the witness cylinder, the axis of the fluxgate being aligned with that of the witness cylinder. The fluxgate was held in place rigidly by a plastic mounting fixture, which was itself rigidly mounted to the witness cylinder.

To increase the resolution of the measured signal from the fluxgate, a Bartington Signal Conditioning Unit (SCU) was used with a low-pass filter set to typically 10-100 Hz and a gain set to typically > 50. The signal from the SCU was demodulated by an SR830 lock-in amplifier [135] providing the in-phase and out-of-phase components of the signal. The sinusoidal output of the lock-in amplifier reference output itself was normally used to drive the solenoid generating the magnetic field. The time constant on the lock-in was typically set to 3 seconds with 12 dB/oct. rolloff.

As shall be described in this section, a concern in the measurement was changes in the

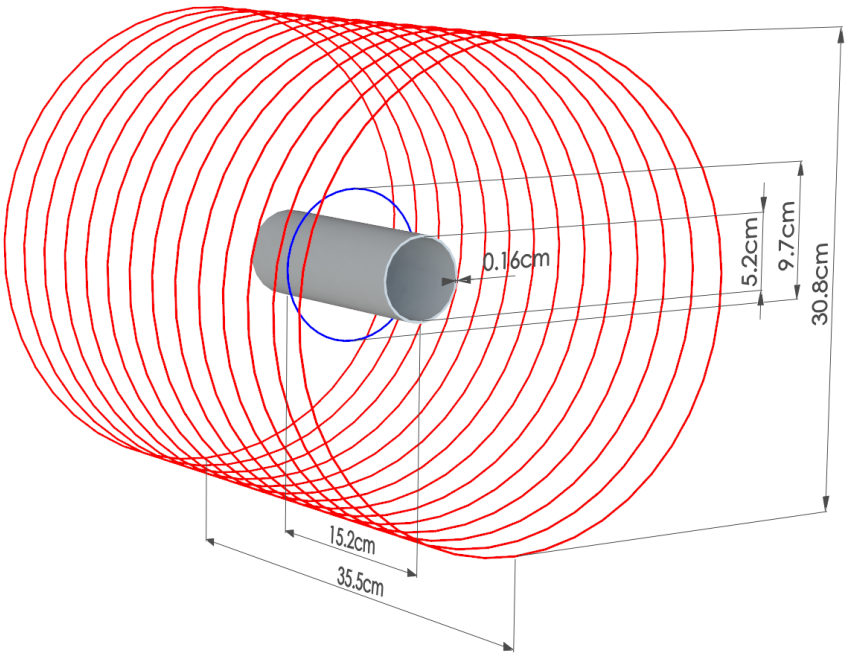

Figure 3.3: Axial shielding factor measurement setup. The witness cylinder with an inner diameter of 5.2 cm and a length of 15.2 cm is placed inside a solenoid (shown in red) with a diameter of 30.8 cm and a length of 35.5 cm, containing 14 turns. The thickness of the witness cylinder is $1/16'' = 0.16$ cm. The loop coil (shown in blue) is mechanically coupled to the witness cylinder and has a diameter of 9.7 cm.

field measured by the fluxgate that could arise due to motion of the system components, or other temperature dependences. This could generate a false slope with temperature that might incorrectly be interpreted as a change in the magnetic properties of the witness cylinder.

To address possible motion of the witness cylinder with respect to the field generation system, another driving coil (the loop coil, also shown in blue in Fig. 3.3) was wound on a plastic holder mounted rigidly to the witness cylinder. The coil was one loop of copper wire with a diameter of 9.7 cm. Plastic set screws in the holder fixed the loop coil to be coaxial with the witness cylinder.

Systematic differences in the results from the two coils (the solenoidal coil, and the loop coil) were used to search for motion artifacts. As well, some differences could arise due to the different magnetic field produced by each coil, and so such measurements could reveal a dependence on the profile of the applied magnetic field. This is described further in this section.

The temperature of the witness cylinder was measured by attaching four thermocouples at different points along the outside of the cylinder. This allowed us to observe the temperature gradient along the witness cylinder. To reduce any potential magnetic contamination, T-type thermocouples were used, which have copper and constantan conductors. (K-type thermocouples are magnetic.) Thermocouple readings were recorded by a National Instruments NI-9211 temperature input module. The magnetic field (signified by the lock-in amplifier readout) and the temperature were recorded at a rate of 0.2 Hz. Temperature variations in the experiment were driven by ambient temperature changes in the room, although forced air and other techniques were also tested. These are described further in this section.

Data and Interpretation

An example of the typical data acquired is shown in Fig. 3.4. For these data, the field applied by the solenoid coil was 1 μT in amplitude, at a frequency of 1 Hz. Fig. 3.4(a) shows the temperature of the witness cylinder over a 70-hr measurement. The temperature changes of 1.4 K are caused by daily temperature variations in the laboratory. The shielded magnetic field amplitude B_s within the witness cylinder is anti-correlated with the temperature trend as shown in Fig. 3.4(b). Here, B_s is the sum in quadrature of the amplitudes of the in-phase and out-of-phase components (most of the signal is in phase). The magnetic field is plotted as a function of temperature in Fig. 3.4(c). The slope in Fig. 3.4(c) was calculated using a linear fit to the data. The relative slope at 23°C was found to be $\frac{1}{B_s}\frac{dB_s}{dT} = -0.75\%/\mathrm{K}$.

Figs. 3.4(d), (e), and (f) show the same measurement with essentially the same settings, when the mu-metal witness cylinder was replaced by a copper cylinder. A similar relative vertical scale was used in Figs. 3.4(e) and (f) as Figs. 3.4(b) and (c). This helps to emphasize the considerably smaller relative slope derived from panel (f) compared to panel (c). A variety of measurements of this sort were carried out multiple times for different parameters such as coil current. Running the coil at the same current tests for effects due to heating of the coil, whereas running the coil at a current which equalizes the

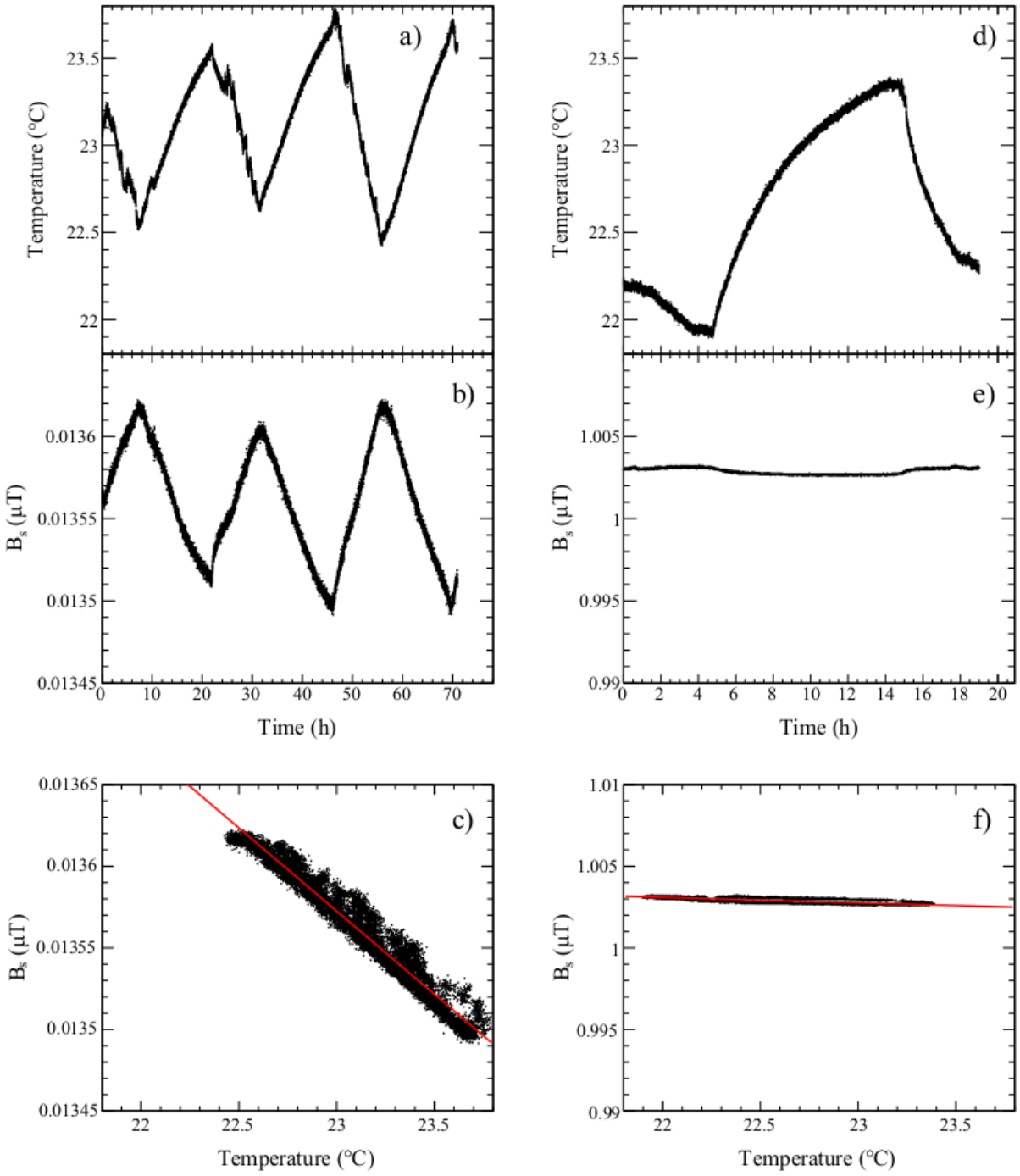

Figure 3.4: Ambient temperature and shielded magnetic field amplitude, measured over a 70 hour period. (a) temperature of the witness cylinder as a function of time. (b) magnetic field amplitude measured by fluxgate at center of witness cylinder vs. time. (c) magnetic field vs. temperature with linear fit to data giving $\frac{1}{B_s}\frac{dB_s}{dT} = -0.75\%/\mathrm{K}$ (evaluated at 23°C). In panels (d), (e), and (f), the same quantities are shown for a 20-hour run with a copper cylinder in place of the witness cylinder with the linear fit giving $\frac{1}{B_s}\frac{dB_s}{dT} = -0.03\%/\mathrm{K}$.

fluxgate signal to its value when the mu-metal witness cylinder is present tests for possible effects related to the fluxgate. For all measurements the temperature dependence of the demodulated magnetic signal was $< 0.1\%/\mathrm{K}$, giving confidence that unknown systematic effects contribute below this level.

Some deviations from the linear variation of B_s with T can be seen in the data, particularly in Figs. 3.4(a), (b), and (c). For example, when the temperature changes rapidly, the magnetic field takes some time to respond, resulting in a slope in $B_s - T$ space that is temporarily different than when the temperature is slowly varying. This is typical of the data that we acquired, that the data would generally follow a straight line if the temperature followed a slow and smooth dependence with time, but the data would not be linear if the temperature varied rapidly or non-monotonically with time. We also tried other methods of temperature control, such as forced air, liquid flowing through tubing, and thermo-electric coolers. The diurnal cycle driven by the building's air conditioning system gave the most stable method of control and the most reproducible results for temperature slopes.

As mentioned earlier, data were acquired for both the solenoid coil and the loop coil. A summary of the data is provided in Table 3.1. Repeated measurements of temperature slopes using the loop coil fell in the range $0.4\%/\mathrm{K} < |\frac{1}{B_s}\frac{dB_s}{dT}| < 1.5\%/\mathrm{K}$. Similar measurements for the solenoidal coil yielded $0.3\%/\mathrm{K} < |\frac{1}{B_s}\frac{dB_s}{dT}| < 0.8\%/\mathrm{K}$.

In general, the slopes measured with the loop coil were larger than for the solenoidal coil. This is particularly evident for measurements 6-12, which were acquired daily over the course of a few weeks alternating between excitation coils but all used the same witness cylinder and otherwise without disturbing the measurement apparatus. A partial explanation of this difference is offered by the field profile generated by each coil, and its interaction with the witness cylinder. This is addressed further in this section.

The other difference between the loop coil and the solenoidal coil was that the loop coil was rigidly mounted to the witness cylinder, reducing the possibility of artifacts from relative motion. Given that this did not reduce the range of the measured temperature slopes we conclude that relative motion was well controlled in both cases.

Trial #	$\frac{1}{B_s}\frac{dB_s}{dT}$ (%/K)	Coil type
1	-0.32	solenoid
2	-0.30	solenoid
3	-0.33	solenoid
4	-1.53	loop
5	-0.42	loop
6	-1.30	loop
7	-0.74	solenoid
8	-1.05	loop
9	-0.73	solenoid
10	-1.23	loop
11	-0.75	solenoid
12	-1.12	loop

Table 3.1: Summary of data acquired for the AC axial shielding factor measurements, in chronological order. Data with an applied field of $\sim 1-6\ \mu T$ and a measurement frequency of 1 Hz are included. Data which used daily fluctuations of the temperature from 21-24°C over a 10-80 hour period are included. Other data acquired for systematic studies are not included in the table.

Several other possible systematic effects were considered, all of which were found to give uncertainties on the measured slopes $< 0.1\%$/K. These included: thermal expansion of components including the witness cylinder itself, temperature variations of the magnetic shielding system within which the experiments were conducted, degaussing of the witness cylinder, and temperature slopes of various components e.g. the fluxgate magnetometer and the lock-in amplifier. Some of these studies are described below.

Methods of Temperature Variation In addition to ambient temperature changes, I tried other methods of forced temperature change. In one design, Tygon tubing was wrapped around the witness cylinder in a spiral pattern to flow water whose temperature could be controlled. Mechanical stability issues clearly dominated the systematic uncertainty in that measurement. When water was flowing, the flexibility of the tubing caused a movement in the witness cylinder. The motion was itself temperature-dependent since warmer water caused the tubing to become more supple. To address this effect, the tubes were replaced by copper tubing. But in this case, the challenge was to create enough contact between the tubes and the witness cylinder which was not successful. In another

design, a TEC was replaced with the tubing. The main issue with this design was that it did not provide enough cooling for the witness cylinder and also it was creating only local temperature changes on the witness cylinder. In addition, despite of using heat sinks, the heat created by the TEC itself made it very inefficient. I also tried using forced air to heat the witness cylinder. This worked rather well, but the heating had to be done slowly in order to avoid temperature gradients across the apparatus, including the witness cylinder. In the end, using the ambient temperature changes in the room gave the most reproducible results. These followed a relatively stable diurnal cycle with the function of the building's air conditioning system.

Although for most of the measurements the general trend of $B(T)$ graphs was consistent, the shape and positions of the nonlinear parts of $B-T$ graphs were changing. The changes in the B vs. temperature slope always correlate with sharper changes in the temperature with time. The effect is most pronounced when a temperature that is decreasing with time suddenly changes to increasing, or vice-versa. However, I have incorporated the uncertainty from this effect into our stated range of values.

Mechanical Stability Other potential motion artifacts due to thermal expansion of components was also considered. The thermal expansion coefficient of mu-metal is $\sim$10 ppm/K [133]. However if the witness cylinder expands uniformly in both thickness and radius, the shielding factor is to first order unchanged. In general, even unnatural asymmetric and twisting motions of the fluxgate sensor and witness cylinder tended to generate temperature slopes in the magnetic field at the level $<$ 30 ppm/K. The general homogeneity of the magnetic field at the fluxgate sensor position and of the applied magnetic field within which the witness cylinder was placed aided in minimizing motion artifacts.

As another mechanical stability study, the movement of the Bartington fluxgate flying lead due to thermal expansion was estimated. If the fluxgate flying lead move about 1 mm normal to its axis of symmetry which is parallel to the axis of the witness cylinder, the magnetic field will change about 30 ppm/K over 20 K temperature changes.

Temperature Dependence of Reaction Factor As the witness cylinder was put through its diurnal heating and cooling cycles, so too was the magnetic shield within which the apparatus was placed. Since this magnetic shield is used as a flux return, especially for the solenoidal coil, a concern could be that the measurement confounds temperature dependence of the flux return with the temperature dependence of the shielding factor of the solenoid. We want to clarify that this cannot be the case: any change in μ of the flux return will have an exceedingly small effect on the field produced by the solenoid. This is perhaps best demonstrated by Fig. 3.1, where the reaction factor in a similar cylindrical geometry is graphed as a function of μ. Based on our measurements, this limits systematic errors from such an effect to be < 200 ppm/K.

Degaussing The magnetization of the witness cylinder changes the magnetic permeability of the material and so the shielding factor changes. Our studies of degaussing the witness cylinder were consistent with studies that we will report in Section 3.2.3. Essentially, if the shields were degaussed, or if they were left for long periods of time in the small AC field generated by the solenoid, the results for temperature dependences were similar. Improper degaussing procedures were found to induce long-term drifts in the measurement, uncorrelated with temperature. We do not include such data when quoting our measurements of temperature slopes. We do think that part of the range of slopes that we measured is due to the magnetic properties of the material, and that it is possible that some of this range is yet due to insufficient degaussing on our part. This is something we plan to improve in planned future experiments on DC field stability.

Temperature Slopes of Various Components of the Apparatus The temperature coefficients of various components that could affect the measurement were also considered.

The Mag-03IEL70 Bartington magnetic field sensor has a scaling temperature coefficient of 15 ppm/K [134]. There is also temperature coefficient for the offset of these sensors, but this is irrelevant for this measurement because of the AC fields and demodulation technique used.

The SRS830 lock-in amplifier has 50 ppm/K amplitude stability [135]. To further test

this, the lock-in amplifier was connected to the coil through a 1 Ω resistor with small temperature coefficient. The voltage across the resistor was measured with the lock-in amplifier itself. Any change would then be interpreted as a change in the current supplied to the coil by the lock-in amplifier. The measured temperature dependence was always $< 0.1\%/\mathrm{K}$.

Different Witness Cylinders The manufacturer of our prototype magnetic shields provided us with three witness cylinders. All three were used in these measurements. Different cylinders possessed systematically different temperature slopes, although always within the ranges quoted above. These changes are believed to arise from the manufacturing and annealing process. It is known that the take-out temperature in the annealing process has a strong effect on the temperature slopes measured at 50 Hz [133].

Stability Test with Copper Cylinder As mentioned earlier in reference to Fig. 3.4(d), (e), and (f), the stability of the system was also tested by replacing the mu-metal witness cylinder with a copper cylinder and in all cases temperature slopes $< 0.1\%/\mathrm{K}$ were measured, giving confidence that other unknown systematic effects contribute below this level. Here the paramagnetism contribution is very small compared to the assigned uncertainty.

Based on the systematic effects that we studied, we conclude that they do not explain the ranges of values measured for $\frac{1}{B_s}\frac{dB_s}{dT}$. We suspect that the range measured is either some yet uncharacterized systematic effect, or a complicated property of the material. We use this range to set a limit on the slope of $\mu(T)$.

Geometry correction and determination of $\mu(T)$

To relate the data on $B_s(T)$ to $\mu(T)$, the shielding factor of the witness cylinder as a function of μ must be known. Finite element simulations in FEMM and OPERA were performed to determine this factor. The simulations are also useful for determining the effective values of B_m and H_m in the material, which will be useful to compare to the case for typical nEDM experiments when the innermost shield is used as a flux return.

For closed objects, such as spherical shells [123, 124], the shielding factor approaches

	$\lvert\frac{\mu}{B_s}\frac{dB_s}{d\mu}\rvert$ (simulated)	$\lvert\frac{1}{B_s}\frac{dB_s}{dT}\rvert$ (%/K) (measured)	$\frac{1}{\mu}\frac{d\mu}{dT}$ (%/K) (extracted)
Solenoidal Coil	0.42-0.50	0.3-0.8	0.6-1.9
Loop Coil	0.56-0.65	0.4-1.5	0.6-2.7

Table 3.2: Summary of OPERA and FEMM simulations and shielding factor measurements, resulting in extracted temperature slopes of μ.

infinity as $\mu \to \infty$, and $|\frac{\mu}{B_s}\frac{dB_s}{d\mu}| \to 1$. Because the witness cylinders are open ended, the shielding factor asymptotically approaches a constant rather than infinity in the high-μ limit, and as a result $|\frac{\mu}{B_s}\frac{dB_s}{d\mu}| < 1$ here. From the simulations the ratio $\frac{\mu}{B_s}\frac{dB_s}{d\mu}$ was calculated. A linear model of the material was used where $\mathbf{B_m} = \mu\mathbf{H_m}$ with μ constant.

The simulations differed slightly in their results, dependent on whether OPERA or FEMM was used, and whether the solenoidal coil or loop coil were used. Based on the simulations, the result is $|\frac{\mu}{B_s}\frac{dB_s}{d\mu}| = 0.42 - 0.50$ for the solenoidal coil, with the lower value being given by FEMM and the upper value being given by a 3D OPERA simulation, for identical geometries. This is somewhat lower than the value suggested by Ref. [136] with fits to simulations performed in OPERA, which we estimate to be 0.6. We adopt our value since it is difficult to determine precisely from Ref. [136]. For the loop coil, we determine $|\frac{\mu}{B_s}\frac{dB_s}{d\mu}| = 0.56 - 0.65$, the range being given again by a difference between FEMM and OPERA.

Combining the measurement and the simulations, the temperature dependence of the effective μ (at $\mu_r = 20,000$ which is consistent with our measurements) can be calculated by equation (3.2). The results of the simulations and measurements is presented in Table 3.2. Combining the loop coil and solenoidal coil results, we find $0.6\%/\text{K} < \frac{1}{\mu}\frac{d\mu}{dT} < 2.7\%/\text{K}$ to represent the full range for the possible temperature slopes of μ that were observed in these measurements.

As stated earlier, the simulations also provided a way to determine the typical value of B_m and H_m internal to the material of the witness cylinder. According to the simulations, the B_m amplitude was typically 100 μT and the H_m amplitude was typically 0.004 A/m. These are comparable to the values normally encountered in nEDM experiments, recalling from Section 3.1 that $H_m < 0.007$ A/m for the innermost magnetic shield of an nEDM

experiment. A caveat is that these measurements were typically conducted using AC fields at 1 Hz, as opposed to the DC fields normally used in nEDM experiments.

3.2.3 Transformer Core Measurements

An alternative technique similar to the standard method of magnetic materials characterization via magnetic induction was also used to measure changes in μ. In this measurement technique, the witness cylinder was used as the core of a transformer. Two coils (primary and secondary) were wound on the witness cylinder using multistranded 20-gauge copper wire. The windings were made as tight as possible, but not so tight as to potentially stress the material. The windings were not potted in place. Three witness cylinders were tested. Data were acquired using different numbers of turns on both the primary (N_p)and secondary (N_s) coils (from 6 to 48 on the primary, and from 7 to 24 on the secondary).

Fig. 3.5 shows a picture of one of the witness cylinders, wound as described. It also shows a schematic diagram of the measurement setup, which we now use to describe the measurement principle.

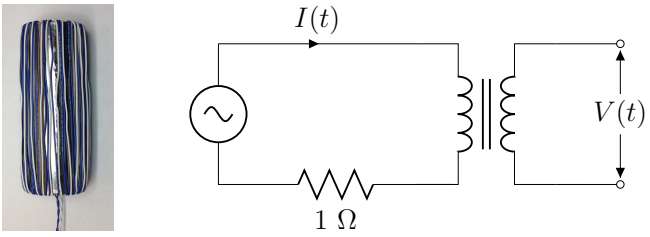

Figure 3.5: Photograph of a witness cylinder showing transformer windings (left) and schematic of the transformer measurement (right). The primary coil was driven by the sine-out of an SR830 lock-in amplifier, which was also used to demodulate induced voltage $V(t)$ in the secondary coil. The driving current $I(t)$ was sensed by measuring the voltage across a stable 1 Ω resistor.

The primary coil generated an AC magnetic field as a function of time $H(t)$, while the secondary coil was used to measure the emf induced by the time-varying magnetic flux proportional to $dB(t)/dt$. To a good approximation

$$H_m(t) = \frac{N_p I(t)}{2\pi R} \tag{3.3}$$

where N_p is the number of turns in the primary, $I(t)$ is the current in the primary, and R is the radius of the witness cylinder, and

$$\frac{dB_m(t)}{dt} = \dot{B}_m(t) = \frac{V(t)}{b\ell} \tag{3.4}$$

where $V(t)$ is the voltage generated in the secondary, and b and ℓ are the thickness and length of the witness cylinder respectively. For a sinusoidal drive current $I(t)$, and under the assumption that $B_m(t) = \mu H_m(t)$ with μ being a constant, the voltage generated in the secondary $V(t)$ should be sinusoidal and out of phase with the primary current.

The internal oscillator of an SR830 lock-in amplifier was used to generate $I(t)$. This was monitored by measuring the voltage across a 1 Ω resistor with small temperature coefficient in the primary loop. The lock-in amplifier was then used to demodulate $V(t)$ into its in-phase V_X and out-of-phase V_Y components (or equivalently $\dot{B}_m(t)$ being demodulated into $\dot{B}_{m,X}$ and $\dot{B}_{m,Y}$, as in equation (3.4)). The experiment was done at 1 Hz with $H_m(t)$ as small as possible, typically 0.1 A/m in amplitude, to measure the slope of the minor B_m-H_m loops near the origin of the B_m-H_m space.

The temperature of the core was measured continuously using the same thermocouple arrangement described previously. Measurements of V_Y as a function of temperature would then signify a change in μ with temperature. In general, we used ambient temperature variations for the measurements, similar to the procedure used for our axial shielding factor measurements.

The naive expectation is that the out-of-phase V_Y component should signify a nonzero μ, and the in-phase V_X component should be zero. In practice, due to a combination of saturation, hysteresis, eddy-current losses, and skin-depth effects, the V_X component is nonzero. It was found experimentally that keeping the amplitude of $H_m(t)$ small compared to the apparent coercivity ($\sim$ 3 A/m for the 0.16 cm thick material at 1 Hz frequencies) ensured that the V_Y component was larger than the V_X component. This is displayed graphically in Fig. 3.6, where the dependence of $\dot{B}_{m,Y}$ and $\dot{B}_{m,X}$ on the amplitude of the applied $H_m(t)$ is displayed, for a driving frequency of 1 Hz. Clearly the value of $\dot{B}_{m,X}$ can be considerable compared to $\dot{B}_{m,Y}$, for larger H_m amplitudes near the

coercivity. At larger amplitudes, the material goes into saturation. Both $\dot{B}_{m,Y}$ and $\dot{B}_{m,X}$ eventually decrease as expected at amplitudes much greater than the coercivity.

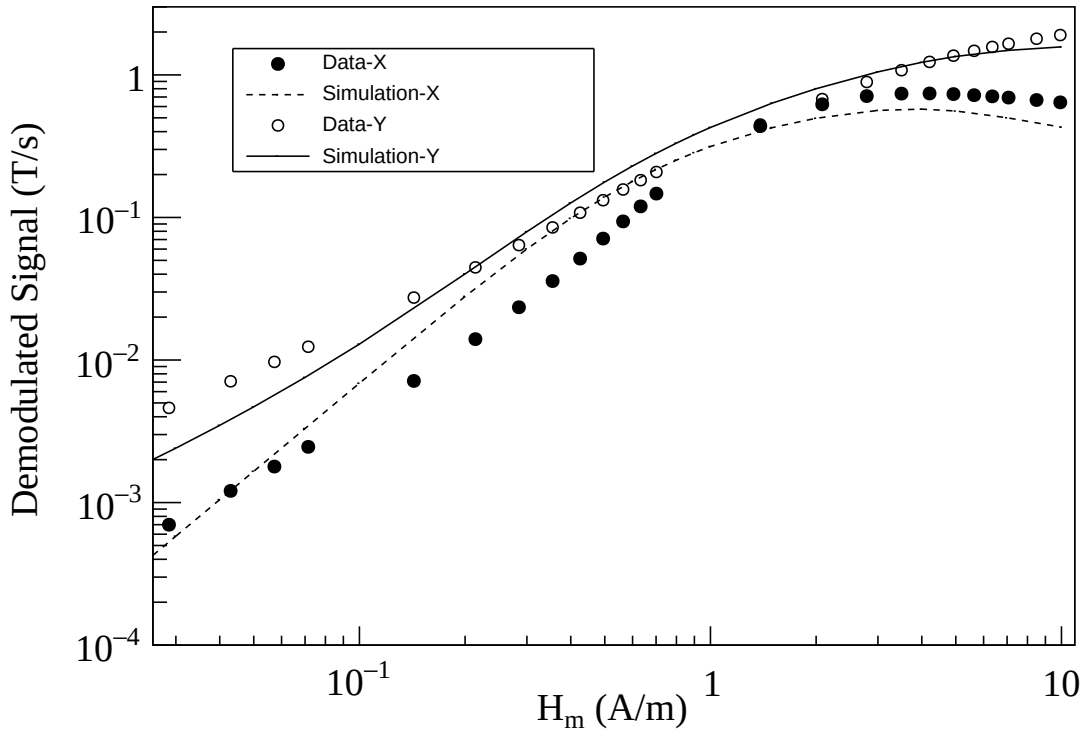

Figure 3.6: $\dot{B}_{m,X}$ and $\dot{B}_{m,Y}$ as a function of amplitude of the applied H_m field at 1 Hz. Points show the acquired data. Curves display the simulation based on the model described in the text.

To understand the behavior in Fig. 3.6, a theoretical model of the hysteresis based on the work of Jiles [137] was used. The anhysteretic magnetization of a material in the presence of magnetic field could be written as the solution of

$$M_{an}(H) = M_s \ell \left(\frac{H + \alpha M_{an}(H)}{a} \right) \tag{3.5}$$

where $\ell = \ell(x) = \coth(x) - 1/x$ is the Langevin function , M_s is the saturation magnetization, α is a coupling coefficient, and $a = k_B T/\mu_0 \langle m \rangle$ with k_B being the Bolzmann constant, T being the temperature, μ_0 being the permeability of free space, and $\langle m \rangle$ being the effective domain size. The equation for hysteresis can then be derived from the

energy-balance equation

$$\mu_0 \int M_{an} dH_e = \mu_0 \int M dH_e + \mu_0 k\delta(1-c) \int \frac{dM_{irr}}{dH_e} \ , \tag{3.6}$$

which means, in an initially demagnetized material, hysteresis can appear as a change in total demagnetization, or be dissipated due to irreversible changes in magnetization M_{irr} (hysteresis loss). Here the first term of the right-hand side is the contribution to the magnetostatic energy, and the second term on the right-hand side is the dissipation loss due to pinning. In this equation $H_e = H + \alpha M$, the coefficient k is the pinning parameter which determines the amount of energy dissipated, and δ is a directional parameter which ensures that energy is always lost through dissipation. The coefficient c is a measure of the amount of reversible change in magnetization. The total magnetization consists of two parts including reversible and irreversible magnetization $M = M_{\rm irr} + M_{\rm rev}$.

Now including both classical (eddy current) losses and anomalous losses we get

$$\begin{aligned} &\left(\frac{\mu_0 d^2}{2\rho\beta}\frac{dH}{dt}\right)\left(\frac{dM}{dH}\right) + \left(\frac{GdW\mu_0 H_0}{\rho}\right)^2 \left(\frac{dH}{dt}\right)^2 \left(\frac{dM}{dH}\right)^{3/2} \\ &+ \left[k\delta - \alpha\left(M_{an}(H) - M(H) + k\delta c\frac{dM_{an}}{dH_e}\right)\right]\left(\frac{dM}{dH}\right) \\ &- \left(M_{an}(H) - M(H) + k\delta c\frac{dM_{an}}{dH_e}\right) = 0 \ , \end{aligned} \tag{3.7}$$

where ρ is the resistivity, d is the cross-sectional dimension in meters, β is a geometric factor, G is a dimensionless constant of value 0.1356, w is the width of the laminations, and H_0 is a parameter representing the fluctuating internal potential experienced by domain walls. This equation can be solved numerically.

We adjusted the parameters based on our measurements of B_m-H_m loops including the initial magnetization curve. These measurements were performed separately from our lock-in amplifier measurements, using an arbitrary function generator and a digital oscilloscope. The measurements were done at frequencies from 0.01 to 10 Hz. It was found that the frequency dependence predicted by Ref. [137] gave relatively good agreement with the measured B_m-H_m loops once the five original (Jiles-Atherton [138, 139]) parameters

were tuned.

For the parameters of the (static) Jiles-Atherton model, we used $B_s = 0.45$ T, $a = 3.75$ A/m, $k = 2.4$ A/m, $\alpha = 2 \times 10^{-6}$, $c = 0.05$, which were tuned to our B_m-H_m curve measurements. For classical losses, we used the parameters $\rho = 5.7 \times 10^{-7}$ Ω·m, $d = 1.6$ mm (the thickness of the material), and $\beta = 6$ (geometry factor). These parameters were not tuned, but taken from data sheets and measurements. For anomalous losses we used the parameters $w = 0.005$ m and $H_0 = 0.0075$ A/m, which we also did not tune, instead relying on the tuning performed in Ref. [137].

These parameters were then used to model the measurement presented in Fig. 3.6, including the lock-in amplifier function. As shown in Fig. 3.6, trends in the measurements and simulations are fairly consistent. The sign of $\dot{B}_{m,X}$ relative to $\dot{B}_{m,Y}$ is also correctly predicted by the model (we have adjusted them both to be positive, for graphing purposes. One of the two should be of opposite sign, independent of the direction of the windings.). We expect that with further tuning of the model, even better agreement could be achieved.

The model of Ref. [137] makes no prediction of the temperature dependence of the parameters. Ideally, the temperature dependence of $\dot{B}_{m,Y}$ and $\dot{B}_{m,X}$ under various conditions could be used to map out the temperature dependence of the parameters. However, this is beyond the scope of the present work.

We make the simplifying assumption that temperature dependence of $\dot{B}_{m,Y}$ may be approximately interpreted as the temperature dependence of a single parameter μ, i.e. that

$$\frac{1}{\dot{B}_{m,Y}} \frac{d\dot{B}_{m,Y}}{dT} = \frac{1}{\mu} \frac{d\mu}{dT}. \tag{3.8}$$

This is justified in part by our selection of measurement parameters (the amplitude of $H_m = 0.1$ A/m and a measurement frequency of 1 Hz) which ensure that $\dot{B}_{m,Y}$ dominates over $\dot{B}_{m,X}$.

We assign no additional systematic error for this simplification, and all our results are subject to this caveat. We comment further that the same caveat exists in our measurements of the axial shielding factor (presented in Section 3.2.2). In that case the in-phase component dominates the demodulated fluxgate signal. In a sense, measuring

Trial #	$\frac{1}{\dot{B}_{m,Y}}\frac{d\dot{B}_{m,Y}}{dT}$ (%/K)	core used
1	0.15	α
2	0.03	α
3	0.04	α
4	0.06	α
5	1.07	β
6	0.93	β
7	0.88	β
8	0.88	β
9	0.09	α
10	1.23	β
11	2.15	β
12	1.85	β
13	1.20	β
14	0.77	γ

Table 3.3: Summary of data acquired for the transformer core measurements. Three different witness cylinders, arbitrarily labeled α, β, and γ, were used for the measurements. A 1 Hz excitation frequency was used with amplitudes for H_m ranging from 0.1 to 0.3 A/m. Fluctuations in the temperature ranged from 21-24°C and measurement times over a 10-80 hour period are included. Other data acquired for systematic studies are not included in the table.

$\mu(T)$ itself is always an approximation, because it is actually the parameters of minor loops in a hysteresis curve which are measured. In reality, our results may be interpreted as a measure of the temperature-dependence of the slopes of minor loops driven by the stated H_m.

Measurements of $\frac{1}{\dot{B}_{m,Y}}\frac{d\dot{B}_{m,Y}}{dT}$ as a function of T were made. In general, the data mimicked the behavior of the axial shielding factor measurements, giving a similar level of linearity with temperature as the data displayed in Fig. 3.4. Other similar behaviors to those measurements were also observed, for example: (a) when the temperature slope changed sign, $\dot{B}_{m,Y}$ would temporarily give a different slope with temperature, (b) the measured value of $\frac{1}{\dot{B}_{m,Y}}\frac{d\dot{B}_{m,Y}}{dT}$ depended on a variety of factors, most notably which of the three witness cylinders was used for the measurement, and on differences between subsequent measurements using the same cylinder.

Table 3.3 summarizes our measurements of the relative slope $\frac{1}{\dot{B}_{m,Y}}\frac{d\dot{B}_{m,Y}}{dT}$ for a variety of trials, witness cylinders, and numbers of windings. The data show a full range of

$0.03 - 2.15\%/\mathrm{K}$ for $\frac{1}{\mu}\frac{d\mu}{dT} = \frac{1}{\dot{B}_{m,Y}}\frac{d\dot{B}_{m,Y}}{dT}$, again naively assuming the material to be linear as discussed above. The sign of the slope of $\mu(T)$ was the same as the axial shielding factor technique.

A dominant source of variation between results in this method arose from properties inherent to each witness cylinder. One of the cylinders (referred to as β in Table 3.3) gave temperature slopes consistently larger $\frac{1}{\mu}\frac{d\mu}{dT} \sim 0.88 - 2.15\%/\mathrm{K}$ than the other two $\frac{1}{\mu}\frac{d\mu}{dT} \sim 0.03 - 0.77\%/\mathrm{K}$ (referred to as α and γ), with some evidence that γ had a larger slope than α). We expect this indicates some difference in the annealing process or subsequent treatment of the cylinders, although to our knowledge the treatment was controlled the same as for all three cylinders. Since our goal is to provide input to future EDM experiments on the likely scale of the temperature dependence of μ that they can expect, we phrase our result as a range covering all these results.

Detailed measurements of the effect of degaussing were conducted for this geometry. The ability to degauss led us ultimately to select a larger number of primary turns (48) so that we could fully saturate the core using only the lock-in amplifier reference output as a current source. A computer program was used to control the lock-in amplifier in order to implement degaussing. A sine wave with the measurement frequency (typically 1 Hz) was applied at the maximum lock-in output power. Over the course of several thousand oscillations, the amplitude was decreased linearly to the measurement amplitude (~ 0.1 A/m). After degaussing with parameters consistent with the recommendations of Refs. [100, 121], the measured temperature slopes were consistent with our previous measurements where no degaussing was done.

Other systematic errors found to contribute at the $< 0.1\%/\mathrm{K}$ level were: motion of the primary and secondary windings, stability of the lock-in amplifier and its current source, and stability of background noise sources.

To summarize, the dominant systematic effects arose due to the different similarly prepared cores giving different results, and due to reproducibility variations in the measured slopes in multiple measurements on the same core. The second of these is essentially the same error encountered in our axial shielding factor measurements. We expect it

has the same source; it is possibly a property of the material, or an additional unknown systematic uncertainty.

3.3 Relationship to nEDM experiments

Neutron EDM experiments are typically designed with the DC coil magnetically coupled to the innermost magnetic shield. As discussed in Section 3.1, if the magnetic permeability of the shield changes, this results in a change in the field in the measurement region by an amount $\frac{\mu}{B_0}\frac{dB_0}{d\mu} = 0.01$.

The temperature dependence of μ has been constrained by two different techniques using open-ended mu-metal witness cylinders annealed at the same time as our prototype magnetic shields. We summarize the overall result as $0.0\%/\mathrm{K} < \frac{1}{\mu}\frac{d\mu}{dT} < 2.7\%/\mathrm{K}$, where the range is driven in part by material properties of the different mu-metal cylinders, and in part by variation in the measurements (e.g. those seen in Tables 3.1 and 3.3 for subsequent measurements).

We note the following caveats in relating this measurement to nEDM experiments:

- Although the measurement techniques rely on considerably larger frequencies and different H_m-fields than those relevant to typical nEDM experiments, we think it reasonable to assume the temperature dependence of the effective permeability should be of similar scale. For frequency, both techniques typically used a 1 Hz AC field, whereas for nEDM experiments the field is DC and stable at the 0.01 Hz level. Furthermore, in one measurement technique the amplitude of H_m was ~ 0.004 A/m and in the other was ~ 0.1 A/m. For nEDM experiments $H_m < 0.007$ A/m and is DC.

- Both measurement techniques extract an effective μ that describes the slope of minor loops in B_m-H_m space. A more detailed treatment would include a more comprehensive account of hysteresis in the material, which is beyond the scope of this work.

Our measurement of $0.0\%/\mathrm{K} < \frac{1}{\mu}\frac{d\mu}{dT} < 2.7\%/\mathrm{K}$ and the generic EDM experiment

sensitivity of $\frac{\mu}{B_0}\frac{dB_0}{d\mu} = 0.01$ give a temperature dependence of the magnetic field in a typical nEDM experiment of $\frac{dB_0}{dT} = 0 - 270$ pT/K. To achieve a goal of ~ 1 pT stability in the internal field for nEDM experiments, the temperature of the innermost magnetic shield in the nEDM experiment should then be controlled to the < 0.004 K level if the worst-case dependence is to be taken into account. This represents a potentially challenging design constraint for future nEDM experiments.

As noted by others [21], the use of self-shielded coils to reduce the coupling of the B_0 coil to the innermost magnetic shield is an attractive option for EDM experiments. The principle of this technique is to have a second coil structure between the inner coil and the shield, such that the net magnetic field generated by the two coils is uniform internally but greatly reduced externally. For a perfect self-shielded coil, the field at the position of the magnetic shield would be zero, resulting in perfect decoupling, which is to say a reaction factor that is identically unity. For ideal geometries, such as spherical coils [140–142] or infinitely long sine-phi coils [143–145], the functional form of the inner and outer current distributions are the same, albeit with appropriately scaled magnitudes and opposite sign. More sophisticated analytical and numerical methods have been used extensively in NMR and MRI to design self-shielded gradient [146, 147], shim [148, 149], and transmit coils [145, 150], and should be of value in the context of nEDM experiments, as well.

3.4 Conclusion

In the axial shielding factor measurement, we found $0.6\%/\text{K} < \frac{1}{\mu}\frac{d\mu}{dT} < 2.7\%/\text{K}$, with the measurement being conducted with a typical H_m-amplitude of 0.004 A/m and at a frequency of 1 Hz. In the transformer core case, we found $0.0\%/\text{K} < \frac{1}{\mu}\frac{d\mu}{dT} < 2.2\%/\text{K}$, with the measurement being conducted with a typical H_m-amplitude of 0.1 A/m and at a frequency of 1 Hz.

The primary caveat to these measurements is that both measurements (transformer core and axial shielding factor) do not truly measure μ. Rather they measure observables

related to the slope of minor hysteresis loops in B_m-H_m space. They would be more appropriately described by a hysteresis model like that of Jiles [137], but to extract the temperature dependence of all the parameters of the model is beyond the scope of this work. Instead we acknowledge this fact and relate the temperature dependence of the effective μ measured by each experiment.

We think it is interesting and useful information that the two experiments measure the same scale and sign of the temperature dependence of their respective effective μ's. This is a principal contribution of this work.

In future work, we plan to measure $B_0(T)$ directly for nEDM-like geometries using precision atomic magnetometers. We anticipat based on the present work that self-shielded coil geometries will achieve the best time and temperature stability. The R&D towards self-shielded coils so far has resulted in three summer student projects and an honours thesis [116].

Chapter 4

UCN Facility at TRIUMF

The vertical UCN cryostat at TRIUMF was developed and tested at KEK-RCNP [151, 152]. This source is referred to as the vertical UCN source because the UCN exit the source vertically. In October 2016, the cryostat was shipped to TRIUMF, and in 2017 it was installed at a dedicated spallation neutron source for further UCN experiments. The main purpose of the initial experiments were for a better understanding of the vertical UCN source, which would guide the design of the next generation UCN source for higher statistics. The cyclotron at TRIUMF provides up to 40 μA of proton beam that can be diverted onto a tungsten spallation target. The vertical UCN source is placed above the target and is surrounded by graphite blocks serving as neutron reflectors.

The vertical source was modified to fulfill the safety requirements at TRIUMF. The modifications included installing pressure relief valves on the cryostat and the UCN guides, and additional radiation shielding. The extra shielding required longer UCN guides compared to RCNP. The vertical source is currently in the Meson Hall experimental area. A map of TRIUMF displaying the location of Meson Hall is shown in Fig. 4.1.

The unique feature of the UCN source at TRIUMF is the combination of spallation neutrons and superfluid helium for UCN production. The important elements of the UCN facility at TRIUMF are described below.

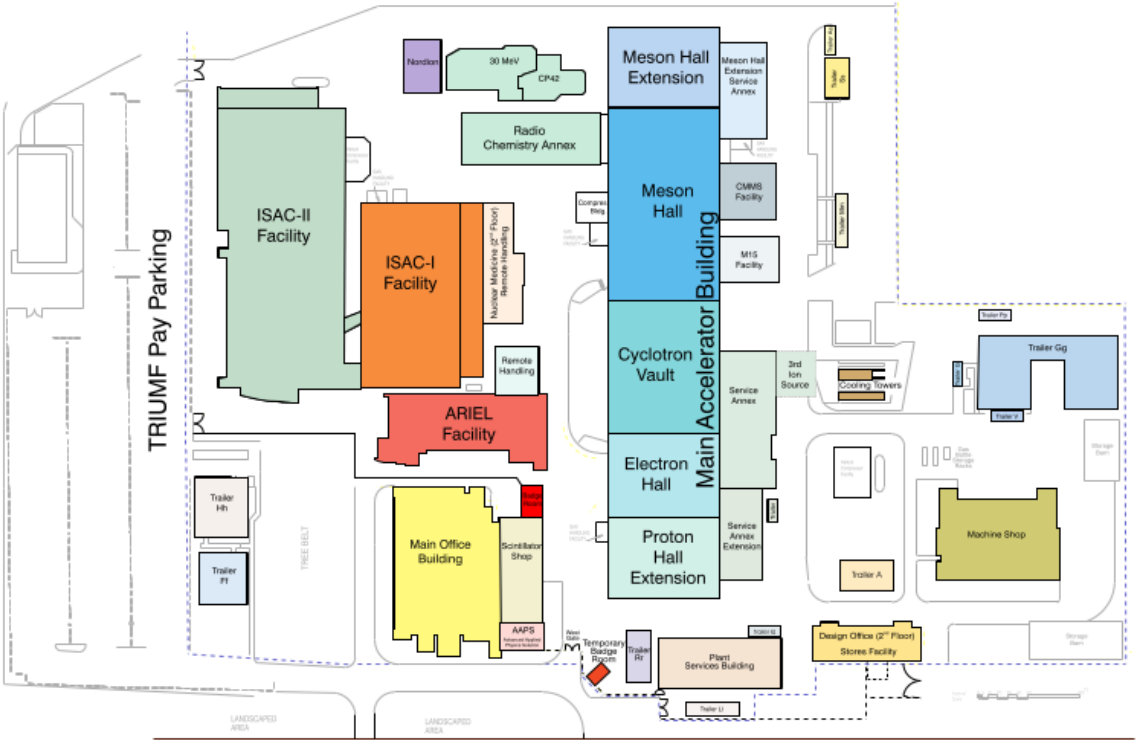

Figure 4.1: A map of TRIUMF. The UCN facility is located at the Meson Hall area shown in Blue.

4.1 Proton Beam-line for UCN Facility (BL1U)

TRIUMF produces negatively charged hydrogen ions H^- from an ion source. The ions are then accelerated in the 520 MeV cyclotron in an outward spiral trajectory. A thin graphite stripper foil removes the electrons from the hydrogen ion resulting in protons which pass through. The positively charged proton is deflected outward due to the magnetic field, and is directed to a proton beam-line. Figure 4.2 shows the beam line (BL) delivering protons from the cyclotron to the UCN facility.

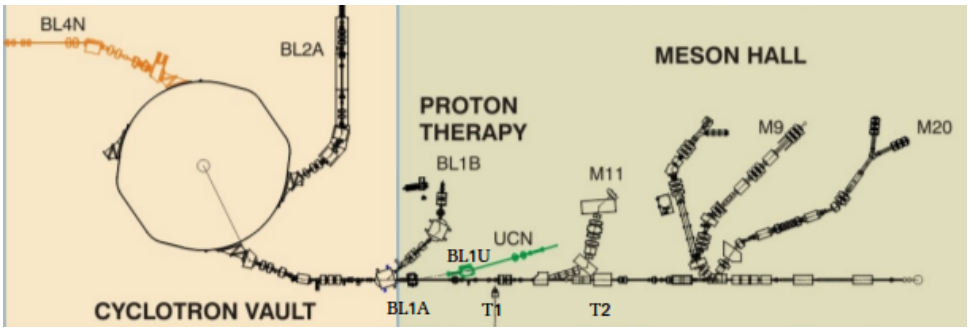

Figure 4.2: TRIUMF cyclotron and the three beam-lines.

The 120 μA beam (BL1A) enters the Meson Hall, normally delivering protons at 480 MeV to two target systems: T1 and T2 for the μSR experiments. Beam-line 1B (BL1B) separates off BL1 at the edge of the cyclotron vault, and provides international users with the Proton Irradiation Facility (PIF), which mimics space radiation for testing computer chips. The new BL1U [153] (shown in green in Fig. 4.2) provides beam to the UCN source. BL2A provides 480 MeV proton beams for the targets that produce exotic ion beams for the ISAC facilities.

The macrostructure of BL1A is in pulses with approximately 1 ms periods of beam followed by a 50-100 μs periods of no beam. The structure is shown schematically in Fig. 4.3 [154]. A kicker magnet delivers 1/3 of the beam from BL1A onto the septum magnet and onward to BL1U and transport it to a conventional dipole (bender) magnet (see the bottom panel of Fig. 4.3 and Fig. 4.4).

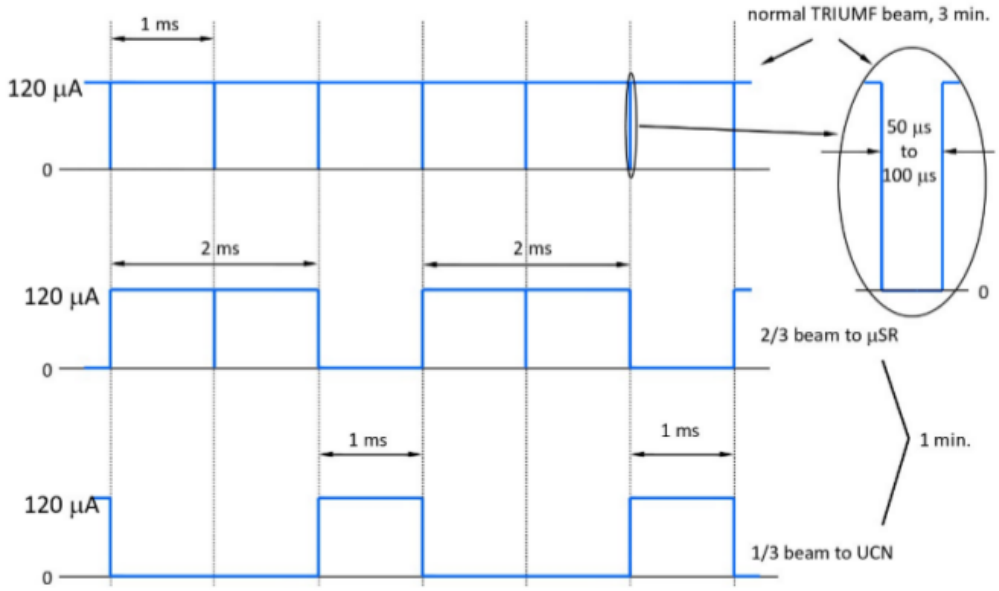

Figure 4.3: UCN beam structure. The top graph shows the 120 μA BL1A in 1 ms period of beam followed by a 50-100 μs of no beam. The middle graph shows the same beam when the kicker magnet is on and 2/3 of the beam goes to μSR experiment. The bottom graph shows the 1/3 of the beam that goes to the UCN area.

The vertical UCN cryostat is above the tungsten target. The target is designed for a maximum of 40 μA beam on target. As a result, only one third of the beam can go to the UCN experimental area, and the rest is shared with other users (see Fig. 4.3).

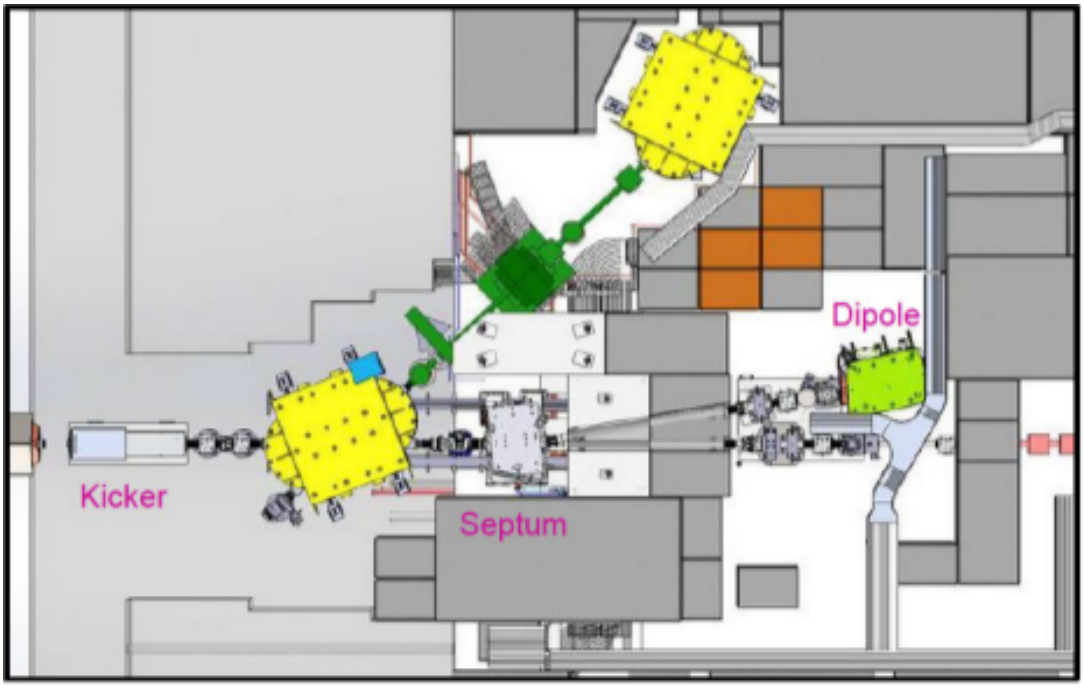

Figure 4.4: The kicker, septum and dipole (bender) magnets define the front two sections of BL1U.

After the bender magnet, the beam passes through a cored shielding block, and reaches the two quadrupole magnets, providing the final focus of the beam onto a 12 cm thick tungsten spallation target. The target is located inside a hermetically-sealed target crypt, which also envelops the beam-line exit window that defines the end of BL1U. Upstream of the beam-line window, there is a collimator to reduce the halo from the proton beam, as well as to help reduce the flux of neutrons and photons streaming back into the beam-line from the target region. The collimator also increases the impedance for the passage of gas arising from a target or window failure, to allow time for the cyclotron fast valves to close. The last part of the beam-line also contains a variety of beam position and current monitors. The spallation target and UCN source, located downstream of the beam line-exit window, are enclosed in a large shielding pyramid shown in Fig. 4.5.

4.2 Tungsten Spallation Target

The spallation target is located at the downstream end of BL1U. The UCN spallation target is composed of a series of rectangular blocks, adding up to one stopping length of

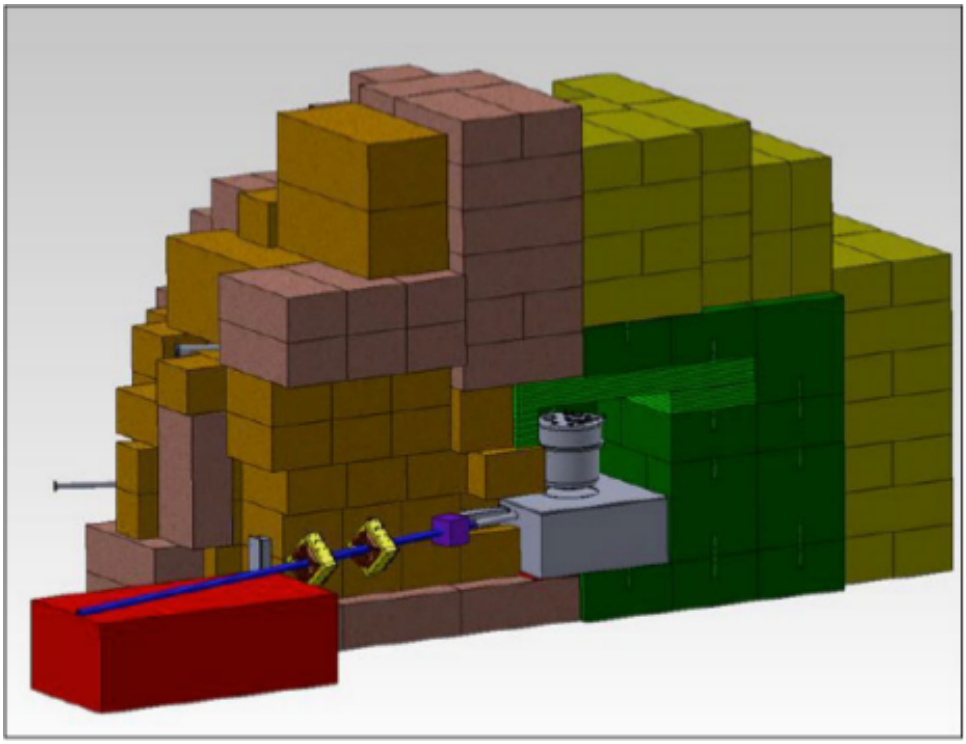

Figure 4.5: Two quadrupole magnets which focus the proton beam onto a 12 cm thick tungsten spallation target, located inside a hermetically-sealed target crypt. Also shown is the UCN shielding pyramid, which encases both the spallation target and the UCN source, and is designed to meet the dose rate requirements specified by the TRIUMF Safety Group.

tungsten (11 cm for 480 MeV protons). This geometry is very similar to (and motivated by) a neutron spallation target design used previously at KEK (KENS facility) [155]: five blocks of tungsten with tantalum plating constitute the target with 78 mm height and 57 mm width, three with 20 mm length in the beam direction, two with 30 mm length (see Fig. 4.6). The target has a support and cooling system, designed to allow for remote-handling and ease of servicing. The target-cooling and remote-handling systems are designed for an instantaneous proton current of 40 μA (10 μA time-averaged).

The target is water cooled. A water flow of approximately 0.8 L/s cools the target. Horizontal channels around the blocks create a uniform flow. To reduce the beam absorption in the water the last two blocks are thicker. Cooling water corrode tungsten. Therefore, a coating of tantalum with a thickness of < 0.1 mm prevents corrosion by the water-cooling system. The estimated lifetime of the target is longer than 10 years. An extraction system allows to exchange the target when necessary.

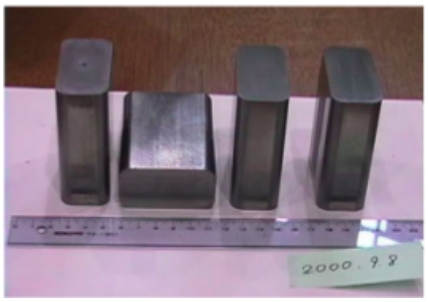

(a)

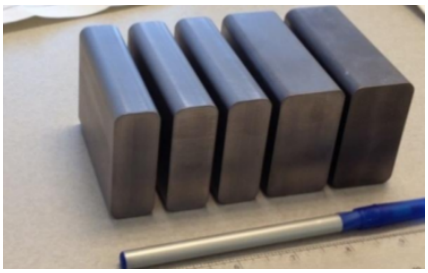

(b)

Figure 4.6: (a) Tungsten Target Blocks from the spallation target at KEK. The target blocks are plated with tantalum. (b) Present design of the tungsten spallation target at the TRIUMF UCN facility. The target blocks have a cross-section of 5.7×7.8 cm^2 , and thicknesses of 2.0, 2.0, 2.0, 3.0, and 3.0 cm, respectively.

4.3 Vertical UCN Source at TRIUMF

Neutrons are produced via proton-induced spallation off a tungsten target. Spallation is a nuclear reaction where high energy particles interact with the atomic nucleus. This creates many high-energy neutrons and less gamma radiation per neutron than fission. Since the temperature of the superfluid helium is crucial, the heat load should be kept as small as possible. Two effects dominate the heat load: (1) heating by prompt γ radiation and neutrons; and (2) residual heating by radioactive decays of materials activated by neutron capture. Any heat deposited in the converter vessel and the connected UCN guide will contribute to the heat load on the He-II, so they should be thin-walled and made out of a material with low density, low atomic number, and low neutron-absorption cross section. Additionally, the vessel and UCN guide should be leak-tight for superfluid helium, have a high optical potential for UCN, or allow coating with a suitable material. The cold- and thermal-moderator vessels have less direct impact on the heat load into the UCN converter, but secondary particles from (n, γ) reactions and radioactive decays can still contribute.

The target is surrounded by several blocks of lead and graphite. The fast neutrons are reflected, moderated, enter the room temperature (300 K) D_2O moderator, and become thermal neutrons with an average energy of 0.025 eV, or a speed of 2.2 km/s. To slow the fast neutrons down via elastic scattering we need a moderator with mass close to that of the free neutron. H_2O will not work since hydrogen has a large neutron absorption

cross-section. Therefore D_2O is a great choice as a neutron moderator. Heavy water ice at 10 K is used as a cold moderator. After passing through the warm D_2O, thermal neutrons enter the cold moderator and become cold neutrons. These neutrons have a speed of several hundred m/s. UCN are produced when the CN enter the isotopically pure superfluid helium at 0.84 to 0.92 K. The CN induce phonon transitions inside the superfluid helium in order to become UCN, as discussed in Section 1.6.

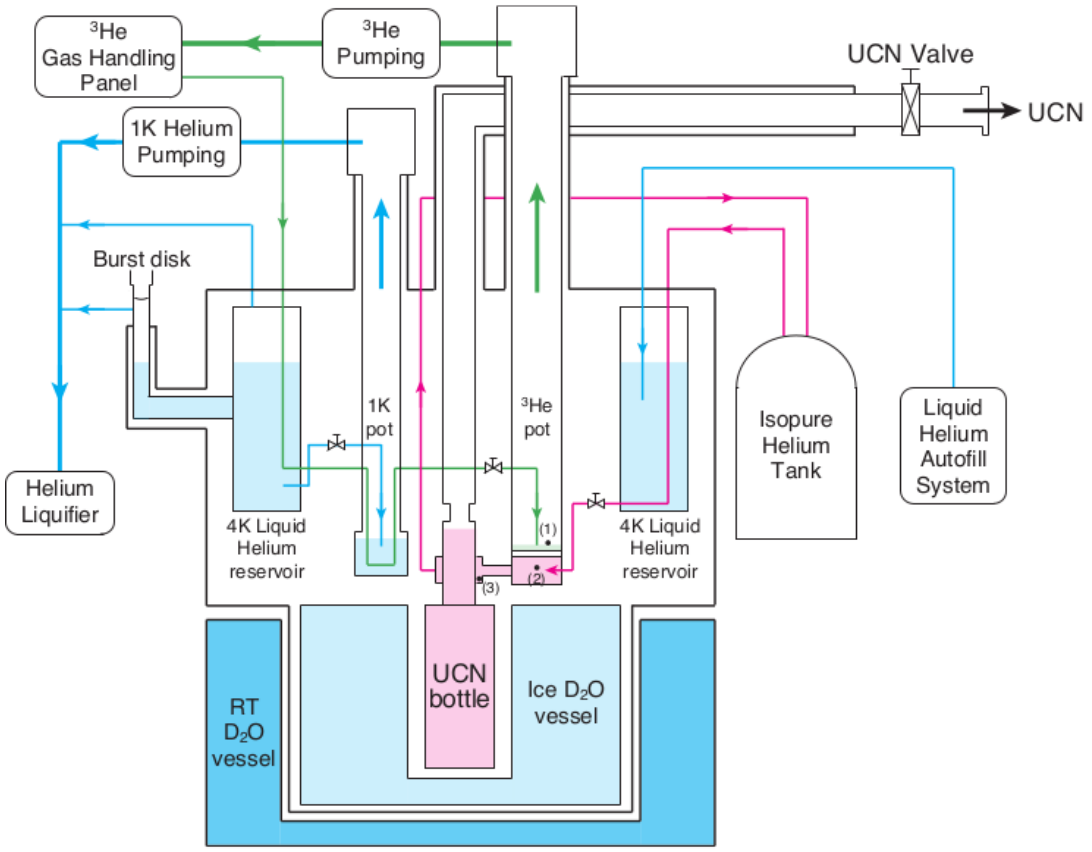

Figure 4.7: Schematic diagram of the vertical UCN source at TRIUMF. Spallation neutrons are moderated in warm D_2O vessel and become cold neutrons in Iced D_2O. The cold neutrons then enter the superfluid helium bottle where they become UCN by phonon excitations in the superfluid. The isotopically pure superfluid helium is cooled down to below 1 K via a ^{3}He pot. The ^{3}He pot is cooled down to 0.7 K via the 1 K pot and further pumping (see text for more details).

A schematic diagram of the vertical source is shown in Fig. 4.7 and a 3D drawing of the vertical source and the guide geometry is shown in Fig. 4.8. The UCN-production volume is filled with superfluid helium and is cooled by a Cu heat exchanger with the ^{3}He pot (see section 4.3.2). The combined height of the UCN-production volume and vertical UCN guide is 1.25 m, with the lower 0.62 m filled with superfluid helium. Right

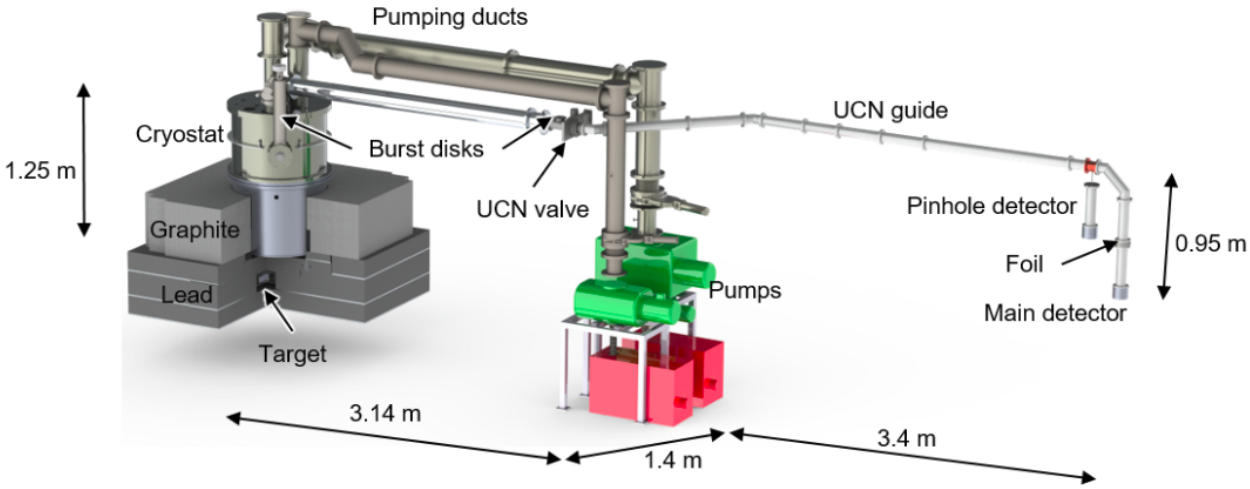

Figure 4.8: The UCN source and the guide geometry at TRIUMF

above the liquid surface, a short, narrow section of the vertical guide blocks superfluid film flow and radiant heat to reduce the heat load. Above the cryostat, the UCN guide turns horizontal in a vacuum jacket to transition from cryogenic to room temperature. It ends with a burst disk for emergency pressure relief and a gate valve (GV) with a protective ring improving UCN transmission in the open state (indicated as UCN valve on Fig. 4.7 and Fig. 4.8).

Downstream of the GV, the UCN guide follows 45° kinks to avoid radiation leaking through a direct line of sight to the experimental area. Finally, it penetrates through 3 m of additional shielding and drops to accelerate the UCN by gravity to penetrate a 0.1 mm-thick aluminum foil and to enter the main detector with high efficiency. The foil separates the helium vapour-filled UCN guide from the detector vacuum to reduce contamination of the source. The main detector is a ^{6}Li detector described in Section 4.5.1. A secondary ^{3}He proportional counter with its own aluminum window is mounted to a 5 mm pinhole in the guide and serves as a monitor detector.

The neutron moderators, the helium circulation system, and the process of cryostat operations are explained below.

4.3.1 Neutron D_2O Moderators

D_2O Solidification

The D_2O ice vessel has a capacity of 100 L. About 14 L of liquid D_2O is injected to the vessel initially. This is followed by adding 11 L of D_2O to the vessel 8 times. After filling up the vessel, Gifford McMahon refrigerators solidify the heavy water and further cool it down to 20 K. The process of freezing the heavy water takes about 6 days and cooling it down to 20 K takes another 7 days.

4.3.2 Helium Circulation and Superfluid Helium Condensation

Helium circulation and superfluid helium condensation normally starts once the temperature of D_2O has reached 10 K. The stages leading to superfluid helium condensation are presented below. The full operation and design details are available in Ref. [156].

Liquid Helium Reservoir

The first step is to fill the 4 K liquid helium reservoir. The full capacity of the reservoir is 50 L. This dewar is referred to as the "stationary dewar".

In the 2017 experimental run, the TUCAN collaboration developed a system to automatically fill the reservoir from a nearby 500 L dewar. The minimum and maximum levels of the helium in the 4 K reservoir were set for the autofill system. The helium autofill system is shown in Fig. 4.9. The helium level is measured by a level meter. The DAQ system and sensor positions are described in section. 4.4 and the gas flow diagram is available in Fig. A.1 of appendix A. In addition, two flow meters were used to observe the gas flow and evaporation of the superfluid in the 4 K reservoir (FM4 and FM5 in Fig. A.1 of Appendix A). The stationary dewar was filled from 350 L transfer dewars which were in turn filled from the Meson Hall liquifier.

Figure 4.10 shows 5 filling cycles of the 4 K reservoir on April 22, 2017 during the first cooling test. Liquid helium transfer starts once the liquid level in the 4 K reservoir reaches 20%. Once the transfer starts, the liquid level starts to decrease with a sharper slope.

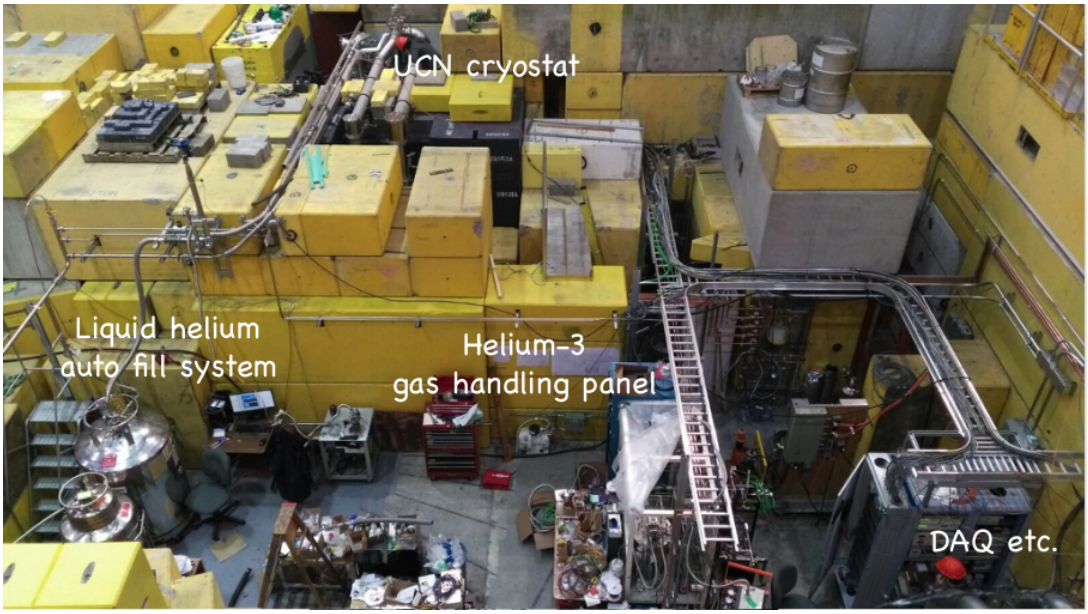

Figure 4.9: A photograph of the UCN experimental area during the mini shutdown in October 2017. Some experimental components are shown and are labelled. The yellow concrete blocks are blocking the radiation during the target irradiation times. The vertical UCN cryostat could be seen because of the removal of some radiation shielding.

This is because it takes some time to cool the transfer line from the stationary dewar to the reservoir. The warmer helium vapour causes a heat load on the 4 K reservoir. Any helium gas evaporated from the reservoir returns through a recovery line to the liquifier. Liquid helium transfer stops once the 4 K reservoir is 60% full.

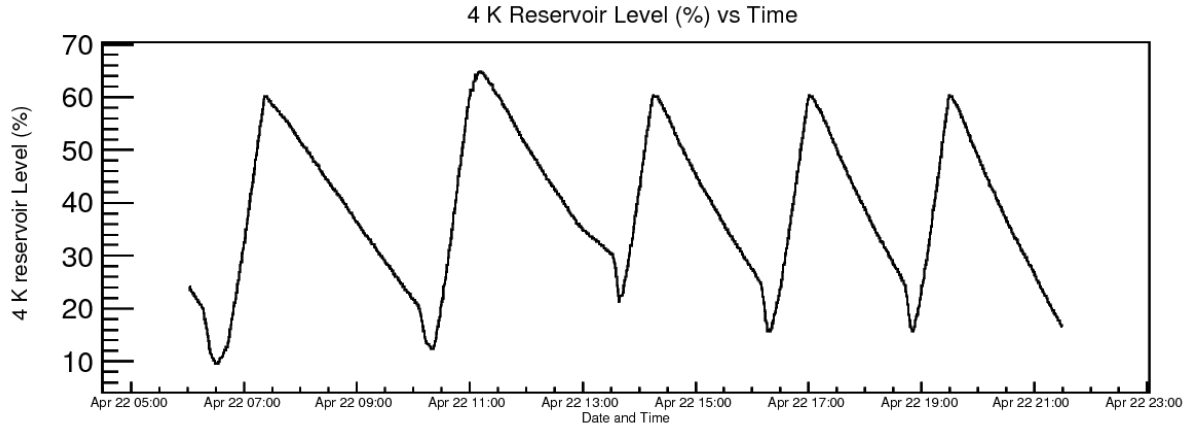

Figure 4.10: The 4 K reservoir filling during the cool down test in April 2017.

The efficiency of each transfer from the stationary dewar to the 4 K reservoir was about 40% to 60% on average.

Liquid Helium Pot at 1 K

The 4.2 K liquid helium in the helium reservoir is transferred to the 1 K pot. The flow rate of the transferred liquid helium is controlled by a needle valve (JT valve) where the Joule-Thomson expansion happens and the liquid helium cools down. The Joule-Thomson expansion occurs when a gas or liquid passes through a valve which has different temperatures and pressures on both sides, while there is no heat exchange to the environment. The 1 K pot is pumped constantly which provides a pressure drop across the valve which then gives rise to expansion, and therefore, cooling of liquid helium down to about 1.4 K via Joule-Thomson (JT) expansion as discussed below. The pressure in the pot determines the saturated vapour pressure above the liquid, and hence, the temperature of the liquid. Calculations of refrigerator performance were studied recently in the context of the vertical UCN source [157] and in the future horizontal UCN source [158]. The level of helium in the 1 K pot is measured by a liquid level meter. The maximum level of the 1.4 K liquid helium is about 15 cm. At this level, the volume of the 1.4 K liquid helium is about 1.3 L.

Liquid ^{3}He Pot

Once the 1 K pot is ready, the ^{3}He gas circulates in a loop from room temperature to the ^{3}He pot. ^{3}He is expensive, so the entire ^{3}He gas system is kept below atmospheric pressure. In case of a leak, the system will be contaminated, but we will not lose ^{3}He. The ^{3}He pot works based on the Joule-Thomson effect as well, as described in the section above. To start, the needle valve in the ^{3}He reservoir is opened. A vacuum pump compresses the ^{3}He gas. The ^{3}He gas is then purified by a room temperature and a cold purifier, and is precooled by the 4 K reservoir, and then condensed in a Cu tube in the 1 K pot. The liquid ^{3}He then undergoes Joule-Thomson (JT) expansion through the NV into the ^{3}He pot which is decompressed by vacuum pumps. The JT expansion is isenthalpic. The ^{3}He pot is connected to the isotopically pure ^{4}He volume by a copper heat exchanger which conducts the heat in the isotopically pure ^{4}He to the ^{3}He pot.

Isopure Helium

After filling the ^{3}He pot with 0.7 K liquid ^{3}He, condensation of the isotopically pure (isopure) superfluid helium starts. The isopure helium has much less ^{3}He than ^{4}He (less than 10^{-10}). Even though the natural abundance of ^{3}He is 1.37×10^{-6} in the atmosphere, this value is still large because of the large neutron absorption cross section of ^{3}He. The existence of ^{3}He causes the UCN storage lifetime to decrease (see section 1.6.1).

The isopure helium is stored in the isopure helium tank shown in Fig. 4.7. Before entering the cryostat, the isopure helium goes through a purifier. The purifier is composed of low temperature charcoals cooled by LN_2. The isopure He is precooled in the 4 K reservoir and goes into the heat exchange pot attached to the bottom of the ^{3}He cryostat. The bottom of the ^{3}He cryostat and the top of the heat exchange pot are connected via a copper heat exchanger. The isopure He in the heat exchange pot is cooled by the 0.7 K liquid ^{3}He via the copper heat exchanger and becomes He-II. The condensed He-II fills the He-II bottle with a volume of 8.5 L and is cooled to $\sim$ 0.83 K.

4.4 Data Acquisition System

The TUCAN UCN DAQ system accumulates data from different devices and integrates them into a MIDAS file. For the 2017 data acquisition, almost all the sensors such as temperature sensors, flow meters, pressure gauges, etc. were connected to a Programmable Logic Controller (PLC). The PLC receives information from the connected sensors or input devices, processes the data, and triggers outputs based on pre-programmed parameters. Depending on the inputs and outputs, a PLC can monitor and record data, automatically start and stop processes, generate alarms based on the applied limits, and more.

A picture of the PLC is shown in Fig. 4.11. It is useful to document a few key features of the layout of this cabinet, which I had an involvement in developing. It is hoped that this will aid future generations of students who will contribute to the EPICS and PLC systems as they evolve. The PLC modules are placed in the top two rows. The bottom

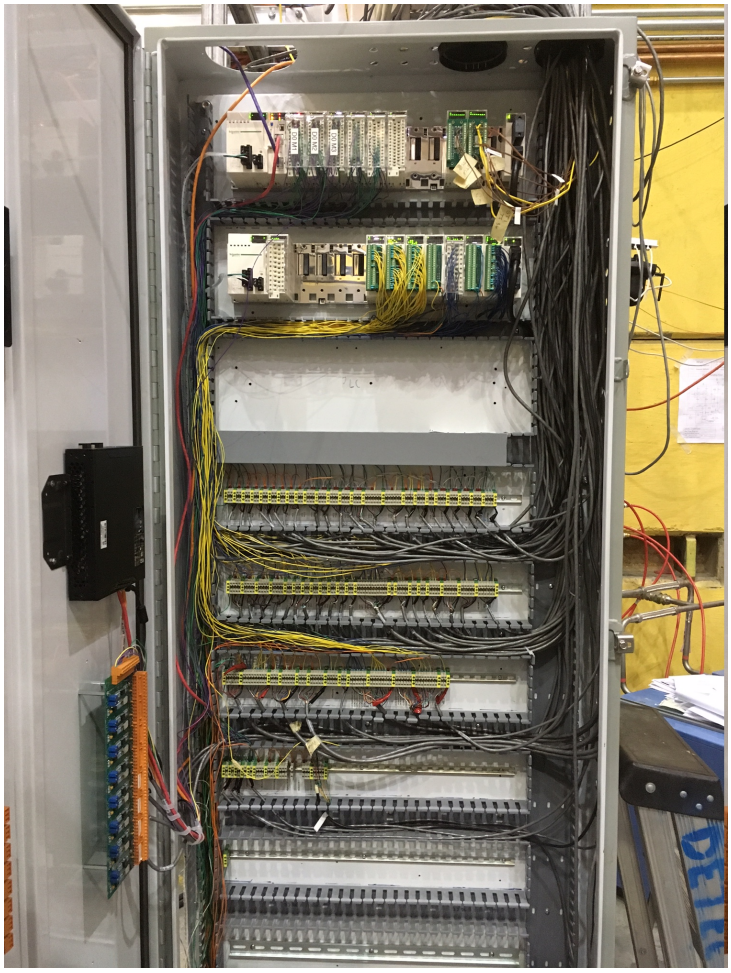

Figure 4.11: A photograph of the PLC in the meson hall. The grey terminal blocks are used to connect the signal from the devices to the computing modules. The first two top rows include the computing modules. Each sensor is connected to a specific terminal on a specific module. The bottom row is where the power supplies and the fuses are positioned.

row includes the power supplies and the fuses for the sensors. The middle section of the PLC box has the terminal blocks for all the sensors. The green terminal blocks are for the ground connection and the grey terminal blocks are for all other readings. The cables from the sensors enter the PLC via the two holes on the top of the PLC box. They are then routed on the right side of the panel and connected to the designated terminal blocks. The input connection from the sensors to the terminal blocks enter from the bottom row and the output connection to the PLC modules leave the terminal blocks from their top row.

Figure 4.12 shows the Altium drawing for the PG3H sensor in the ^{4}He system which is named UCN:He4:PG3H. The first part indicates that it is a sensor for the UCN source,

the middle part indicates which sub-system this system belongs to (e.g., ^{3}He or ^{4}He or UCN guides UGD) and the last part is the name of the sensor which in this case is pressure gauge 3 high (PG3H). The left wires on the left side of the drawing show the connection to the modules. Here we used the red (RD), black (BK) and shield (SH) of a Belden 9462 cable. An orange wire (OR) then goes to the bottom of the PLC and connects to a fuse and a violet wire (VI) connects to the top row (D0) module one (M1) and terminals T7 and T9. The other values (UCN:HE4:PG3H and RADCPRESS) are related to the PLC programming. On the left side of the graph we see wires from the sensor itself to the terminal block. As the figure shows, the sensor is a Omega PXM219-1.6 bar pressure gauge. To see the location of the sensor, see Appendix A.

Figure 4.12: Altium drawing of the pressure gauge PG3H (UCN:HE4:PG3H)

The communication between the PLC and the screen is handled by EPICS. The EPICS screen defines the user interface for the controls. It provides readouts of variables, indications of device status, and various user input controls for turning devices on/off, resetting devices, etc. The screen shows the approximate physical layout of the apparatus being controlled, with each device and its controls placed in its actual location. The colours of the devices are used to indicate their current status [159]. Figure 4.13 shows the thermal EPICS screen for the TUCAN vertical UCN source during the November 2017 experimental run. The gas flow screen (not shown, very similar to the thermal screen) is intended to contain all the information about pressures, flows, levels, and controls for pumps and valves.

MIDAS is a modern data acquisition system developed at PSI and TRIUMF written in C/C++ which runs on all operating systems. MIDAS logs data in two different ways: History logging where some data is saved periodically (every 1-10 s) and can be plotted from history page and file logging where all data is saved to MIDAS file to be analyzed

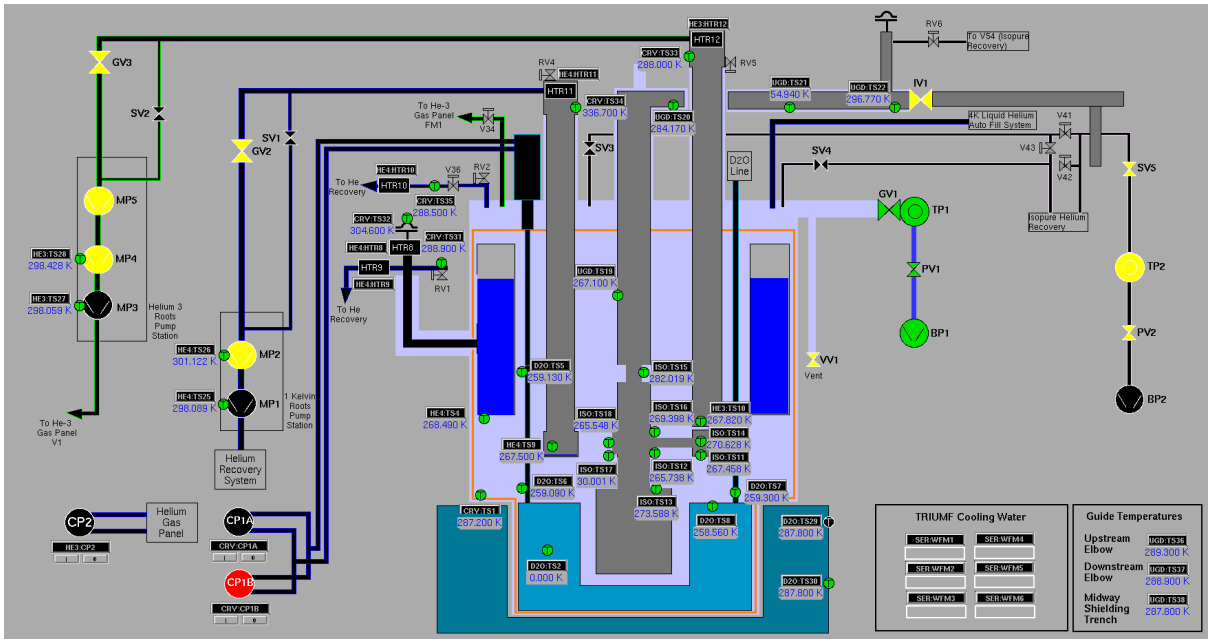

Figure 4.13: EPICS thermal screen. The approximate location of each temperature sensor is shown. The thermal screen is intended to contain all the information about temperatures, and controls for compressors and heaters.

later. The TUCAN MIDAS DAQ has a web interface shown in Fig. 4.14. The green colour indicates that the equipment front-end is running. Each run can be started by pressing the button at the top section.

The main MIDAS front-ends that are being read out by the UCN DAQ:

- Source EPICS front-end (and beam line EPICS) front-end, which copies a subset of the EPICS Process Variables (PVs) to the MIDAS history system. The program that does this is called "feSourceEpics". On the MIDAS status page the equipment "SourceEpics" is green and producing new events at a rate of ~ 0.1 Hz. It is possible to add new history plot or add new variables to the existing history plot.

- A Keithley picoammeter which is reading the current from a thermal neutron counter. The picoammeter is readout through a MIDAS-GPIB chain; the front-end to control it is called "scpico".

- The V1720 for reading out the UCN ^{6}Li detector.

- A front-end program for controlling UCN sequence. It starts triggering after the end of target irradiation.

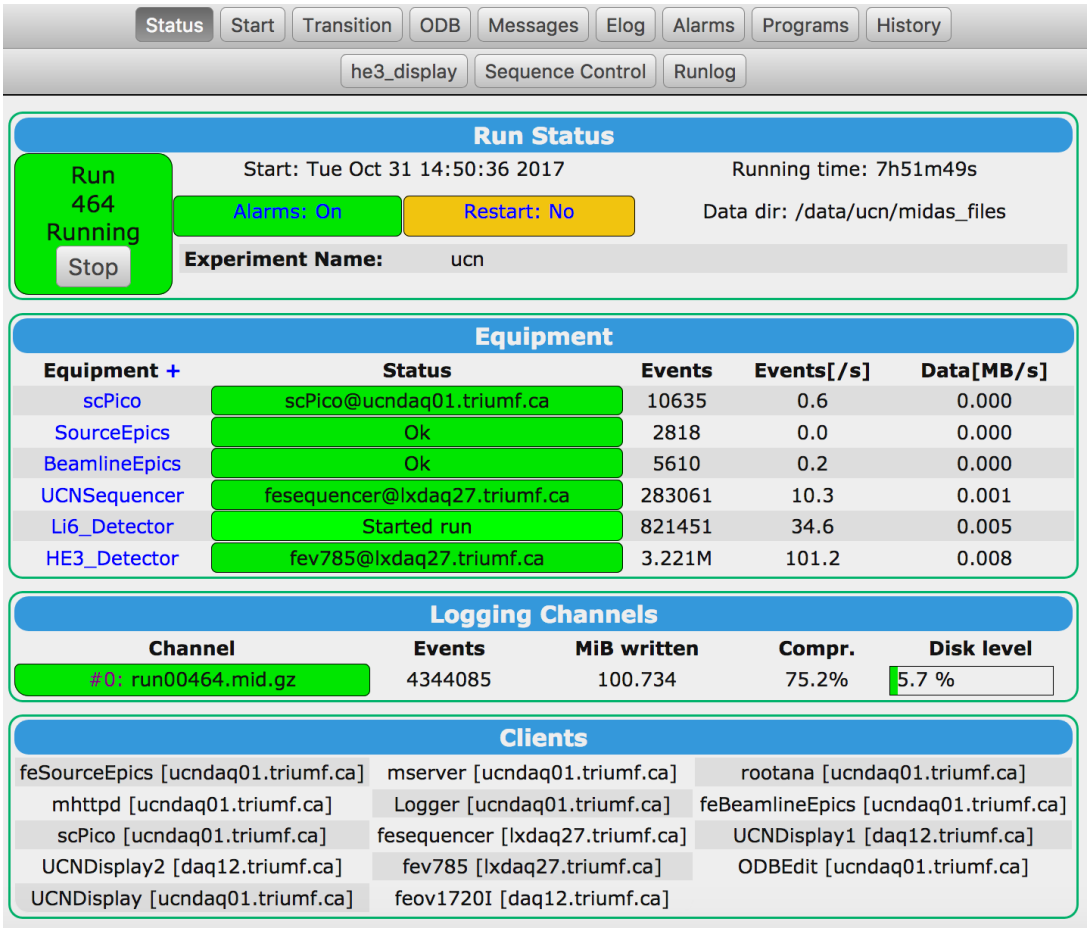

Figure 4.14: TUCAN MIDAS web interface

- V785 peak sensing ADC for reading out the UCN ^{3}He detector. This front-end is for digitizing the signal from the ^{3}He UCN detector. The program for reading out the digitizer is called "fev785". These front-end program controls the readout from a CAEN V785 VME module. The trigger (gate) signal for the V785 is generated by a bunch of NIM electronics that process the signal from the ^{3}He detector.

For the 2017 experimental run, each experiment had a unique MIDAS run number. The MIDAS files were then converted to ROOT files for data analysis. ROOT is a scientific software package developed by scientists at CERN [160]. It provides all the functionalities needed to deal with data processing, statistical analysis, visualization and storage. It is mainly written in C++, but integrated with other languages such as Python and R. Each ROOT file represents a particular Midas run and has 8 trees. A tree in ROOT is like a table. Each row of the table is a branch in the tree. Figure 4.15a shows the trees in a ROOT file. The XXX indicates the number of the MIDAS run. The

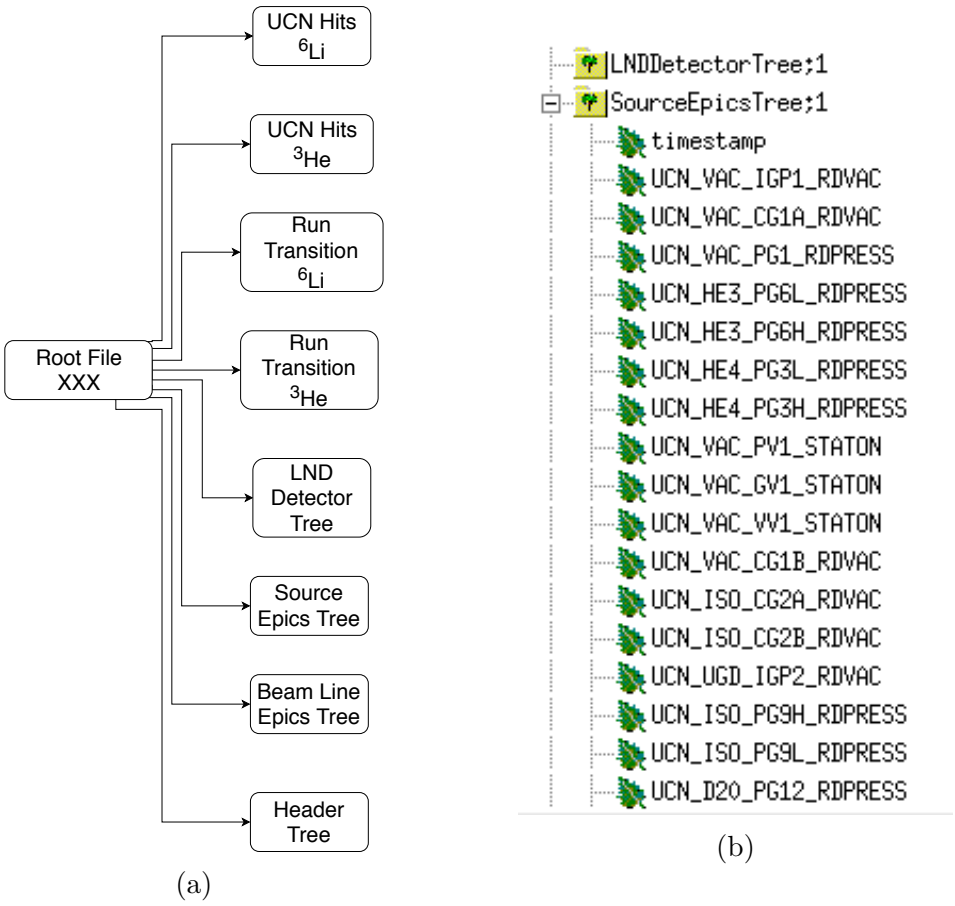

Figure 4.15: (a) A ROOT file and the trees that represent tables. (b) A snapshot of the Source Epics tree with some of the branches. Each branch is a row of the Source Epics table.

UCN Hit trees include the data time-stamps, ChargeL, ChargeS, PSD (see Section 4.5), Baseline and etc. The run transition trees include the UCN valve open time, UCN valve close time, Cycle start time and etc. (see Chapter 5). The LND (thermal neutron) detector tree has the thermal neutron detector readings and its time-stamps. The Source Epics tree has the readings for all the UCN source sensors integrated into the EPICS system, and the Beam Line Epics tree has all the readings related to the beam lines such as target temperatures and etc. The header tree includes the experiment number (e.g., TCN170XX which represents a TUCAN experiment in 2017 and XX represents the experiment number), the person who was on the shift, and the comments they entered on the MIDAS web interface screen during the shift.

We developed a ROOT program that extracts the UCN cycle information for each MIDAS run and creates a .root file. The output file has one tree as “cycle information”

table. It consists of branches with the cycle average, maximum, and minimum values for the main sensors that contribute to the analysis. The analysis is based on the UCN cycles, and it is essential to know, for example, how the temperature of the superfluid helium changes for each cycle. Therefore, the average, maximum and minimum values of the superfluid helium temperature for each cycle for different temperature sensors are calculated and inserted in the cycle information tree. In addition, the UCN background, and the total UCN counts for each cycle are also added to the tree. More details about these variables, and the result of the analysis is presented in Chapter 5.

4.5 UCN Detectors

For the TUCAN experimental runs in 2017, a ^{6}Li and a ^{3}He detector were used. The main reason two detectors were used was to check the consistency of the result, and the performance of each detector. A brief description of each detector is available below.

4.5.1 ^{6}Li Detector

The main detector used during the UCN measurements (see chapter 5) is a ^{6}Li glass based scintillator detector designed and built at the University of Winnipeg for the TUCAN nEDM experiment at TRIUMF [112, 161]. Since ^{6}Li has a high neutron capture cross-section (order of 10^5 b) at UCN energies, the scintillator glass is doped with it. The charged particles in the reaction

$$^6Li + n \rightarrow \alpha(2.05 \text{ MeV}) + t(2.73 \text{ MeV}) \tag{4.1}$$

are detected. The mean range of the α is 5.3 μm, and the mean range of the triton is 34.7 μm. To reduce the effect of α or triton escaping the glass, a layer of 60 μm thick depleted ^{6}Li glass (GS30), on top of a layer of 120 μm thick dopped ^{6}Li (GS20) were optically bonded. This design allows the UCN to pass through the depleted layer before being captured in the ^{6}Li-rich layer, thus the resultant particles deposit all their energy within the scintillating glass. Table 4.1 shows the content and density of those

^{6}Li scintillators.

Scintillator	GS20 (^{6}Li Enriched)	GS30 (^{6}Li depleted)
Total Li content (%)	6.6	6.6
^{6}Li fraction (%)	95	0.01
^{6}Li density (cm^{-3})	1.716×10^{22}	1.806×10^{18}

Table 4.1: Properties of the glass scintillators

Making the scintillating Li glass as thin as possible reduces the sensitivity to γ-ray-induced scintillation backgrounds, and thermal neutron captures. In order to handle high UCN rates of up to 1 MHz, the ^{6}Li detector face is segmented into 9 tiles (see Fig. 4.16). The scintillation light of each tile is guided through ultra-violet transmitting acrylic light-guide to its corresponding photo-multiplier tube (PMT) outside the vacuum region of the detector.

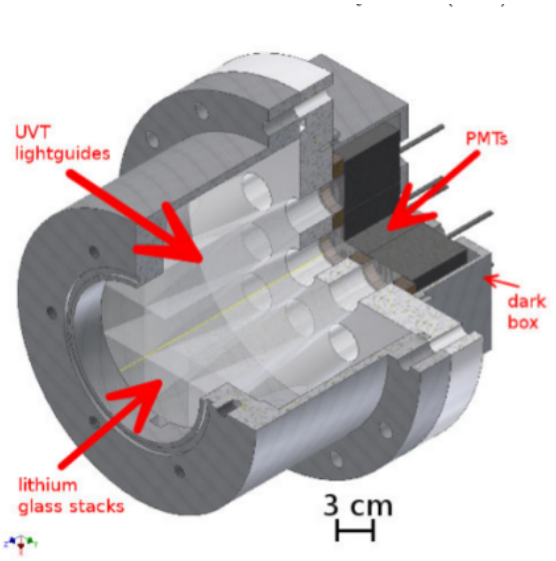

Figure 4.16: 3D drawing of the ^{6}Li detector and its enclosure. The enclosure is made of Al, and the rim of the adapter flange which UCN can hit is coated with 1 μm Ni by thermal evaporation.

The data acquisition for the detector is based on the CAEN V1720 digitizer which has a Pulse-Shape Discrimination (PSD) firmware. Every 4 ns the digitizer samples the waveform on a 2 V scale into an ADC value between 0 and 4096. Each channel of the digitizer sends a trigger, whenever the number of counts in the ADC goes below a certain baseline (pedestal) value. The PSD calculates the sum of the signal below the baseline for two time windows: $t_s = 40$ ns (short gate) and $t_L = 200$ ns (long gate). The short gate is

chosen in a way to contain all of the charge for the γ-ray interactions in the light-guide. The ADC sum for during the long gate below the baseline is called Q_L (read charge long) and for during the short gate below the baseline is called Q_S (read charge short). Charge long has the total charge deposited for the neutron capture events. The PSD value is defined as

$$\text{PSD} = \frac{(Q_L - Q_S)}{Q_L} \ , \tag{4.2}$$

which is the amount of charge in the tail of an event.

The absolute efficiency of this detector is $89.7^{+1.3}_{-1.9}$ % with a background contamination (largely due to γ-ray interactions in the lightguides, also see section 5.2) of 0.3 ± 0.1 % [112]. The detector is stable at the 0.06 % level or better, and that the variation in the efficiency between the detector tiles is less than 5 %.

4.5.2 ^{3}He Detector

The ^{3}He detector used for the data acquisition is a Dunia-10 type which was used at RCNP. ^{3}He provides an effective neutron detector material for neutron detection by absorbing neutrons via the following reaction

$$n + {}^3\text{He} \rightarrow p + t + 674 \text{ keV}. \tag{4.3}$$

Before the start of the experiment, the ^{3}He detector was tested with an AmBe source, and it showed consistent result with what was observed at RCNP. The detector was surrounded with paraffin blocks to moderate the neutrons (see Fig. 4.17).

More detail about the ^{3}He detector can be found in Ref. [156].

Figure 4.17: ^{3}He detector and paraffin blocks for neutron moderation.

Chapter 5

UCN Production, Transport, and Detection

In November of 2017, the first UCN at TRIUMF were produced using the prototype vertical UCN source described in section 4.3. Several experiments were performed with the UCN including UCN yield measurements, UCN storage lifetime measurements and steady-state UCN production. These experiments are essential for a better understanding of the vertical source, and to design the next generation high intensity UCN source. In this chapter those experiments are described and the results presented.

This chapter proceeds as follows:

- general discussion of measurement cycle
- data analysis focusing on experimental measurements of UCN counts and storage lifetime in source
- data are compared to detailed Monte-Carlo description in section 5.5 to extract physical parameters of source and UCN guides

5.1 UCN Cycle of Measurement

Figure 5.1 is a simple schematic of UCN production and detection volumes which shows the UCN propagation between different volumes. Here volume V_1 represents the pro-

duction and storage volume before the valve, where N_1 UCN are produced. V_2 is the secondary volume, where N_2 UCN enter after the valve is opened, and V_3 is the detector volume where N_3 UCN are detected.

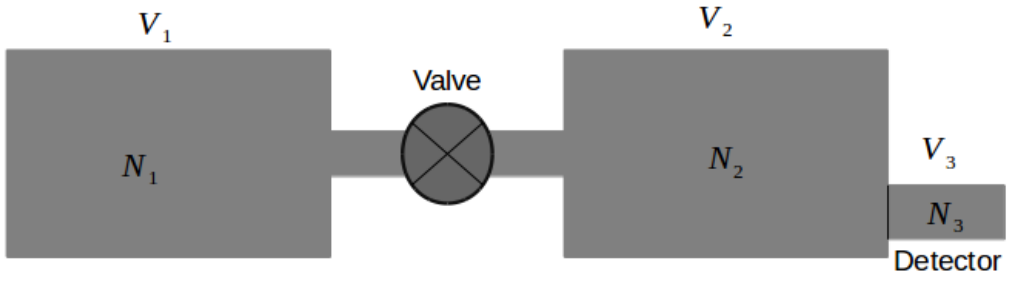

Figure 5.1: Schematic drawing of a simple UCN source. V_1 is the production volume with N_1 number of UCN, V_2 is the secondary volume where N_2 number of UCN exist, and V_3 is the detector with N_3 number of UCN.

At $t = 0$, when the beam is on and the valve is closed, the number of UCN in V_1 builds up, while the total number of UCN in V_2 and V_3 is zero. This may be described with

$$\frac{dN_1}{dt} = P - \frac{N_1}{\tau_1} \ , \tag{5.1}$$

where P is the UCN production rate in the source, as described in Section 1.6.2, and τ_1 is the UCN storage lifetime in the source. The solution is exponential with $N_1 \to P\tau_1$ as $t \to \infty$. After the beam is turned off, the valve is opened, and UCN may travel to the volume V_2 and eventually volume V_3. In our measurements, the valve is usually left open for 2 minutes. The UCN rates of change are described by the coupled, first-order, linear differential equations:

$$\begin{aligned}
\frac{dN_1}{dt} &= -\frac{N_1}{\tau_{c,1}} - \frac{N_1}{\tau_1} + \frac{N_2}{\tau_{c,2}} \\
\frac{dN_2}{dt} &= \frac{N_1}{\tau_{c,1}} - \frac{N_2}{\tau_{c,2}} - \frac{N_2}{\tau_2} - \frac{N_2}{\tau_{c,3}} \\
\frac{dN_3}{dt} &= \frac{N_2}{\tau_{c,3}} \ .
\end{aligned} \tag{5.2}$$

Here $\tau_{c,1}$, $\tau_{c,2}$, and $\tau_{c,3}$ are the lifetimes due to crossing the surface (described below) and τ_2 is the lifetime in V_2. In these equations, dN_1/dt shows the change in the UCN counts over time in V_1, dN_2/dt shows the change in the UCN counts in V_2, and dN_3/dt shows the change in the UCN count in V_3, after the valve is opened. Each term on the right side of the equations is described below.

In the first equation, the total number of UCN in V_1 depends on three factors: the UCN that get into V_2 with the rate $N_1/\tau_{c,1}$, the UCN that are lost with the storage lifetime τ_1 with the rate rate N_1/τ_1, and the UCN that bounce back from V_2 to V_1 with the rate $N_2/\tau_{c,2}$. Here $1/\tau_{c,1}$ is the loss rate for UCN crossing from volume V_1 to volume V_2, and $1/\tau_{c,2}$ is the loss rate for UCN cross from volume V_2 back to volume V_1.

In the second equation for V_2, some UCN cross from V_1 to V_2 with the rate $N_1/\tau_{c,1}$, some get lost with the rate N_2/τ_2, some cross the gate valve and go back to V_1 with the rate$N_2/\tau_{c,2}$, and some get to the detector with the rate $N_2/\tau_{c,3}$. Here $1/\tau_{c,3}$ is the loss rate for UCN crossing from volume V_2 to volume V_3 and $1/\tau_2$ is the loss loss rate for UCN in volume V_2.

In the third equation, the rate of the UCN detection dN_3/dt is the rate of UCN crossing from volume V_2 to volume V_3 as $N_2/\tau_{c,3}$. If they enter V_3, they will be detected, hence, they will not cross back. In principle, solving these equations could give an estimate of the number of UCN in each volume. The solutions are again exponential.

A 3D drawing of the experimental setup is shown in Fig. 4.8. In this case, V_1 is the UCN source bottle and the horizontal section of the UCN guide before the UCN gate valve, and V_2 and V_3 are the volumes after the UCN valve and the detector volume respectively.

The process of UCN production described above is referred to as "batch mode", since the UCN are accumulated in the source before opening the UCN valve. In our standard UCN production measurements, the applied beam current was 1 μA, and the target was irradiated for 60 s. One cycle of measurement is shown in Fig. 5.2. The UCN valve was typically left open for 2 minutes. The end of a UCN cycle is defined by the UCN valve close time. Once the UCN valve is closed, a new cycle of measurement starts. The UCN

counts are then fitted by an exponential function.

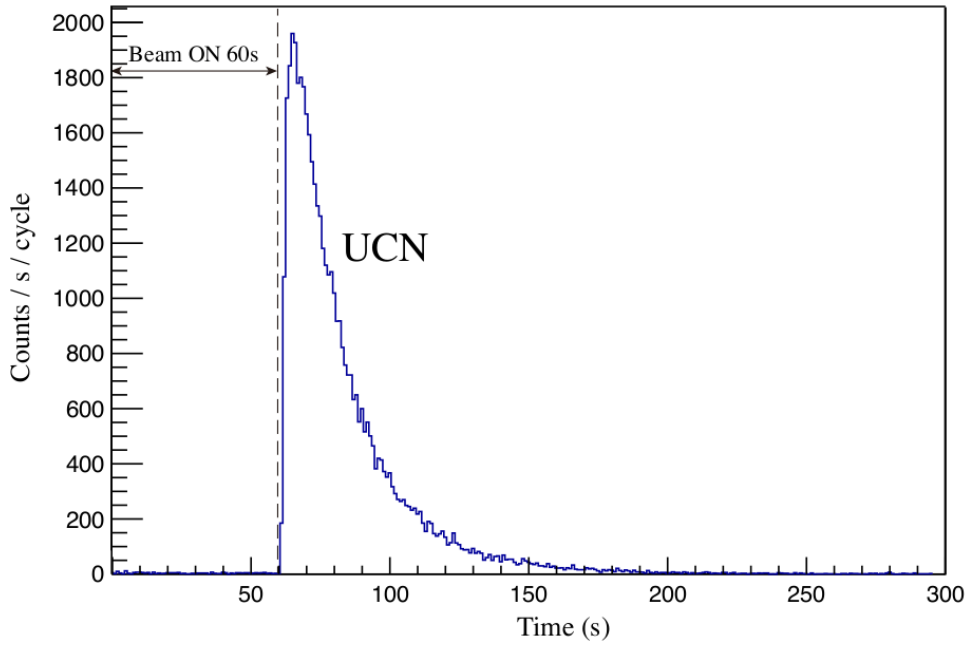

Figure 5.2: The figure shows the UCN rate at 60 s irradiation time, and 1 μA beam current. In this case, the UCN gate valve is opened immediately after the end of target irradiation. At this time, the UCN rate reaches the peak of about 2000 UCN/s. The UCN rate decays down to the background level. The valve is left open for 120 s.

Another possible mode of operation is to leave the UCN valve open while irradiating the target. This is called the "steady-state mode" where we have a constant stream of UCN to the main detector (see Section 5.3.4).

5.2 Data Quality Checks

During the 2017 experimental run, we performed about 35 experiments individually labelled by TCN#. For most of these experiments we used the ^{6}Li detector described in Section 4.5.1. The data in this chapter was focused on UCN source characterization, all acquired with the ^{6}Li detector. To check the reliability of this data we performed data quality checks based on the detector signals.

The PSD versus Q_L distribution from a run is shown in Fig. 5.3 for all nine PMTs combined. The UCN appear in the upper right portion of PSD-Q_L space.

Here the UCN spectrum has an energy range of 3000 to 12000 Q_L as expected, and a median PSD value of 0.5. The events at PSD $\sim$ 0 represent the γ-rays in the lightguides.

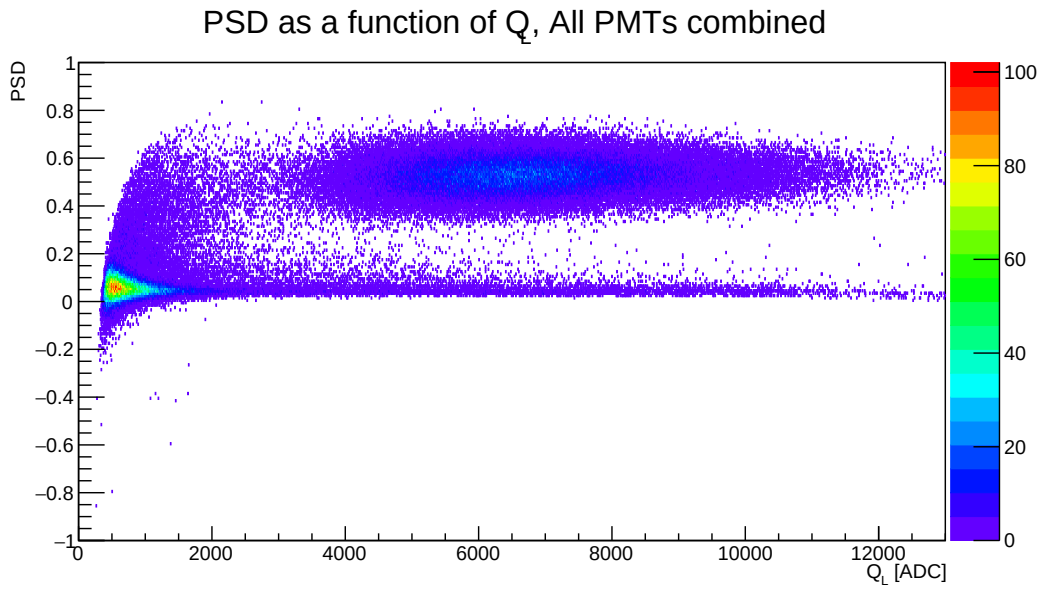

Figure 5.3: UCN event spectra for all of the PMTs for a standard 1 μA proton beam current and 60 s target irradiation time

To define UCN counts, a PSD cut at 0.3 and a Q_L cut at 2000 were applied. These cuts define the UCN box acceptance or UCN region of interest (ROI) described below. Those cuts were confirmed with Monte-Carlo simulations to have an efficiency of 99% or higher. The total number of UCN events in each PMT for a run at 1 μA beam current and 60 s irradiation time is shown in Fig. 5.4. Out of all 9 channels, the central channel counts the most UCN, while the corner channels receive the least as expected based on geometry.

The effect of detector systematics on the measured UCN counts can be categorized in three groups: deadtime, crosstalk and pileup. Deadtime is the minimum time difference between two subsequent UCN events in the same PMT, which gives rise to a loss of UCN counts. Crosstalk arises from multiple trigger events in neighbouring PMTs originated from the same UCN event. This would falsely increase the total UCN counts. Pileup is the combination of multiple events into a single event. It includes UCN-UCN, UCN-γ, γ-UCN and γ-γ pileups. The true number of UCN counts is estimated by

$$N_{\mathrm{UCN}}^{\mathrm{True}} = [N_{\mathrm{UCN}}^{\mathrm{raw}} \cdot (1 + \alpha_{pl} + \alpha_{ct})] \cdot A_{ROI} \ , \tag{5.3}$$

where α_{pl} is the estimated pileup coefficient from data and independent calculations assuming Poisson statistics, α_{ct} is the estimated time-coincidence analysis on data, and

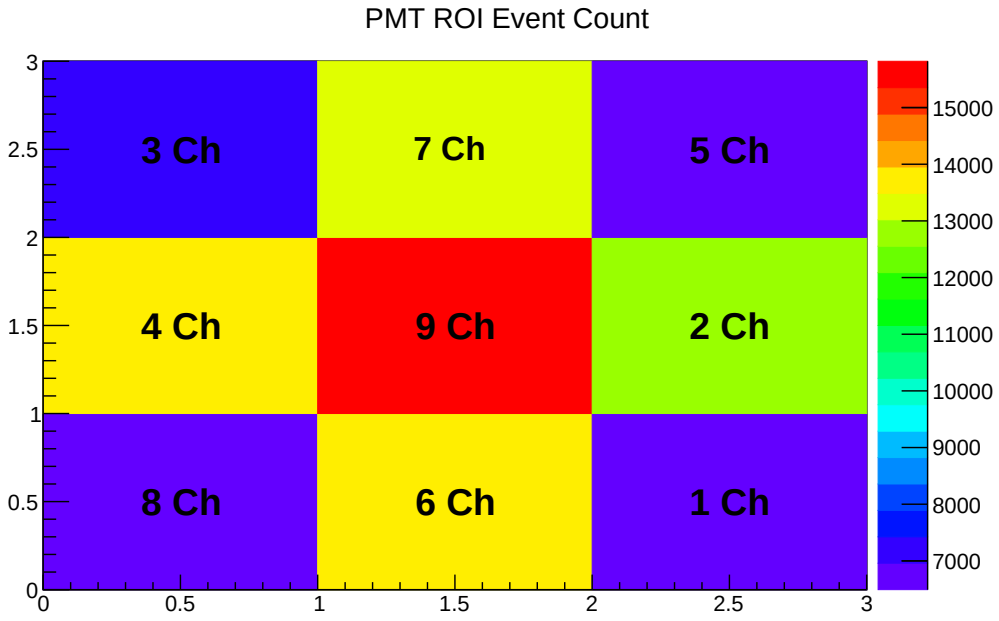

Figure 5.4: Number of UCN events for each channel. The total number of UCN events decrease as we move towards the corner channels.

A_{ROI} is the UCN ROI efficiency estimated using Monte-Carlo simulations. Based on our Monte-Carlo simulations, the γ-UCN and UCN-γ pileups are negligible. In addition, γ-γ pileup does not have a tail which extends into the region defined by the UCN acceptance cuts.

The result of such analyses showed the UCN ROI acceptance is at 99.7 $\pm$ 0.1 %. The UCN-UCN pileup at 1 μA beam current and 60 s irradiation of the target was measured to be 0.075 Hz or less than 1%. The analysis indicated that cross-talk has a negligible effect on the operating rates and deadtime affects the rates by less than 2%. For more detail about the characterization of our lithium detector, see Ref. [112].

5.3 UCN Count Measurements

The total number of UCN produced in the vertical source, N, at a certain time t_i when the UCN valve is closed is the solution of Eqn. 5.1

$$N = P\tau_1 \left[1 - \exp\left(\frac{-t_i}{\tau_1}\right)\right] \ , \tag{5.4}$$

where the UCN storage lifetime τ_1 is given by

$$\frac{1}{\tau_1} = \frac{f_1}{\tau_{\mathrm{He}}} + \frac{1-f_1}{\tau_{\mathrm{vapour}}} + \frac{1}{\tau_{\mathrm{wall},1}} + \frac{1}{\tau_\beta} \ . \tag{5.5}$$

The storage lifetime consists of four terms: the loss rate in the superfluid helium $f_1\tau_{\mathrm{He}}^{-1}$, the loss rate in the helium vapour $(1-f_1)\tau_{\mathrm{vapour}}^{-1}$, the loss rate in the UCN guide walls $\tau_{\mathrm{wall},1}^{-1}$, and the neutron β decay rate τ_β^{-1}. The volume in which the UCN are produced includes the UCN bottle, as well as the horizontal guide section before the UCN valve (see Fig. 4.8). This volume is not fully filled with the superfluid helium. The quantity f_1 is the probability of UCN being in the superfluid helium while the UCN valve is closed. After the valve is opened, the total UCN lifetime is

$$\frac{1}{\tau_2} = \frac{f_2}{\tau_{\mathrm{He}}} + \frac{1-f_2}{\tau_{\mathrm{vapour}}} + \frac{1}{\tau_{\mathrm{wall},2}} + \frac{1}{\tau_d} + \frac{1}{\tau_\beta} \ , \tag{5.6}$$

where f_2 is the probability of UCN being in the superfluid helium, ${\tau_{\mathrm{wall},2}}^{-1}$ is the UCN guide loss rate in the case where the valve is open and the target irradiation is stopped, and τ_d^{-1} is the loss rate in the detector. Figure 5.5 shows three measurement cycles at 1 μA beam current, and 60 s irradiation time with zero second delay time between the end of the target irradiation and opening the UCN valve (this is referred to as the cycle delay time or valve open delay time). The dashed lines indicate the start of the target irradiation for a cycle, the dotted lines show the end of the target irradiation, which in this case is the same as the UCN valve open time. The solid lines shows the valve close time.

The total UCN counts are given by the sum of all the UCN events for the duration of the valve open time. However, this method of counting includes backgrounds. To subtract the background counts from the actual UCN counts, the UCN background rate is calculated before the start of the irradiation of that particular cycle. This rate is then multiplied by the valve open duration, which then gives an estimate of the total background UCN counts. The background rate is typically less than 5 UCN/s. The subtraction of the latter from the total UCN counts gives the actual number of UCN

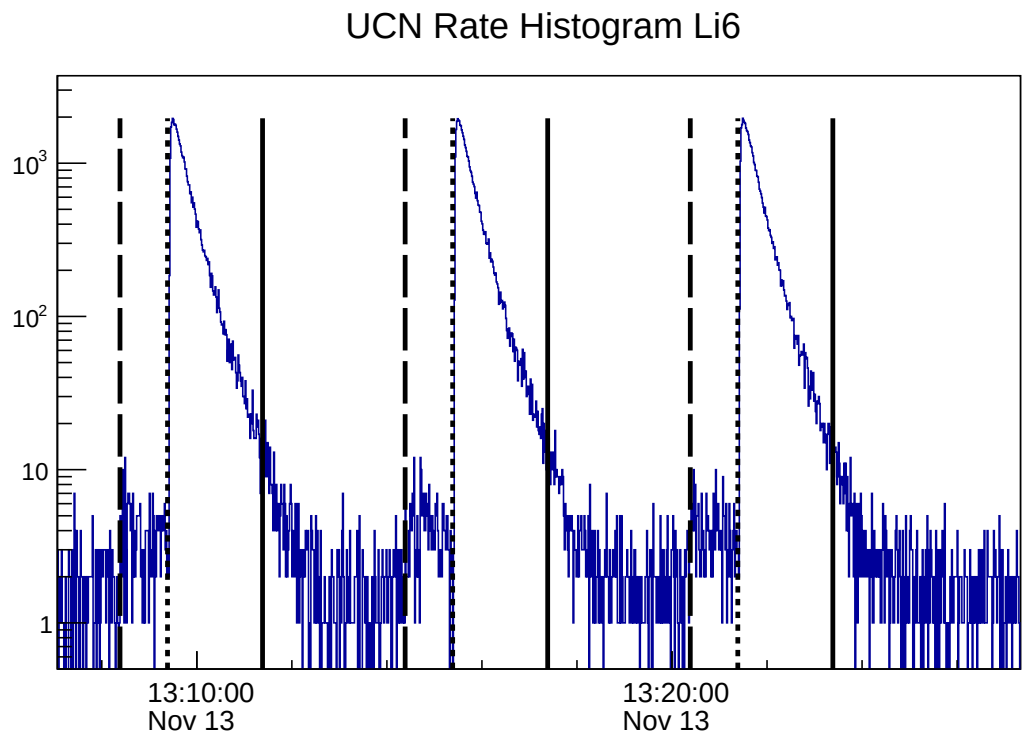

Figure 5.5: Three measurement cycles for 1 μA beam current, 60 s irradiation time, and 0 s valve open delay time. The dashed lines show the start of the target irradiation, the dotted lines show the end of the irradiation and the valve open time for each cycle and the solid lines show the end of a cycle, which is the valve close time.

that are produced by the isopure helium converter and detected by the detector. At the observed UCN count rates, the statistical uncertainty follows Poisson statistics [162].

5.3.1 UCN Yield Versus Proton Beam Current

A unique feature of the TRIUMF facility compared to RCNP is the higher current capability (RCNP: 400 MeV at < 1 μA). Figure 5.6 shows the background-subtracted UCN counts versus the applied proton beam current in A at 60 s irradiation time. At lower beam currents, the total UCN counts increase linearly with the proton beam current. The dashed line shows the extrapolation to higher beam currents in the ideal case. However, at higher beam currents, the total UCN count decreases due to an increase in the heat load on the isopure superfluid helium, and therefore, its temperature. Theoretically, the upscattering rate in the superfluid helium is related to its temperature as T^7 (see Section 1.6.2). This has been confirmed by performing PENTrack simulations and comparing the result to the acquired data (see Section 5.5).

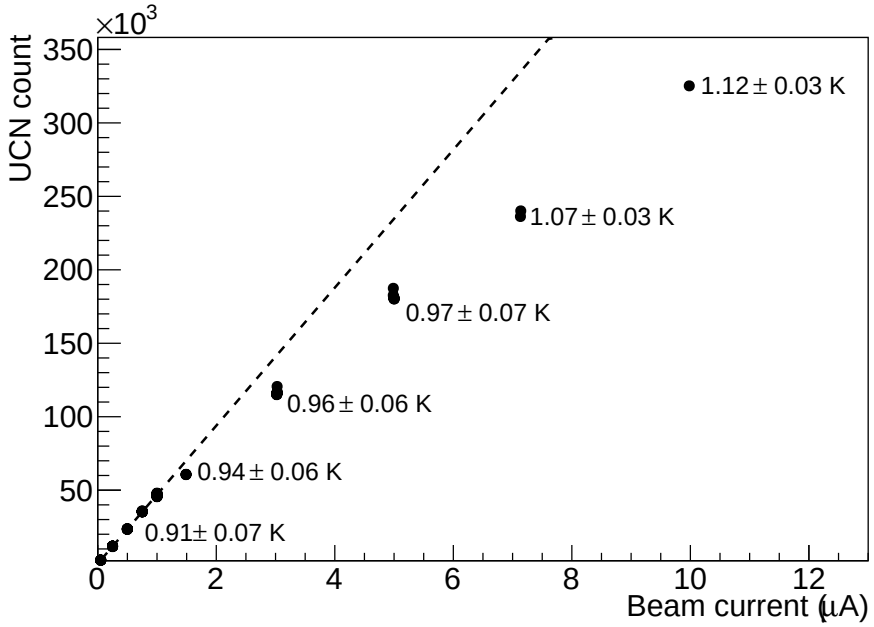

Figure 5.6: The total UCN counts versus the applied proton beam current for 60 s target irradiation times. The labels show the full range of the superfluid helium temperature for that measurement. The dashed line is the fit to the UCN counts at low beam currents. The total UCN counts can be described by Eqn. 5.4. Here the production rate grows linearly with current and τ_1 varies with time.

The labels in the graph show the full range of the isopure helium temperatures during the measurement cycle. Four temperature sensors were used to measure the superfluid helium temperature: TS11, TS12, TS14 and TS16. The location of these sensors is shown in Fig. 5.7. TS11 is located at the UCN heat exchanger bottom, TS14 is located at the UCN heat exchanger top, TS12 is located at the UCN double tube bottom, and TS16 is located at the UCN double tube top. At low temperatures around 0.8 K, these temperature sensors show a maximum of 0.1 K discrepancy with TS16 showing the highest value, and TS12 showing the lowest value.

At lower beam currents, because of the low heat load on the superfliud helium, the temperature change is not significant, and it gives rise to a linear increase in the UCN counts versus at various applied proton beam current. However, at higher proton beam currents, the temperature of the superfluid increases due to a higher heat load, and it gives rise to higher upscattering rate in the superfluid and lower UCN counts.

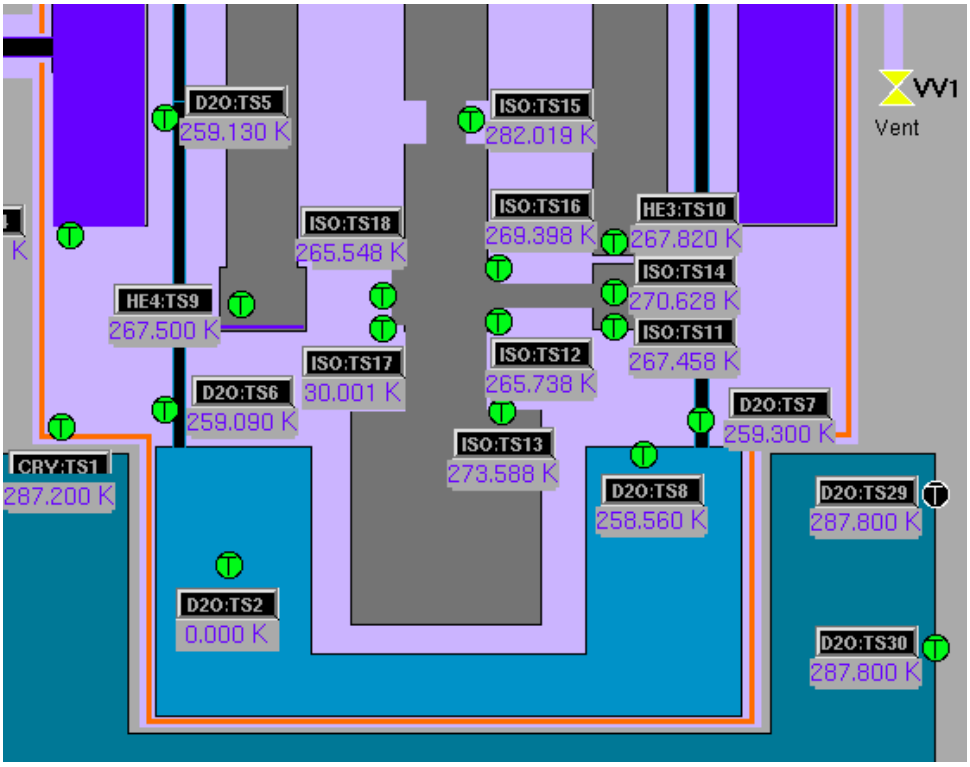

Figure 5.7: Zoomed in screen-shot of the EPICS temperature monitoring screen 4.13. TS11 is located at the UCN heat exchanger bottom, TS12 is located at the UCN double tube bottom, TS14 is located at the heat exchanger double tube top and TS16 is located at the UCN double tube top. For further information about the source schematic see Section 4.3

5.3.2 UCN Yield Versus Target Irradiation Times

The total UCN count is optimized by irradiating the target with different proton beam currents for different irradiation times. The result is shown in Fig. 5.8. In this graph, the vertical axis shows the background-subtracted number of UCN, and the horizontal axis shows the target irradiation time in seconds. Each marker represents a proton beam current. The dashed line is an exponential fit (see Eqn. 5.4) to those data points. The proton beam current and the extracted time constant from the fit are shown in the figure.

At higher beam currents, the saturation time constant decreases due to the higher heat load and faster temperature increase in the superfluid helium. At higher beam currents and longer irradiation times, the total measured UCN counts are below the exponential extrapolation due to the higher temperature and higher upscattering rate in the superfluid helium.

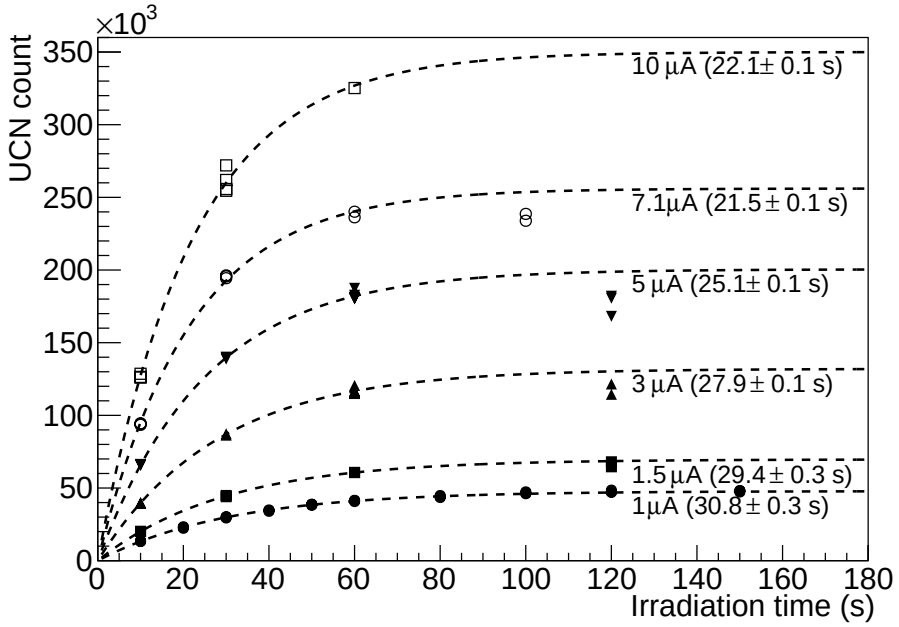

Figure 5.8: Number of UCN extracted from the source after irradiating the target for different times with different beam currents. The dashed lines extrapolate the data for irradiation times below 60 s using exponential saturation curves. The labels show the saturation time constant for each beam current.

5.3.3 UCN Yield Versus Isopure Helium Temperature

The UCN count was also measured at different superfluid helium temperatures (see Fig. 5.9). The vertical axis shows the number of UCN counts, and the horizontal axis shows the temperature of the superfluid helium for all four temperature sensors. The vertical error bars are statistical, and the horizontal error bars are calculated as $(T_{\max} - T_{\min})/2$ for each temperature sensor, where $T_{\max}$ is the maximum value of the superfluid helium temperature reading by one temperature sensor, and $T_{\min}$ is the minimum value read for the same sensor.

As the temperature of the superfluid helium increases, the number of UCN counts in the detector decreases as expected. This is mainly due to the high UCN upscattering rate in the superfluid helium at higher temperatures which is further quantified in Section 5.5.2.

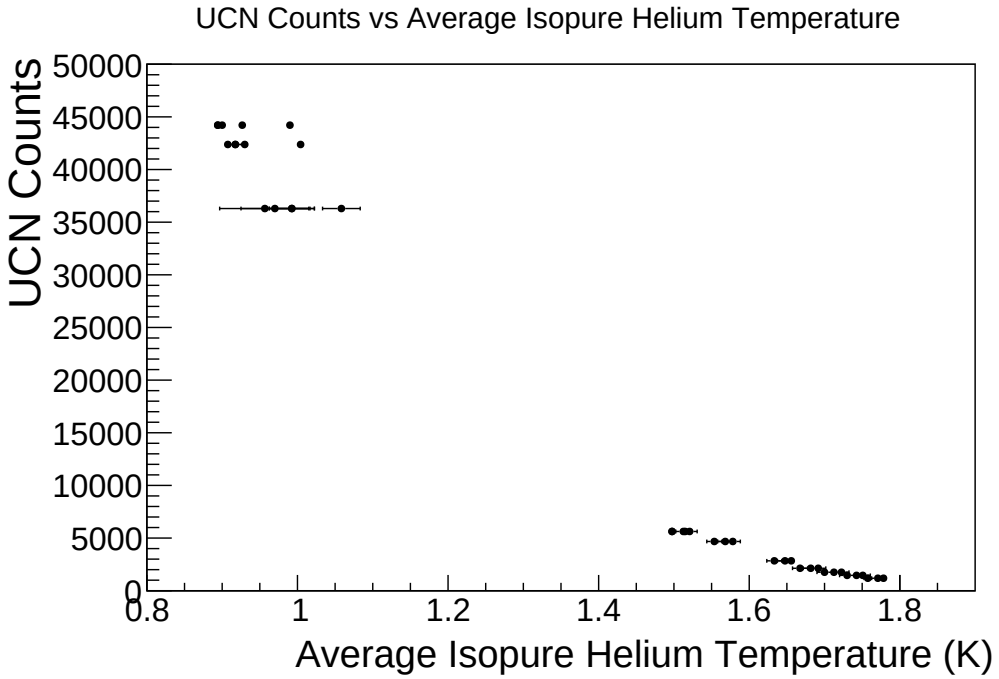

Figure 5.9: UCN yield versus the superfluid helium temperature. At a particular UCN counts, there are several values for the temperature of the superfluid helium. This is due to the discrepancy in the temperature sensor readings as described in the text.

5.3.4 Steady-state UCN Production

The results shown so far were measured in the batch mode operation. In addition to such measurements, the UCN rate was also measured at different beam currents in the steady-state mode of operation. In these measurements, the UCN valve was left open, and the target was irradiated for about 10 min. A typical UCN rate graph for 0.3 μA beam current and 10 min target irradiation time is shown in Fig. 5.10.

At lower beam currents such as 0.3 μA, the UCN rate remains constant throughout the whole target irradiation time as shown in Fig. 5.10. An example of a steady-state UCN production at 3 μA is shown in Fig. 5.11. Since the proton beam current is high, the UCN rate does not remain constant. Here the maximum UCN rate is observed near the start of the target irradiation. As the target irradiation continues, the heat load on the cryostat increases the temperature, and the upscattering rate in the superfluid helium. As a result, the UCN rate decreases. The change in the temperature is shown in Fig. 5.12. Throughout the target irradiation time, the temperature of the superfluid helium increased. Once the irradiation stoped, the temperature started to decrease.

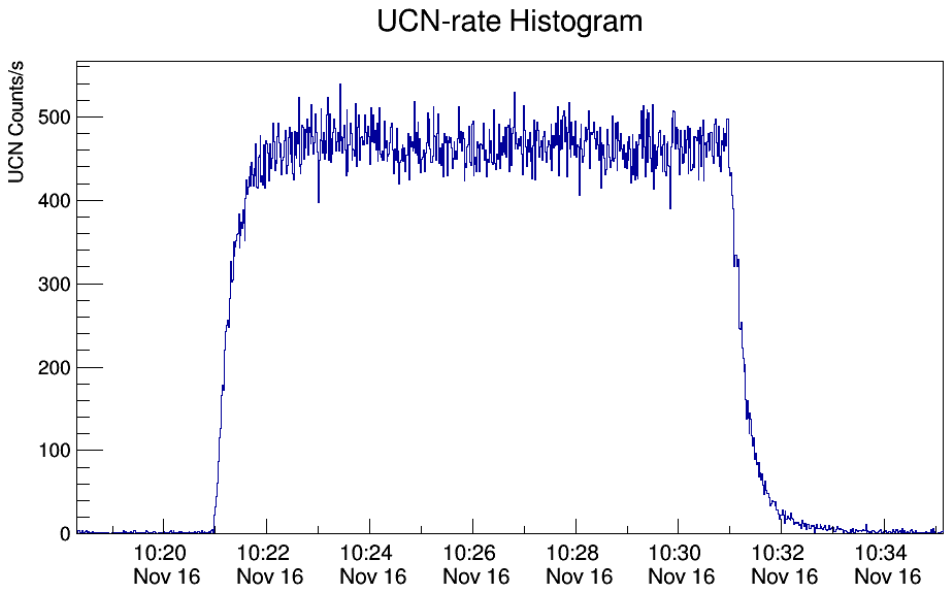

Figure 5.10: UCN rate at the steady-state production mode with 0.3 μA proton beam current. The UCN rate reaches a constant value of 450 UCN counts/s.

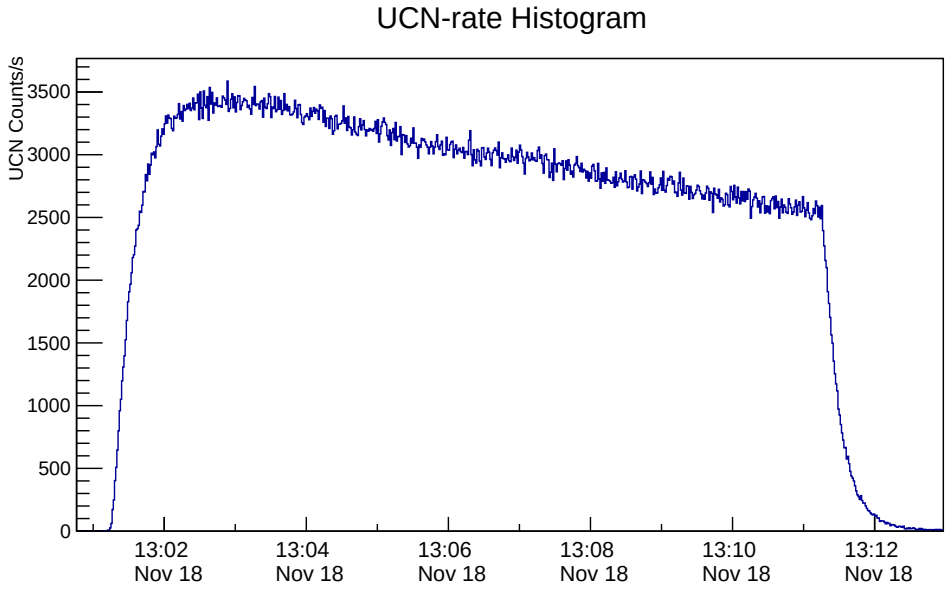

Figure 5.11: The UCN rate at 3 μA beam current at 10 min irradiation time at the steady-state mode of operation. The UCN valve is left open throughout the measurement cycle. Quickly after the start of the target irradiation the UCN rate in the detector goes up. The target irradiation creates a heat load on the cryostat and the superfluid helium. This gives rise to a slow temperature increase in the source. As a result, the UCN rate goes down due to the higher upscattering rate.

The steady-state UCN rate measurements were conducted at different proton beam currents, leading to different temperature changes for all temperature sensors. The result of all those measurements and comparison to simulations is discussed in Section 5.5.

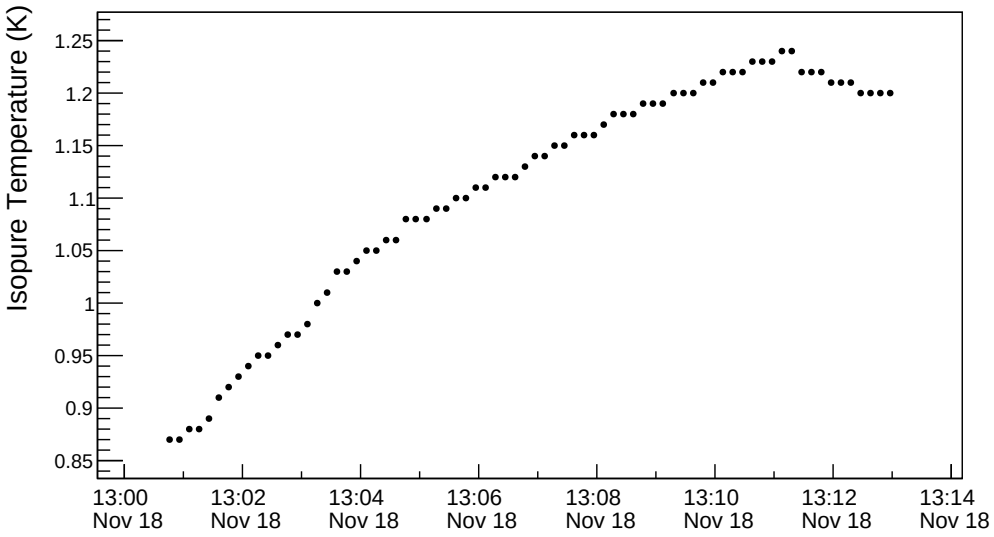

Figure 5.12: The temperature of the superfluid helium (TS12) for the steady state mode of operation at 3 μA beam current and 10 min target irradiation. After the irradiation stops, the temperature starts to decrease.

5.3.5 UCN Yield Over the Experiment Period

The total UCN counts for our standard measurements at 1 μA beam current and 60 s irradiation time over the course of the experimental run is shown in Fig. 5.13. The graph shows an overall decrease of about $\sim 40\%$ over the course of the eighteen days. The source volume is connected to a long UCN guide sealed with an O-ring. It is expected that residual gas added contaminants to the source every time the UCN valve opened. This caused a decrease in the UCN yield (and storage lifetime as shown later in Section 5.4.3) over the course of the measurement. In addition, the changes in the UCN guide geometry in the latter half of the run potentially affected this drop by adding contamination to the source and increasing the losses.

5.4 UCN Storage Lifetime

The total number of detected UCN strongly depends on the storage lifetime of the source τ_1 (see Eqn. 5.5), which indicates the performance of the UCN source.

The storage lifetime of UCN is determined by making an exponential fit to the background-subtracted UCN counts at different valve open delay times right after the

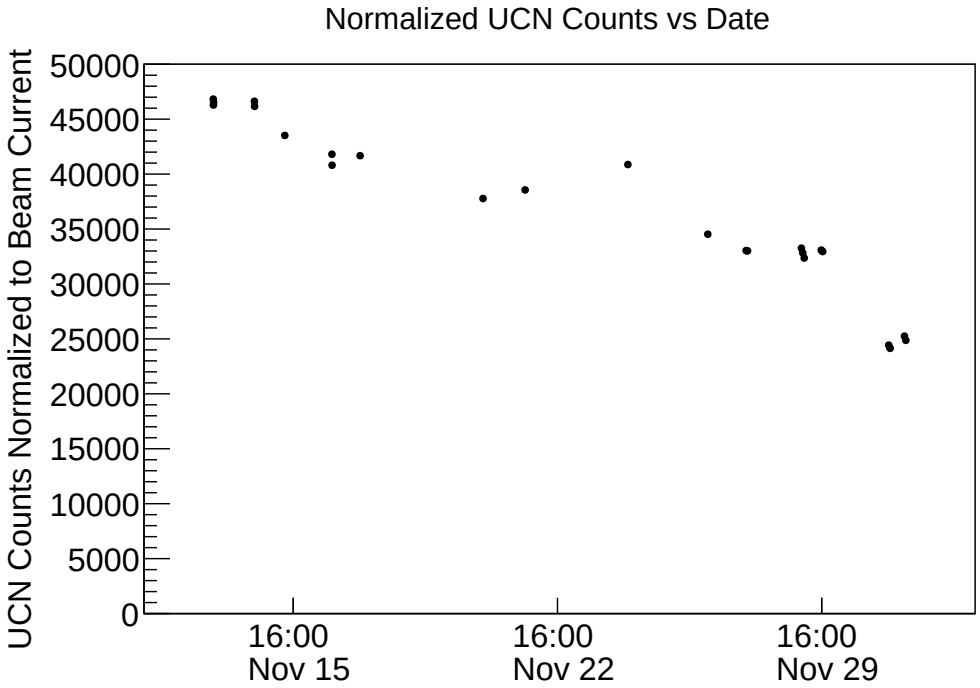

Figure 5.13: The total UCN counts extracted from the source for 1 μA beam current and 60 s irradiation time at different days during the experimental run.

irradiation stops. Typically the target was irradiated for 60 s and valve open delay times were 0 s, 5 s, 10 s, 20 s, 30 s, 60 s, 80 s, 120 s and 170 s.

Fig. 5.14 shows several UCN cycles for the standard 1 μA proton beam current and 60 s target irradiation time. The difference in the maximum detected UCN rate is due to different valve open delay times as labelled on the graph. Fig. 5.15 shows the total UCN counts (background subtracted) versus the valve open delay time for 1 μA and 10 μA proton beam current and 60 s target irradiation time. The total UCN count at 0 s cycle delay time is higher for 10 μA. The longer delay times give rise to lower UCN counts due to the loss mechanisms. The one exponential fit function

$$\text{UCN counts} = Ae^{-t/\tau_1} \ , \tag{5.7}$$

determines the storage lifetime τ_1. At the 170 s valve open delay time, the background-subtracted UCN counts are inconsistent with the exponential fit function due to low statistics. However, the result of the fit is not driven by this inconsistency as it has a negligible effect on the extracted storage lifetime because of low statistics.

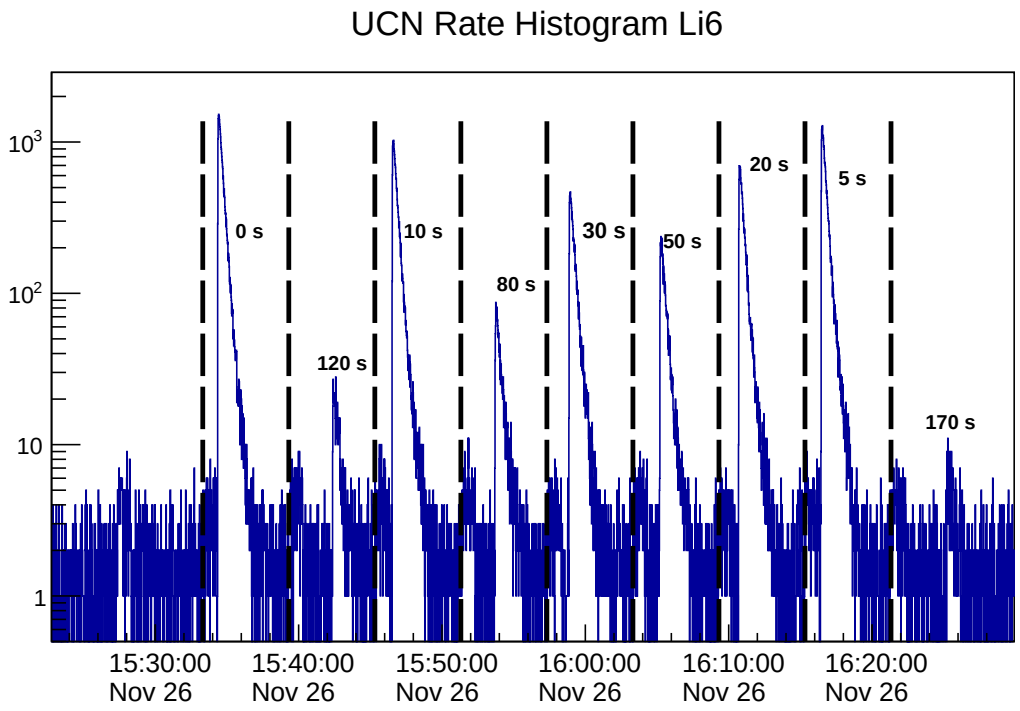

Figure 5.14: UCN cycles at different valve open delay times for 1 μA beam current and 60 s target irradiation time. The vertical dashed line indicate the start of the target irradiation. The values in seconds represent the valve open delay times for each cycle.

5.4.1 Storage Lifetime Versus Beam Current and Irradiation Time

The storage lifetime of UCN in the source was measured at different proton beam currents and different target irradiation times for a better understanding of the source. The result of those measurements is shown in Fig. 5.16. Here the vertical axis shows the storage lifetime of the source in seconds, and the horizontal axis shows the proton beam current in μA. Each marker represents a target irradiation time. At lower beam currents, the duration of the target irradiation does not make a significant difference in the storage lifetime. At higher proton beam currents, the longer the irradiation time, the lower the storage lifetime will be. In summary, irradiating the target at high proton beam currents and longer irradiation times create a higher heat load on the UCN source, which leads to higher upscattering rates, and as a result, lower UCN storage lifetime in the source.

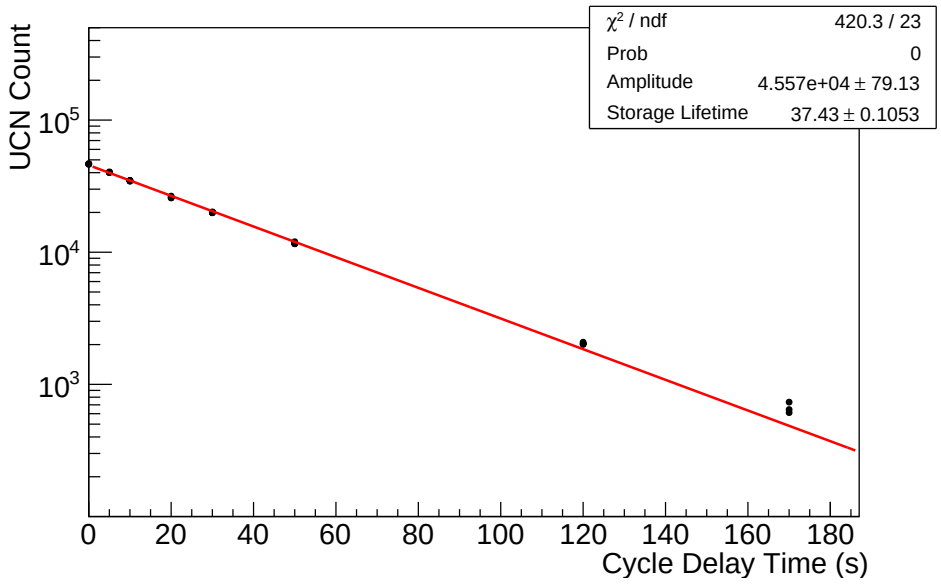

(a)

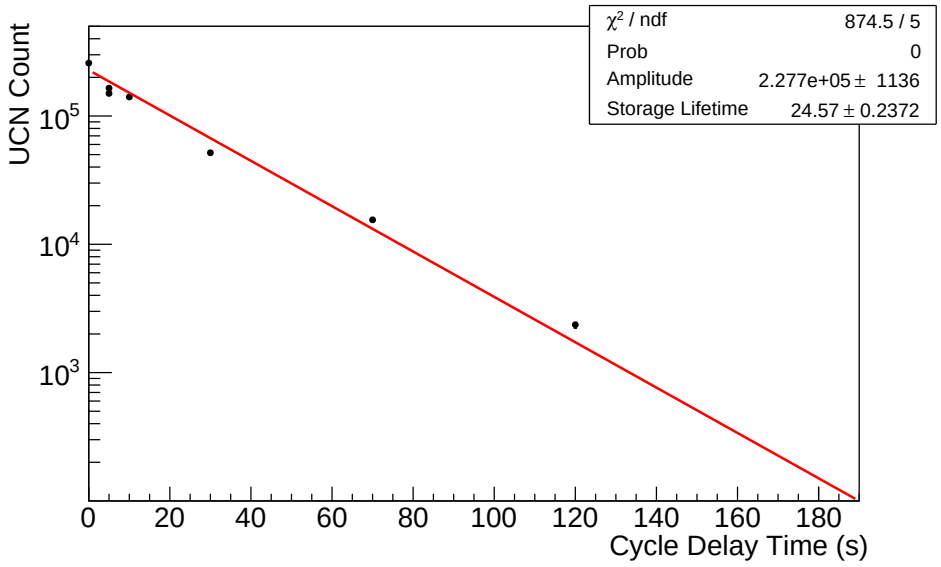

(b)

Figure 5.15: The total UCN counts at different valve open delay times for (a) 1 μA beam current and 60 s irradiation time and (b) 10 μA beam current and 30 s target irradiation time. The red line is a single exponential fit. The initial UCN counts for the 10 μA target irradiation is higher. However, the storage lifetime is lower compared to 1 μA beam current because of the heat load on the superfluid helium. In the case of 10 μA beam current, the maximum cycle delay time is 120 s compared to the 170 s delay time in the case of 1 μA beam current. This is due to excessive heat load on the cryostat and low statistics.

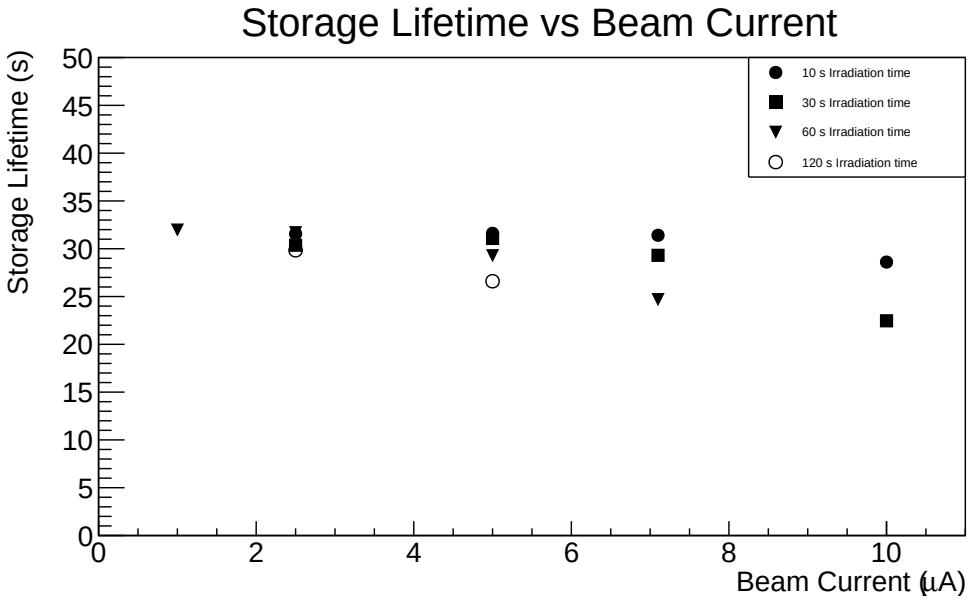

Figure 5.16: Storage lifetime in the source at different irradiation times and proton beam currents. Different markers refer to different target irradiation times. At longer irradiation times and higher beam currents, the storage lifetime decreases due to the increased heat load in the source, and an increase in the superfluid helium temperature.

5.4.2 Storage Lifetime Versus Isopure Helium Temperature

The storage lifetime of UCN was also measured at different temperatures of the superfluid helium. In this experiment, the temperature of the superfluid was increased by using heater wire wrapped around the UCN bottle. The heater power was set to increase the temperatures by a certain amount. Once the temperature stabilized, target irradiation was started.

The result of this measurement is shown in Fig. 5.17. The vertical axis is the storage lifetime of UCN in seconds, and the horizontal axis is the temperature of the superfluid helium. As mentioned earlier, the four temperature sensors that measure the temperature of the superfluid show some discrepancy. As a result, for a given measurement, there are four different values for the temperature of the superfluid. The vertical error bars come from the fit, and the horizontal error bars are set as $(T_{\max} - T_{\min})/2$, as discussed earlier. The data show a downward trend. As the temperature of the superfluid helium increases, the storage lifetime in the source decreases. This is due to higher upscattering rate in the superfluid helium at higher temperatures.

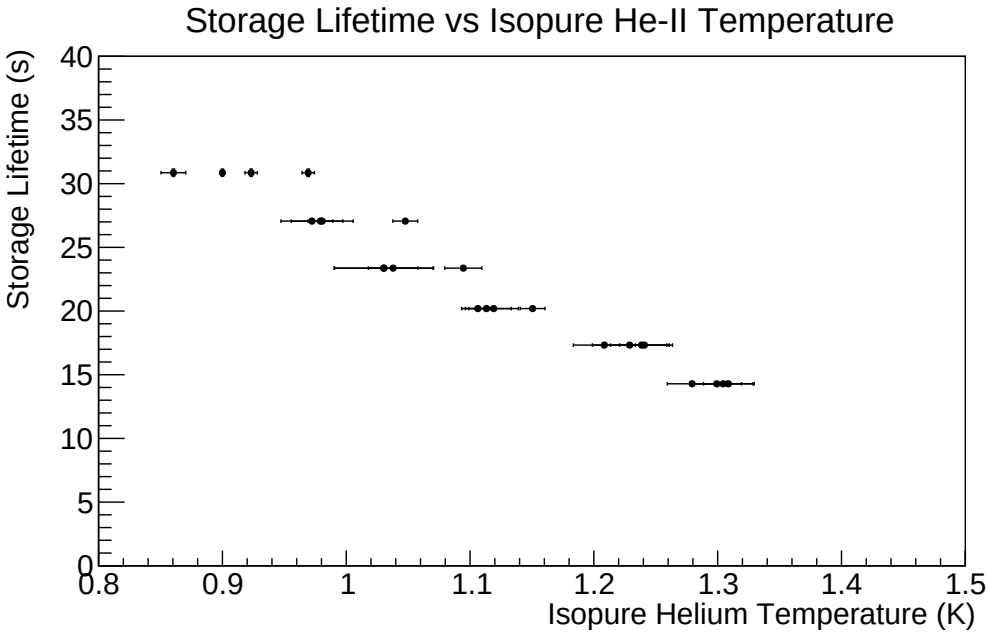

Figure 5.17: Storage lifetime of UCN at different isopure helium temperatures. In this experiment, the temperature of the superfluid helium was set using heater tapes around the UCN bottle. The vertical axis shows the storage lifetime in seconds and the horizontal axis shows the superfluid helium temperature in Kelvin. As the temperature increases, the storage lifetime decreases. This is due to higher upscattering rate in the superfluid helium at higher temperatures.

5.4.3 Storage Lifetime Over Experimental Period

Standard storage lifetime measurements were performed on a daily basis over the course of the experimental run. This includes the irradiation of the target at 1 μA proton beam current for 60 s. The result of those measurements is shown in Fig. 5.18. Over a two week period, the storage lifetime decreased from 37 s to 27 s. This is possibly due to progressive contamination in the UCN source after opening the UCN valve.

5.5 Main Results

For a better understanding of the loss mechanisms of UCN, the experiments were also simulated in PENTrack [110]. PENTrack is a particle tracking simulation software which simulates the trajectories of UCN and their decay products (e.g., protons and electrons) and their spin precession in complex geometries in electric and magnetic fields by solving the relativistic equations of motion.

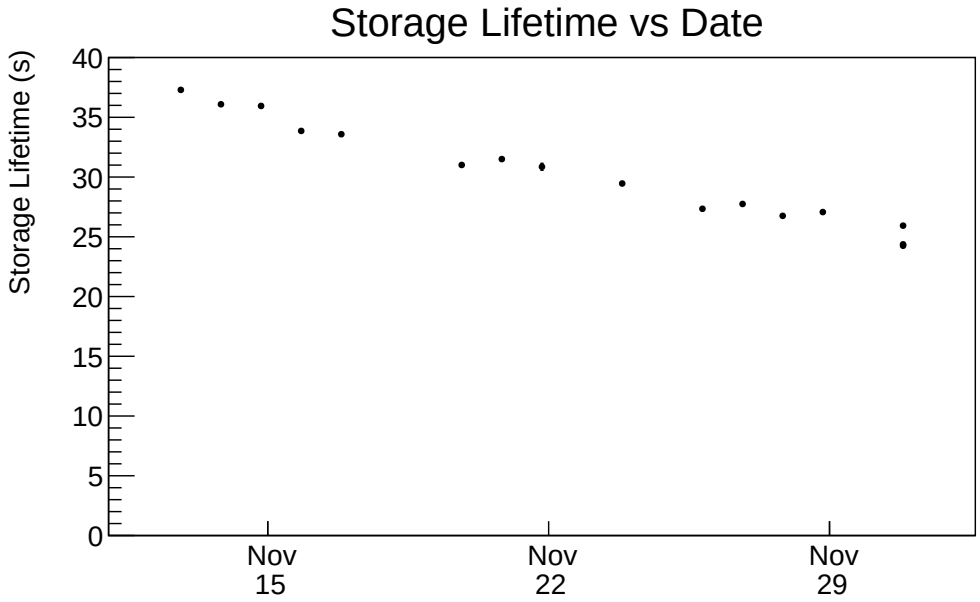

Figure 5.18: Storage lifetime in the source over the experimental run. A 2% daily decrease in the storage lifetime is observed possibly due to the contamination in the source after opening the UCN valve. The two different values of the storage lifetime at the end of the experimental run is due to different configuration.

To simulate the UCN storage and transport, an exact model of the UCN guides for PENTrack was built by the TUCAN team. Here the result of those simulations and comparison to the measured data are presented.

5.5.1 UCN Guide Diffusivity

As discussed in Chapter 1, UCN interact with all four fundamental forces. To describe the interaction of UCN with matter, a complex optical potential is used to describe matters

$$U = V - iW \ , \tag{5.8}$$

where the real part, V, depends on the number density and bound coherent scattering lengths of each nucleus species. The imaginary part, W, depends on the loss cross-section for a given velocity. Upon the incidence of a UCN on a surface, it can be reflected either specularly or diffusely. Specular reflection from a smooth surface is at an angle equal to the incident angle. Diffuse reflection from rough surfaces tends to be in all directions.

PENTrack simulations were performed to extract the diffusivity of the UCN guides (see

Fig. 4.8). Experimental geometries imported in PENTrack are the STL files made through CAD models. For these simulations, the exact model of the vertical UCN source was used including the burst disk, the actual shape of the UCN valve in the open and closed state, the pinhole detector, the foil and the main ^{6}Li detector (see Section 4.3 for more details).

In the PENTrack simulations, the interaction of UCN with material boundaries and bulk material is handled by determining the UCN track intersections with the STL mesh triangles and selecting the relevant model to describe the behaviour: specular reflection, diffuse reflection (Lambert model or Microroughness model), transmission via Snell's law, diffuse transmission (Lambert model or Microroughness model), absorption or upscattering at a material boundary, and absorption or upscattering in the bulk of the material. To track particles, PENTrack performs a 5th-order-Runge-Kutta integration of a general, relativistic equation of motion including gravitational acceleration, Lorentz forces due to magnetic and electric fields, and the force of the magnetic gradient field on the particle's magnetic moment. To simulate the precession of spins in magnetic fields, PENTrack can integrate the Bargmann-Michel-Telegdi (BMT) equation along a particle's trajectory.

The material list includes real and imaginary optical potentials, Lambert reflection probabilities, Microroughness parameters, and spin-flip probabilities. The imaginary optical potential of a material can vary with temperature and thus materials must be treated separately at different temperatures. PENTrack has no direct temperature parameter, so the imaginary optical potentials were calculated. Only the Lambert model was used for the simulations to study the transmission properties of UCN guides.

In PENTrack simulations, the optical potential of materials is used to model their interaction with UCN. The imaginary part of the optical potential (W) determines the loss of UCN (see Section 1.5). Table 5.1 collects the material parameters used in our simulations. The absorption in the foil is set according to the measurements in [163]. The main detector was modelled with its two scintillator layers [112] and their corresponding optical potentials and absorption cross-section, as stated in [164]. In the simulations, it is assumed that the spectrum of produced UCN is proportional to $\sqrt{E}$ and that the upscattering rate in the superfluid helium follows $\tau_{\mathrm{He}} = BT^7$, with B between 0.008 s^{-1}

Material	Optical Potential (neV)	Diffusivity
He-II	$18.8 - 0.5\hbar BT^7 i$	0.16
He vapour	$-0.5\hbar\tau_{\text{vapour}}^{-1} i$	0
Production volume (NiP)	$213 - 0.120i$	0.05
Guides (stainless steel)	$183 - 0.140i$	0.03
Foil (aluminium) [163]	$54.1 - 0.00281i$	0.20
GS30 scintillator [164]	$83.1 - 0.000123i$	0.16
GS20 scintillator [164]	$103 - 1.24i$	0.16

Table 5.1: Material parameters used in PENTrack simulation.

and 0.016 s^{-1} as measured by [63]. The imaginary optical potentials of the UCN guides and the production volume were tuned (see Table 5.1) to give a storage lifetime in the source (τ_1) that matches the storage lifetime during the middle of the experimental run.

The helium vapour above the liquid is included in the simulations with an upscattering rate $\tau_{\text{vapour}}^{-1} = \langle v \rangle \, n \sigma_{\text{He,n}}$ depending on the average atomic velocity $\langle v \rangle$ which is given by the vapour temperature, the vapour density n given by the saturated vapour pressure of the liquid and the vapour temperature, and the thermal-neutron-scattering cross-section of helium $\sigma_{\text{He,n}} = 0.76$ b. This is because the temperature of the vapour right above the superfluid helium liquid is the same as the superfluid temperature itself and it increases to room temperature while moving along the guides. In this model, since the helium vapour above the liquid has much higher temperature than the superfluid helium liquid, the helium atoms have much higher velocities as compared to the UCN. As a result, it might seem that the UCN are stationary. Therefore, in the reference frame of the helium atoms, thermal neutrons are moving towards the helium atoms. It was assumed that the vapour has the same temperature gradient as measured by several temperature sensors on the outer guide wall. To include the temperature gradient in the simulation, the guide volume was split into 10 cm long sections and each assigned an averaged UCN upscattering rate in that section.

To match the simulated UCN transport with the measured data more accurately, both the simulated and measured UCN rate in the detector after opening the valve at $t = 0$ were fitted with the function

$$R(t) = R_0 \left[1 - \exp\left(-\frac{t - \Delta t}{\tau_{\text{rise}}}\right)\right] \exp\left(-\frac{t - \Delta t}{\tau_2}\right) + R_B \tag{5.9}$$

In this equation, Δt is the delay time between opening the valve and detecting the first UCN which is typically 2 to 3 s in the measurements. The parameter R_B is the background UCN rate in the experimental data and is zero in the simulations. The fit function, the rise time τ_{rise}, and the fall time τ_2 are shown in Fig. 5.19 for a given UCN cycle.

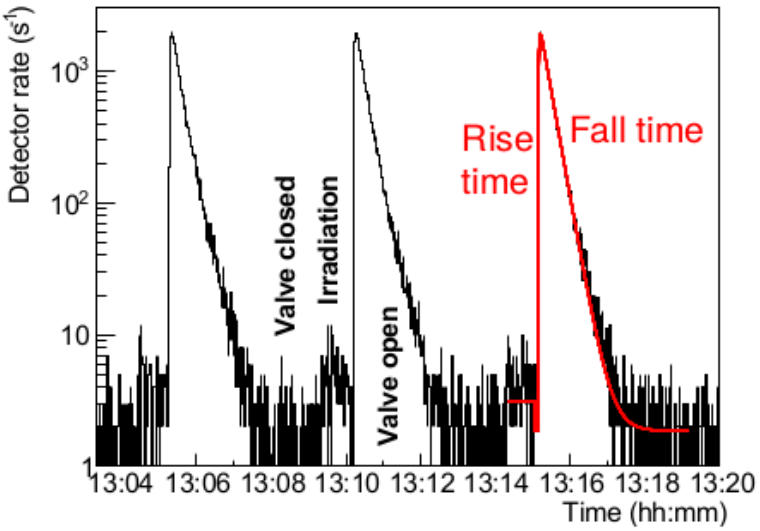

Figure 5.19: UCN rate with two exponential fit shown in red. The rise time and fall time are labelled.

In the simulations, the Lambert model was used to tune the probability of UCN being diffusely reflected on the guide walls to match the rise time and fall time of the UCN rate in the storage lifetime measurements (see Figs. 5.20 and Fig. 5.21). The delay time Δt is a constant in all scenarios. In the graphs, the data are shown by ROIes and the simulation results for different UCN guide diffusivities are shown by different markers. The ROIes indicate the second and third quartile of the experimental data. The median lies between the second and third quartile. Median divides the data into two parts where the equal number of data points lie above and below it. The lowest 25% of data points are in the first quartile, the next 25% are in the second quartile, the next 25% are in the third quartile, and the highest 25% are in the fourth quartile. Each quartile contains a

quarter of the data.

Diffuse reflection probabilities of 1% and 10% clearly result in too short and too long time constants. The experimental fall time can be matched with diffuse reflection probabilities of 3% and 5%. The rise time is best matched with 3%. This value is similar to values reported for a range of UCN guides [165–167].

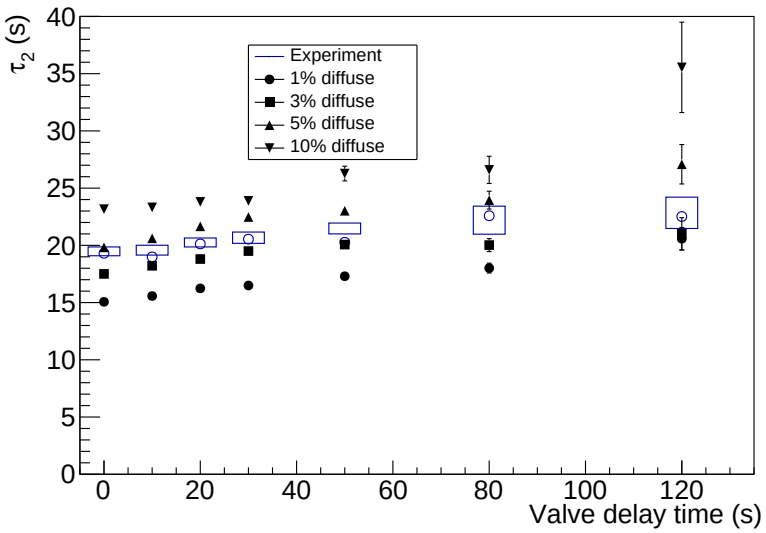

Figure 5.20: Comparison of fall time τ_2 in the experimental data and the simulations with different diffuse-reflection probabilities. The boxes indicate the second and third quartile of the experimental data (see text for the definition of quartiles). The empty circle indicates its average.

5.5.2 UCN Yield and Storage Lifetime Simulations

To estimate the UCN production, an accurate model of target, moderator and UCN converter geometries was built for MCNP 6.1, taking into account material impurities determined from assays and fill levels of liquid moderator vessels (see Fig. 5.22). The full source was then simulated: the proton beam hitting the target, secondary neutrons, protons, photons, and electrons, and neutron moderation in graphite and heavy water. In contrast to liquid heavy water, no detailed data on thermal neutron scattering in solid heavy water were available. Instead, we relied on a free-gas model with an effective temperature of 80 K, as this seems to be the minimum effective neutron temperature achieved with solid heavy water moderators [168]. From the simulated cold neutron flux in the

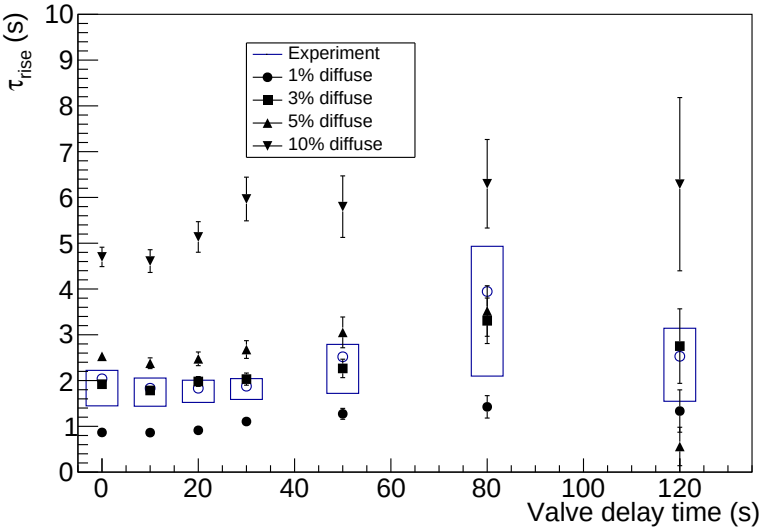

Figure 5.21: Comparison of rise time τ_{rise} in experimental data and simulations with different diffuse-reflection probabilities. The boxes indicate the second and third quartile of the experimental data (see text for the definition of quartiles). The empty circles indicate the average.

UCN production volume and UCN production cross sections from [54, 169], a production rate of (20600 ± 200) s^{-1} in an energy range up to 233.5 neV was determined. This value for the production rate was then used in the storage lifetime simulations in PENTrack.

Figures. 5.23 and 5.24 show the measured UCN counts and storage lifetime versus the super fluid helium temperature for all four temperature sensors as well as their simulations. The UCN upscattering rate in superfluid helium is $\tau_{\text{up}}^{-1} = BT^7 = 2W/\hbar$ (see Section 1.5). The imaginary optical potential was calculated for two values of B ($B = 0.016$/s and $B = 0.008$/s, with T in K) at the desired temperature in the Pentrack simulations.

In these graphs, the filled circles represent the measured data, and the empty squares and triangles represent the simulations. The empty squares are the simulations where the helium vapour above the superfluid helium liquid is included, and empty triangles are the simulations without the helium vapour. The interpolations for the squares are shown in solid lines and the interpolations for the empty triangles are shown with dotted and dashed lines. The lines are only shown for readability and are interpolation of the simulated points.

The simulations include two values for the upscattering parameter B: $B = 0.016$ s^{-1}, which represent the lower thick solid line (empty squares which represents the model

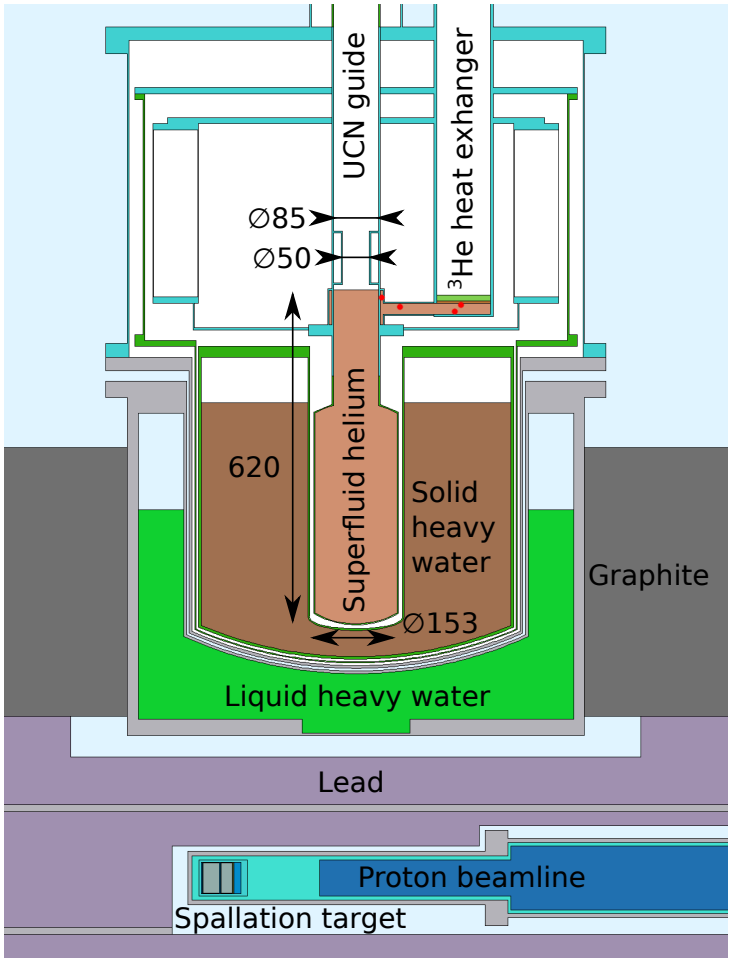

Figure 5.22: MCNP model of the source. Red dots indicate the temperature sensors used to determine the temperature of the superfluid.

where the helium vapour above the superfluid helium liquid is included) and the dotted line (empty triangles where the helium vapour above the superfluid helium liquid is not included), and $B = 0.008$ s^{-1} which represents the solid line (empty squares) and the dashed line (empty triangles). For the simulations with $B = 0.016$ s^{-1}, when the helium vapour is also included (thick solid line), the measured data and simulations match very well. Simulations without including the liquid vapour (empty triangles, dotted and dashed lines) show significant differences at higher liquid temperatures. In this model, the storage lifetime and the UCN yield at higher temperatures are overestimated. The reason for this is because of the high upscattering rate of UCN in the helium vapour.

The UCN rate in the steady-state mode of operation was measured at different proton beam currents. When the proton beam current is above 1 μA, the temperature of the superfluid helium increases due to the excess heat load. This causes the UCN rate

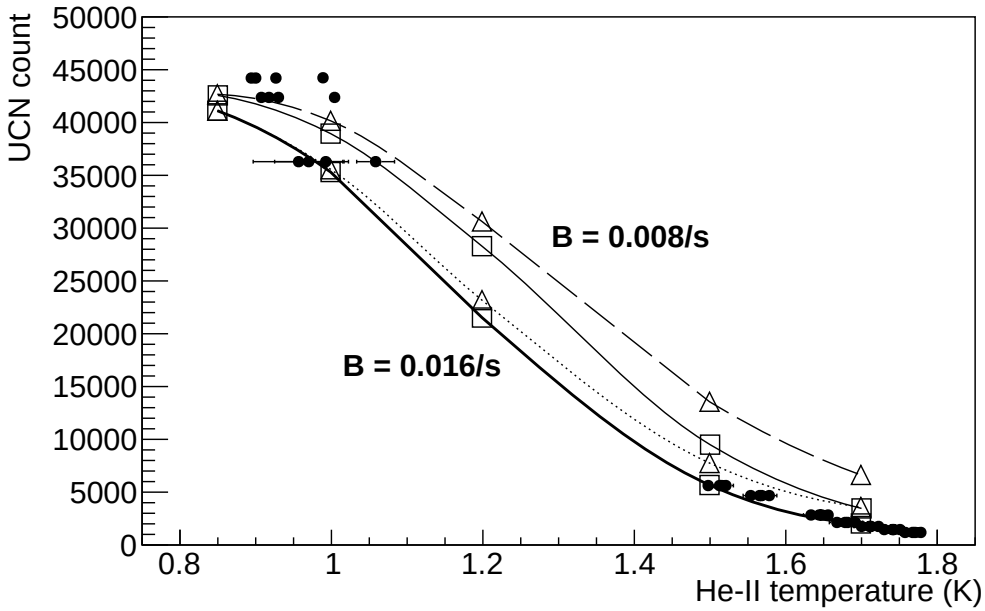

Figure 5.23: Number of UCN extracted from the source at different superfluid helium temperatures after irradiating the target with 1 μA proton beam current for 60 s(filled circles). The empty squares represent the simulations where the helium gas above the superfluid helium liquid is taken into account and the empty triangles represent the simulations where the helium gas is not included. The lines are interpolations of simulated data to guide the eye. The simulations were performed with two values of B: $B = 0.008$/s (as shown with the top two lines) and $B = 0.016$/s (as shown with the bottom two lines). The measured data is best matched with the simulations where $B = 0.016$/s where the helium gas is also taken into account.

to slowly decrease. The overall result of those measurements and their simulations is shown in Fig. 5.25. The empty squares represent the simulations where the helium vapour above the superfluid helium liquid is included in the simulations, and the empty triangles represent the case where the helium vapour is excluded. The interpolation of the simulations are shown in lines. The simulations are performed for two values of parameter B: $B = 0.016$/s and $B = 0.008$/s. The simulated data with a liquid helium upscattering parameter of $B = 0.016$ s^{-1} (thick solid line) slightly overestimates the drop in the UCN rate with temperature. With $B = 0.008$ s^{-1} (solid line), it slightly overestimates the UCN rate, but better matches the drop with temperature.

Unfortunately, the discrepancies between the temperature sensors in the superfluid helium prevent a more accurate determination of the upscattering parameter.

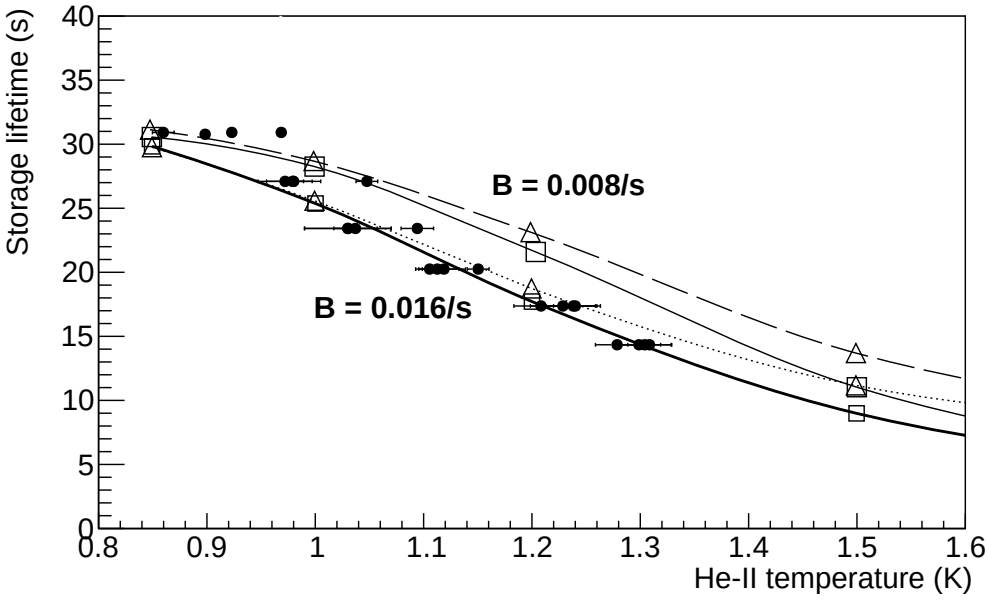

Figure 5.24: Storage lifetime of UCN in the source at different superfluid helium temperatures (filled circles). The empty squares represent the simulations where the helium gas above the superfluid helium liquid is taken into account and the empty triangles represent the simulations where the helium gas is not included. The lines are interpolations of simulated data to guide the eye. The simulations were performed with two values of B: $B = 0.008$/s (the top two lines and $B = 0.016$/s. The measured data is best matched with the simulations where $B = 0.016$/s where the helium gas is also taken into account. The lines are interpolations of simulated data to guide the eye.

5.6 Heater Test Versus Proton Beam Current

One of the UCN experiments was designed to match the heater power from the heaters wrapped around the UCN bottle with the proton beam current. This type of measurements helps to understand the input heat load on the cryostat from the beam.

The result of additional heater tests is discussed in Ref. [157]. Applying heat to the superfluid helium bottle gives rise to a temperature increase in the superfluid helium, as well as a flow rate increase in the ^{3}He pot. This heat load is known simply from the applied voltage and current to the heater wire. However, the input heat load is not known in the case of the target irradiation. As a result, the steady-state UCN yield were measured at different proton beam currents to calibrate the proton beam current with the input current on the heaters. The target irradiation at higher beam currents give rise to a temperature increase in the superfluid helium. In addition, the increase in the heat load increases the ^{3}He flow rate in the ^{3}He pot. The comparison of the temperature and

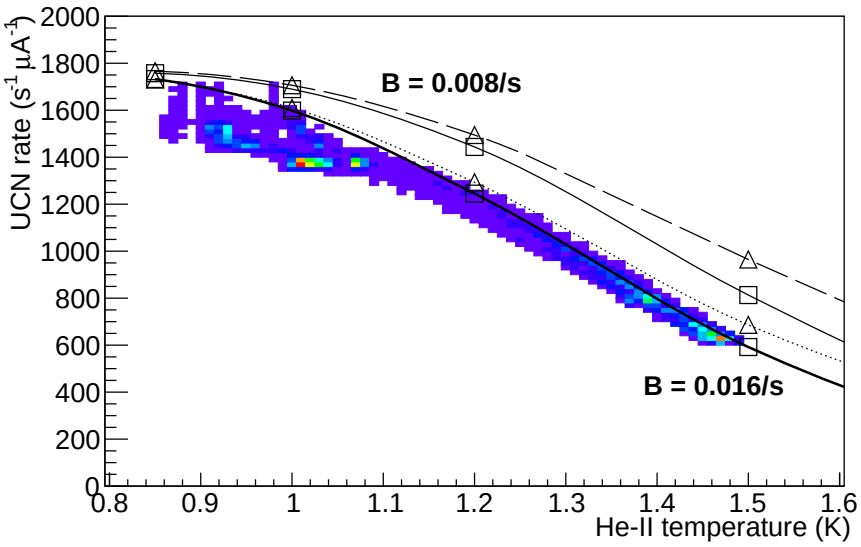

Figure 5.25: Histogram of measured UCN rates and temperatures from all four temperature sensors while the target is continuously irradiated with the UCN valve open. The empty squares represent the simulations where the helium gas above the superfluid helium liquid is taken into account and the empty triangles represent the simulations where the helium gas above the superfluid helium liquid is not included.The lines are interpolations of simulated data to guide the eye. The simulations are performed for two values of B: $B = 0.016$/s (shown by the two bottom lines), and $B = 0.008$/s (shown by the top two lines).

flow rate increase between these experiments gives an idea of the amount of applied heat load on the superfluid helium bottle for each given proton beam current.

Even though the result of the data analysis for this experiment was not conclusive, it gave an idea of the stability and the behaviour of the helium cryostat, and a better experimental plan for the future.

Some unexpected anomalies were observed during the measurements. For instance, when the 4 K reservoir was being filled, the flow rate in the ^{3}He pot as well as the temperature in the superfluid helium was not stable nor reproducible. Another problem arose from the wait time between the measurements. Before conducting a new measurement, it is essential to wait long enough so that the superfluid helium temperature and ^{3}He flow rate stabilize. In some cases, the wait time between the measurements was not long enough, and therefore it was not possible to assign a change in the superfluid helium temperature or ^{3}He flow rate. In addition, target irradiation should be long enough so that the temperature and the ^{3}He flow rate reach a stable value.

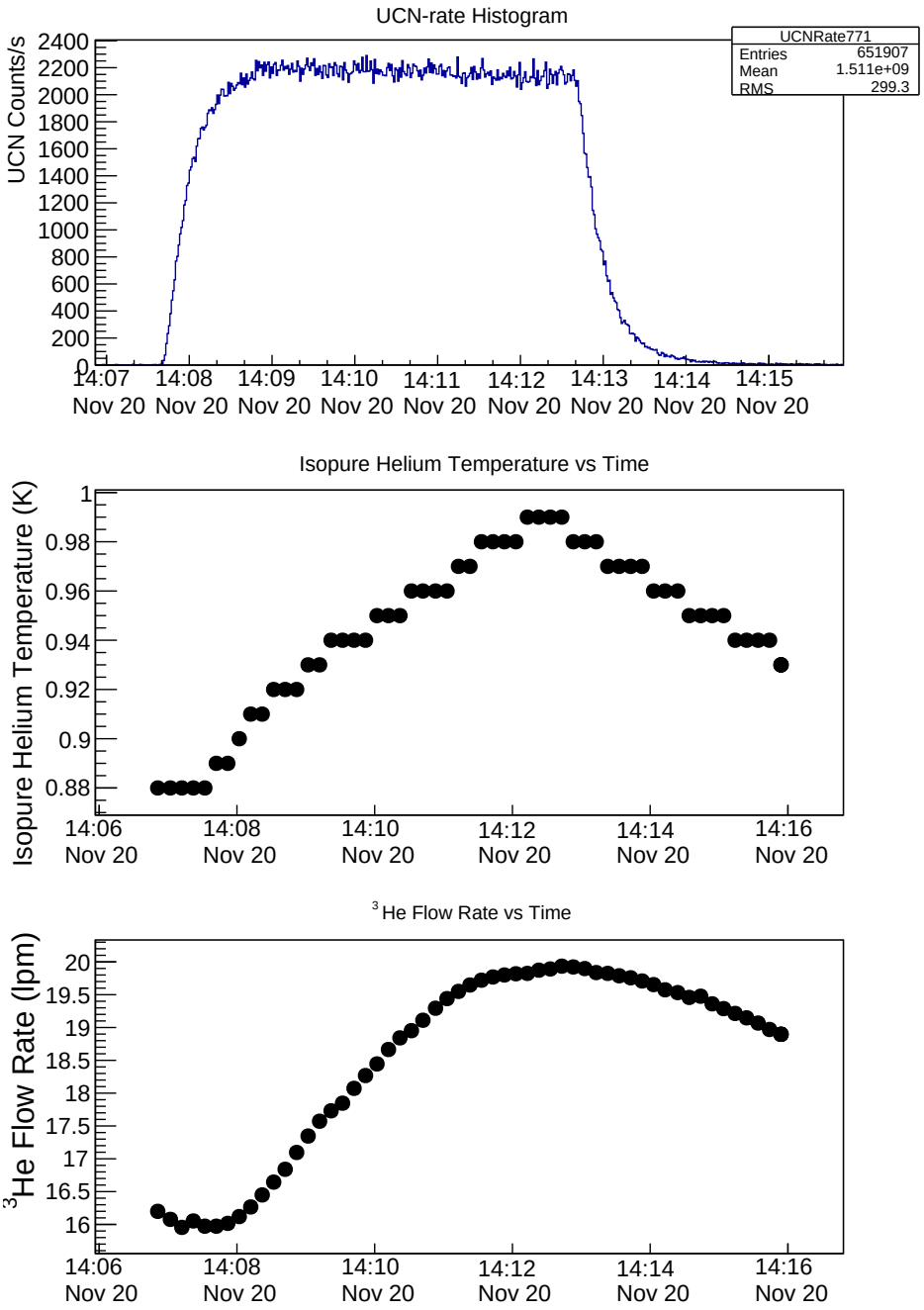

Figure 5.26: Steady-state UCN production data for 1.5 μA proton beam current. The top graph shows the UCN rate over time, the middle graph shows the superfluid helium temperature (TS12) over time and the bottom graph shows the ^{3}He flow rate versus time. Detail provided in text.

Fig. 5.26 shows an inconclusive run. The top graph shows the UCN rate over time. This shows an increase in the UCN rate after starting the target irradiation. At the end of the irradiation, the UCN rate decays to the typical background rate. The middle graph shows the temperature of the superfluid helium from the temperature sensor TS12 over

time. Here the irradiation of the target stopped before the superfluid helium could reach a stable saturation value. The bottom graph shows the flow rate in the ^{3}He from sensor FM1 (see Fig. A.1 to see the position of the sensor). At the beginning of the run, the flow rate was still going down, and it did not reach a minimum stable value. Typically this value was around 14 SLM. In addition, the flow rate did not reach a maximum saturation value due to short target irradiation time. Therefore, due to missing information, the observed change in the ^{3}He flow rate was not a good measure of the input heat load on the cryostat and no result can be concluded.

5.7 Summary

We successfully operated a superfluid-helium source for UCN at a spallation source at TRIUMF. The result of the first UCN production with this source at TRIUMF were discussed in this chapter. The measurements include the UCN yield experiments, UCN storage lifetime experiments, and steady-state UCN production experiments as well as their simulations.

The maximum number of UCN achieved for the standard 1 μA proton beam current at 60 s target irradiation time was 40,000, and the highest number of UCN counts was 325,000 at 10 μA beam current and 60 s target irradiation time which was a new record for this source. Dividing this number by the total guide volume of 60.8 L yields a UCN density of 5.3 cm^{-3}. The experimental period took about two weeks. In this time, the storage lifetime of UCN decreased from 37 s to 27 s with about 2% decrease per day due to the source contamination after opening the UCN valve. The UCN counts also showed a decrease of about 40% due to the source contamination as well as different experimental configuration at later dates. The steady-state UCN rate was shown to be around 1600 UCN/s/μA.

Although we were able to extract three times more UCN than ever before due to the increased beam current on the spallation target, we achieved only half of the previous best storage lifetime, mostly due to the contamination of the source while it was moved

from RCNP to TRIUMF, the burst disk added to the UCN guide, and the new UCN valve which was not being optimized for UCN storage.

The UCN production rate from MCNP simulations was found to be (20600 ± 200) s^{-1} in an energy range up to 233.5 neV with $\sqrt{E_{\mathrm{UCN}}}$ energy spectra. Simulations including the temperature-dependent up-scattering in superfluid helium and helium vapour confirm that the former follows $\tau_{\mathrm{He}}^{-1} = BT^7$, matching the experimental UCN yield and storage lifetime best with B between 0.008/s and 0.016/s. Upscattering in helium vapour plays a significant role at liquid temperatures above 1 K.

Future operation of this source will focus on better management of contamination to increase the storage lifetime and on tests of new UCN guides, valves, polarizers, and storage volumes.

This research provides the prerequisites for future developments: a next-generation source with cooling power and UCN flux increased by two orders of magnitude, and an experiment to measure the nEDM with a sensitivity of 10^{-27} e·cm. The good agreement of simulations and experiment makes us confident that we can predict the performance of this future source and experiment.

Chapter 6

Conclusion

The work presented in this thesis is part of the R&D studies towards the future nEDM experiment at TRIUMF. The existence of a non-zero nEDM would indicate a new source of CP violation beyond the standard model. Theories of new physics beyond the standard model predict such sources. Based on the Sakharov conditions, new sources of CP violation are essential to create the observed baryon asymmetry in the universe.

The focus of the research in this thesis was on the two aspects of the nEDM measurement:

- Magnetic field stability (focused on temperature related effects)
- UCN production and storage

and I first summarize these results.

6.1 Magnetic Field Requirements and Stability

To measure the nEDM, an ensemble of polarized UCN are placed in the presence of aligned electric and magnetic fields. The Larmor precession frequency of the UCN is measured once when the electric and magnetic fields are parallel, and once when they are anti-parallel. The frequency shift between these two geometries is proportional to the nEDM. In this process, the existence of a very stable and homogeneous magnetic environment is essential. The applied DC magnetic field should be held constant. To achieve the

magnetic requirements several layers of magnetic shielding are employed including active and passive shielding. Internal coils are placed inside the passive shielding to create the DC magnetic field. In the past, experiments used coils where the return yoke corresponded to the innermost magnetic shielding layer. These are referred to as "shield-coupled" coils. In this case, a change in the properties of the innermost passive shield, such as its magnetic permeability μ, would affect the magnetic field measured internally. One of the factors that can cause such changes in μ is the changes in the environmental temperature.

In Chapter 3 the result of the studies of the changes of μ with temperature were presented and discussed. Two methods were pursued to study the correlation of the changes in the measured internal magnetic field with respect to the changes in temperature. For those measurements, we used small witness cylinders (15.2 cm in length and 5.2 cm in diameter) made of the same material and annealed at the same time as the prototype passive shields. As a result, we expected them to have the same magnetic properties of the larger passive shields while having the advantage of being easier to perform experiments with.

In method one, a witness cylinder was put inside a coil system that produced a low-frequency magnetic field. The axial shielding factor as a function of temperature was then measured. These measurements were repeated with two different coils to study the systematic effects. In the second technique, which is more common, the witness cylinder was used as a core of a transformer. A primary and a secondary coil were wound on the witness cylinder. Here the slopes of the minor $B-H$ loops as a function of temperature were measured.

The measurements were conducted in AC fields with frequencies around 1 Hz as opposed to the DC fields in the actual nEDM experiments. To relat the shielding factor measurements to $\mu(T)$, finite element simulations were performed to find the shielding factor of the witness cylinders as a function of μ. Combining the measurements and the simulations, it was found that $0.6\%/\mathrm{K} < \frac{1}{\mu}\frac{d\mu}{dT} < 2.7\%/\mathrm{K}$ with an H_m-amplitude of 0.004 A/m at 1 Hz. In the second method, it was found that $0.0\%/\mathrm{K} < \frac{1}{\mu}\frac{d\mu}{dT} < 2.2\%/\mathrm{K}$ with a typical H_m-amplitude of 0.1 A/m at 1 Hz. For a typical nEDM experiment,

$H_m < 0.007$ A/m.

Considering the overall range implied by the measurements of $0.0\%/\text{K} < \frac{1}{\mu}\frac{d\mu}{dT} < 2.7\%/\text{K}$ and the generic EDM experiment sensitivity of $\frac{\mu}{B_0}\frac{dB_0}{d\mu} = 0.01$, the temperature dependence of the magnetic field in a typical nEDM experiment would be $\frac{dB_0}{dT} = 0 - 270$ pT/K. This means, to safely achieve the magnetic stability goal of 1 pT for hundreds of seconds in the interal field (for the worst case temperature slope), the temperature of the innermost magnetic shield in the nEDM experiment should be controlled to < 0.004 K level which puts a challenging constraint on the future nEDM experiment design. Achieving this level of temperature control is very difficult. As a result, TUCAN collaboration is now considering the self-shielded coil designs as the baseline for the future nEDM experiment.

6.2 Overview of UCN Studies at TRIUMF

The second half of this thesis was focused on the new UCN facility at TRIUMF. In 2016, the prototype vertical UCN source, previously built and tested in Japan, was shipped to TRIUMF. The unique feature of this facility is the production UCN by combining spallation neutrons with a superfluid helium converter.

In November 2017 the first UCN were produced with the prototype vertical source at TRIUMF. The experiments that were conducted include measurements of the UCN yield, UCN storage lifetime and UCN rate in the steady-state mode of operation. Those experiments and their simulations were presented in Chapter 5. Such experiments are essential for a better understanding of the UCN cryostat and for the design of the next generation UCN source.

Around 40,000 UCN were detected for the standard measurement of 1 μA proton beam current while irradiating the target for 60 s. The maximum number of UCN produced was 325,000 at 10 μA proton beam current. Over the three weeks of the experimental run period, the measured storage lifetime of UCN dropped from 37 s to 27 s. This is likely due to contamination of the source when the UCN valve was opened. The UCN

yield for the standard measurements at 1 μA proton beam current and 60 s irradiation time also dropped correspondingly by about 40%. Other than the source contamination, different experimental configuration in the second half of the experimental period caused this drop.

We could successfully produce three times more UCN than ever before. However, our UCN storage lifetime was only half of the previously best storage lifetime. This is most likely due to a combination of the contamination in the source, the existence of the burst disk, and the non-optimized UCN valve for the UCN storage. The result of the simulations proved that the upscattering rate in the superfluid helium follows $\tau_{\mathrm{He}}^{-1} = BT^7$. In addition, the UCN yield and the UCN storage lifetime simulations matched the experimental values best when the B values were between 0.008/s and 0.016/s. At higher temperatures above 1 K, the upscattering in the helium vapour plays a significant role.

6.3 Overall Conclusion and Future Work

The research presented in this thesis is part of the TUCAN's ongoing R&D towards the future nEDM measurement at TRIUMF. The experimental goal is to measure the nEDM with the sensitivity level of 10^{-27} e·cm.

The best previous measurement of the nEDM showed that the dominant systematic uncertainty is due to the magnetic field instability. As a result, one source of systematic uncertainty, the temperature dependence of magnetic permeability μ, was studied. The result of those measurements as well as the relevant simulations showed that, to fulfill our 1 pT internal magnetic field stability requirement, the temperature of the innermost magnetic shield for the nEDM experiment should be controlled to better than 4 mK level while employing the shield coupled coils to generate the DC field.

The current nEDM experiments suffer from low UCN statistics. The UCN experiments with our prototype UCN source provide the prerequisites for building our next-generation UCN source with cooling power and UCN flux increased by two orders of magnitude (see Section 2.1). The excellent match of the simulations and experiments

presented in Chapter 5 makes us confident that we can predict the performance of this future source and the counting statistics of the nEDM experiment very well.

Appendices

Appendix A

Vertical Source Gas Flow Diagram

The gas flow diagram of the vertical UCN source is shown in Fig. A.1. The components of the vertical source are described in Chapter 4. The main components for the gas flow include:

- The natural helium loop, including:
  - Liquid helium reservoir
  - Liquid helium pot at 1 K
- Liquid ^{3}He pot and the ^{3}He loop
- Isopure helium loop.

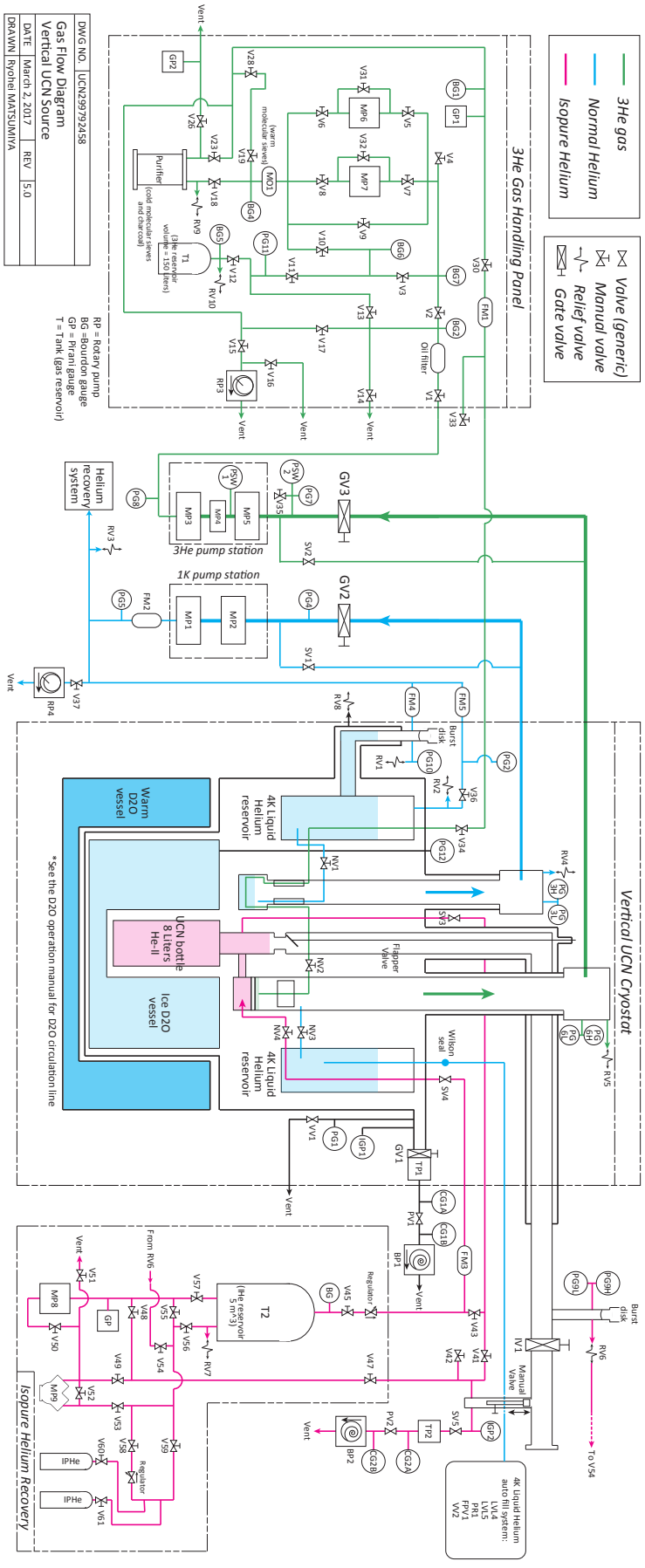

Figure A.1: Gas flow diagram for the vertical UCN source

References

[1] M. Pospelov and A. Ritz, Annals of physics **318**, 119 (2005).

[2] T. D. Lee and C.-N. Yang, Physical Review **105**, 1671 (1957).

[3] C. S. Wu, E. Ambler, R. W. Hayward, D. D. Hoppes, and R. P. Hudson, Phys. Rev. **105**, 1413 (1957).

[4] R. L. Garwin, L. M. Lederman, and M. Weinrich, Phys. Rev. **105**, 1415 (1957).

[5] J. I. Friedman and V. Telegdi, Physical Review **106**, 1290 (1957).

[6] L. Landau, Nuclear Physics **3**, 127 (1957).

[7] J. D. Jackson, S. B. Treiman, and H. W. Wyld, Phys. Rev. **106**, 517 (1957).

[8] E. M. Purcell and N. F. Ramsey, Phys. Rev. **78**, 807 (1950).

[9] J. Smith, E. Purcell, and N. Ramsey, Physical Review **108**, 120 (1957).

[10] C. Baker, D. Doyle, P. Geltenbort, K. Green, M. Van der Grinten, P. Harris, P. Iaydjiev, S. Ivanov, D. May, J. Pendlebury, *et al.*, Physical Review Letters **97**, 131801 (2006).

[11] .

[12] S. Abel, S. Khalil, and O. Lebedev, Nucl. Phys. **B606**, 151 (2001), arXiv:hep-ph/0103320 [hep-ph] .

[13] J. M. Cline, (2006), arXiv:hep-ph/0609145 [hep-ph] .

[14] A. Sakharov, Pisma Zh.Eksp.Teor.Fiz. **5**, 32 (1967).

[15] D. E. Morrissey and M. J. Ramsey-Musolf, New J. Phys. **14**, 125003 (2012), arXiv:1206.2942 [hep-ph] .

[16] J. M. Cline, *Proceedings, Higgs cosmology: Theo Murphy meeting: Buckinghamshire, UK, March 27-28, 2017*, Phil. Trans. Roy. Soc. Lond. **A376**, 20170116 (2018), [,339(2017)], arXiv:1704.08911 [hep-ph] .

[17] M. Carena, M. Quiros, and C. E. M. Wagner, Phys. Lett. **B380**, 81 (1996), arXiv:hep-ph/9603420 [hep-ph] .

[18] M. J. Ramsey-Musolf and S. Su, Physics Reports **456**, 1 (2008).

[19] R. D. Peccei and H. R. Quinn, Phys. Rev. Lett. **38**, 1440 (1977).

[20] N. Ayres, arXiv preprint arXiv:1805.10252 (2018).

[21] I. B. Khriplovich and S. K. Lamoreaux, *CP violation without strangeness* (Springer, 1997).

[22] M. Auzinsh, D. Budker, and S. Rochester, *Optically polarized atoms: understanding light-atom interactions* (Oxford University Press, 2010).

[23] A. Serebrov, P. Geltenbort, I. Shoka, G. Shmelev, A. Kharitonov, A. Vassiliev, I. Krasnoshekova, M. Lasakov, E. Siber, A. Fomin, *et al.*, Nuclear Instruments and Methods in Physics Research Section A: Accelerators, Spectrometers, Detectors and Associated Equipment **611**, 263 (2009).

[24] S. Lamoreaux and R. Golub, Journal of Physics G: Nuclear and Particle Physics **36**, 104002 (2009).

[25] I. Altarev, G. Ban, G. Bison, K. Bodek, M. Burghoff, Z. Chowdhuri, M. Daum, C. Düsing, M. Fertl, P. Fierlinger, *et al.*, Nuclear Physics A **844**, 47c (2010).

[26] J. Pendlebury, S. Afach, N. Ayres, C. Baker, G. Ban, G. Bison, K. Bodek, M. Burghoff, P. Geltenbort, K. Green, *et al.*, Physical Review D **92**, 092003 (2015).

[27] R. Pattie, N. Callahan, C. Cude-Woods, E. Adamek, L. J. Broussard, S. Clayton, S. Currie, E. Dees, X. Ding, E. Engel, *et al.*, Science **360**, 627 (2018).

[28] S. Paul, Nuclear Instruments and Methods in Physics Research Section A: Accelerators, Spectrometers, Detectors and Associated Equipment **611**, 157 (2009).

[29] F. E. Wietfeldt and G. L. Greene, Reviews of Modern Physics **83**, 1173 (2011).

[30] S. Arzumanov, L. Bondarenko, S. Chernyavsky, W. Drexel, A. Fomin, P. Geltenbort, V. Morozov, Y. Panin, J. Pendlebury, and K. Schreckenbach, Physics Letters B **483**, 15 (2000).

[31] A. Serebrov, V. Varlamov, A. Kharitonov, A. Fomin, Y. Pokotilovski, P. Geltenbort, J. Butterworth, I. Krasnoschekova, M. Lasakov, R. Tal'daev, *et al.*, Physics Letters B **605**, 72 (2005).

[32] P. R. Huffman, C. Brome, J. Butterworth, K. Coakley, M. S. Dewey, S. Dzhosyuk, R. Golub, G. Greene, K. Habicht, S. K. Lamoreaux, *et al.*, Nature **403**, 62 (2000).

[33] B. Plaster, R. Rios, H. Back, T. Bowles, L. Broussard, R. Carr, S. Clayton, S. Currie, B. Filippone, A. García, *et al.*, Physical Review C **86**, 055501 (2012).

[34] M. P. Mendenhall, R. W. Pattie, Y. Bagdasarova, D. B. Berguno, L. J. Broussard, R. Carr, S. Currie, X. Ding, B. W. Filippone, A. García, P. Geltenbort, K. P. Hickerson, J. Hoagland, A. T. Holley, R. Hong, T. M. Ito, A. Knecht, C.-Y. Liu, J. L. Liu, M. Makela, R. R. Mammei, J. W. Martin, D. Melconian, S. D. Moore, C. L. Morris, A. Pérez Galván, R. Picker, M. L. Pitt, B. Plaster, J. C. Ramsey, R. Rios, A. Saunders, S. J. Seestrom, E. I. Sharapov, W. E. Sondheim, E. Tatar, R. B. Vogelaar, B. VornDick, C. Wrede, A. R. Young, and B. A. Zeck (UCNA Collaboration), Phys. Rev. C **87**, 032501 (2013).

[35] L. Broussard and U. Collaboration, AIP Conference Proceedings **1560**, 149 (2013), https://aip.scitation.org/doi/pdf/10.1063/1.4826741 .

[36] .

[37] O. Zimmer, Physics Letters B **685**, 38 (2010).

[38] S. Baessler, V. Nesvizhevsky, K. Protasov, and A. Y. Voronin, Physical Review D **75**, 075006 (2007).

[39] A. P. Serebrov, O. Zimmer, P. Geltenbort, A. K. Fomin, S. Ivanov, E. Kolomensky, I. Krasnoshekova, M. Lasakov, V. M. Lobashev, A. Pirozhkov, *et al.*, JETP letters **91**, 6 (2010).

[40] S. Afach, G. Ban, G. Bison, K. Bodek, M. Burghoff, M. Daum, M. Fertl, B. Franke, Z. Grujić, V. Helaine, *et al.*, Physics Letters B **745**, 58 (2015).

[41] I. Altarev, Phys. Rev. Lett. **103**, 081602 (2009).

[42] V. V. Nesvizhevsky, H. Börner, A. Gagarski, A. Petoukhov, G. Petrov, H. Abele, S. Baeßler, G. Divkovic, F. Rueß, T. Stöferle, *et al.*, Physical Review D **67**, 102002 (2003).

[43] M. Tanabashi, K. Hagiwara, K. Hikasa, K. Nakamura, and Y. Sumino *et al.*, .

[44] R. Golub, D. Richardson, and S. Lamoureaux, *Ultra-cold neutrons, Adam Hilger, Bristol, Philadelphia, New York*, Tech. Rep. (ISBN 0-7503-0115-5, 1991).

[45] D. Richardson, J. Pendlebury, P. Iaydjiev, W. Mampe, K. Green, and A. Kilvington, Nuclear Instruments and Methods in Physics Research Section A: Accelerators, Spectrometers, Detectors and Associated Equipment **308**, 568 (1991).

[46] A. Steyerl, H. Nagel, F.-X. Schreiber, K.-A. Steinhauser, R. Gähler, W. Gläser, P. Ageron, J. Astruc, W. Drexel, G. Gervais, *et al.*, Physics Letters A **116**, 347 (1986).

[47] A. Steyerl, Nuclear Instruments and Methods **125**, 461 (1975).

[48] A. R. Young (JGU Mainz, Germany, 2016).

[49] R.GolubJ.M.Pendlebury, Physics Letters A **53**, 133 (1975).

[50] R. Golub and J. Pendlebury, Physics Letters A **62**, 337 (1977).

[51] C. R. Brome, J. Butterworth, S. Dzhosyuk, C. Mattoni, D. McKinsey, J. Doyle, P. Huffman, M. Dewey, F. Wietfeldt, R. Golub, *et al.*, Physical review C **63**, 055502 (2001).

[52] M. Van der Grinten, C. Collaboration, *et al.*, Nuclear Instruments and Methods in Physics Research Section A: Accelerators, Spectrometers, Detectors and Associated Equipment **611**, 129 (2009).

[53] P. R. Huffman, C. Brome, J. Butterworth, K. Coakley, M. S. Dewey, S. Dzhosyuk, R. Golub, G. Greene, K. Habicht, S. K. Lamoreaux, *et al.*, Nature **403**, 62 (2000).

[54] E. Korobkina, R. Golub, B. Wehring, and A. Young, Physics Letters A **301**, 462 (2002).

[55] P. Schmidt-Wellenburg, K. Andersen, and O. Zimmer, Nuclear Instruments and Methods in Physics Research Section A: Accelerators, Spectrometers, Detectors and Associated Equipment **611**, 259 (2009), particle Physics with Slow Neutrons.

[56] K. Kirch, B. Lauss, P. Schmidt-Wellenburg, and G. Zsigmond, Nuclear Physics News **20**, 17 (2010), https://doi.org/10.1080/10619121003626724 .

[57] G. L. Squires, *Introduction to the Theory of Thermal Neutron Scattering*, 3rd ed. (Cambridge University Press, 2012).

[58] M. Gibbs, W. Stirling, K. Andersen, and H. Schober, Journal of low temperature physics **120**, 55 (2000).

[59] M. Gibbs, K. Andersen, W. Stirling, and H. Schober, Journal of Physics: Condensed Matter **11**, 603 (1999).

[60] K. H. Andersen, W. G. Stirling, R. Scherm, A. Stunault, B. Fak, H. Godfrin, and A. J. Dianoux, Journal of Physics: Condensed Matter **6**, 821 (1994).

[61] W. Schott, J.M. Pendlebury, I. Altarev, S. Gröger, E. Gutsmiedl, F.J. Hartmann, S. Paul, G. Petzoldt, P. Schmidt-Wellenburg, and U. Trinks, Eur. Phys. J. A **16**, 599 (2003).

[62] B. Fåk and K. Andersen, Physics Letters A **160**, 468 (1991).

[63] K. K. H. Leung, S. Ivanov, F. M. Piegsa, M. Simson, and O. Zimmer, Phys. Rev. C **93**, 025501 (2016).

[64] A. Frei, E. Gutsmiedl, C. Morkel, A. R. Müller, S. Paul, S. Rols, H. Schober, and T. Unruh, EPL (Europhysics Letters) **92**, 62001 (2010).

[65] C.-Y. Liu, A. R. Young, and S. K. Lamoreaux, Phys. Rev. B **62**, R3581 (2000).

[66] C. L. Morris, J. M. Anaya, T. J. Bowles, B. W. Filippone, P. Geltenbort, R. E. Hill, M. Hino, S. Hoedl, G. E. Hogan, T. M. Ito, T. Kawai, K. Kirch, S. K. Lamoreaux, C.-Y. Liu, M. Makela, L. J. Marek, J. W. Martin, R. N. Mortensen, A. Pichlmaier, A. Saunders, S. J. Seestrom, D. Smith, W. Teasdale, B. Tipton, M. Utsuro, A. R. Young, and J. Yuan, Phys. Rev. Lett. **89**, 272501 (2002).

[67] F. Atchison, K. Bodek, B. van den Brandt, T. Brys, M. Daum, P. Fierlinger, P. Geltenbort, M. Giersch, P. Hautle, M. Hino, R. Henneck, M. Kasprzak, K. Kirch, J. Kohlbrecher, J. Konter, G. Kühne, M. Kuźniak, K. Mishima, A. Pichlmaier, and J. Zmeskal, *Journal of research of the National Institute of Standards and Technology*, **110** (2005).

[68] R. Golub and K. Böning, Zeitschrift für Physik B Condensed Matter **51**, 95 (1983).

[69] A. Anghel, T. Bailey, G. Bison, B. Blau, L. Broussard, S. Clayton, C. Cude-Woods, M. Daum, A. Hawari, N. Hild, *et al.*, arXiv preprint arXiv:1804.08616 (2018).

[70] Salvat, D. J., Gutsmiedl, E., Liu, C.-Y., Geltenbort, P., Orecchini, A., Paul, S., and Schober, H., EPL **103**, 12001 (2013).

[71] F. Atchison, B. Blau, K. Bodek, B. van den Brandt, T. Bryś, M. Daum, P. Fierlinger, A. Frei, P. Geltenbort, P. Hautle, R. Henneck, S. Heule, A. Holley,

M. Kasprzak, K. Kirch, A. Knecht, J. Konter, M. Kuźniak, C.-Y. Liu, C. Morris, A. Pichlmaier, C. Plonka, Y. Pokotilovski, A. Saunders, Y. Shin, D. Tortorella, M. Wohlmuther, A. Young, J. Zejma, and G. Zsigmond, Nuclear Instruments and Methods in Physics Research Section A: Accelerators, Spectrometers, Detectors and Associated Equipment **611**, 252 (2009), particle Physics with Slow Neutrons.

[72] E. Alsolami, *An examination of keystroke dynamics for continuous user authentication*, Ph.D. thesis, Queensland University of Technology (2012).

[73] A. Serebrov (Neutron Electric Dipole Moment Workshop, Ascona, Switzerland, 2014).

[74] F. M. Piegsa, M. Fertl, S. N. Ivanov, M. Kreuz, K. K. H. Leung, P. Schmidt-Wellenburg, T. Soldner, and O. Zimmer, Phys. Rev. C **90**, 015501 (2014).

[75] O. Zimmer and R. Golub, Phys. Rev. C **92**, 015501 (2015).

[76] T. Ito (Neutron Electric Dipole Moment Workshop, Ascona, Switzerland, 2014).

[77] D. Ries (Neutron Electric Dipole Moment Workshop, Ascona, Switzerland, 2014).

[78] J. Karch, Y. Sobolev, M. Beck, K. Eberhardt, G. Hampel, W. Heil, R. Kieser, T. Reich, N. Trautmann, and M. Ziegner, The European Physical Journal A **50**, 78 (2014).

[79] A. Kolarkar, AIP Conference Proceedings **1200**, 861 (2010), https://aip.scitation.org/doi/pdf/10.1063/1.3327748 .

[80] S. Imajo *et al.*, PTEP **2016**, 013C02 (2016), arXiv:1507.07223 [physics.ins-det] .

[81] N. F. Ramsey, Phys. Rev. **78**, 695 (1950).

[82] P. Schmidt-Wellenburg, *Proceedings, 11th Latin American Symposium on Nuclear Physics and Applications: Medellin, Colombia*, AIP Conf. Proc. **1753**, 060002 (2016), arXiv:1602.01997 [nucl-ex] .

[83] P. Schmidt-Wellenburg, (2016), arXiv:1607.06609 [hep-ex] .

[84] J. M. Pendlebury, W. Heil, Y. Sobolev, P. G. Harris, J. D. Richardson, R. J. Baskin, D. D. Doyle, P. Geltenbort, K. Green, M. G. D. van der Grinten, P. S. Iaydjiev, S. N. Ivanov, D. J. R. May, and K. F. Smith, Phys. Rev. A **70**, 032102 (2004).

[85] S. Afach, C. Baker, G. Ban, G. Bison, K. Bodek, Z. Chowdhuri, M. Daum, M. Fertl, B. Franke, P. Geltenbort, *et al.*, The European Physical Journal D **69**, 225 (2015).

[86] B. Graner, Y. Chen, E. Lindahl, and B. Heckel, arXiv preprint arXiv:1601.04339 (2016).

[87] B. Yoon, T. Bhattacharya, and R. Gupta, in *EPJ Web of Conferences*, Vol. 175 (EDP Sciences, 2018) p. 01014.

[88] S. Afach, C. Baker, G. Ban, G. Bison, K. Bodek, M. Burghoff, Z. Chowdhuri, M. Daum, M. Fertl, B. Franke, P. Geltenbort, K. Green, M. van der Grinten, Z. Grujic, P. Harris, W. Heil, V. Hélaine, R. Henneck, M. Horras, P. Iaydjiev, S. Ivanov, M. Kasprzak, Y. Kermaïdic, K. Kirch, A. Knecht, H.-C. Koch, J. Krempel, M. Kuźniak, B. Lauss, T. Lefort, Y. Lemière, A. Mtchedlishvili, O. Naviliat-Cuncic, J. Pendlebury, M. Perkowski, E. Pierre, F. Piegsa, G. Pignol, P. Prashanth, G. Quéméner, D. Rebreyend, D. Ries, S. Roccia, P. Schmidt-Wellenburg, A. Schnabel, N. Severijns, D. Shiers, K. Smith, J. Voigt, A. Weis, G. Wyszynski, J. Zejma, J. Zenner, and G. Zsigmond, Physics Letters B **739**, 128 (2014).

[89] S. Afach, C. A. Baker, G. Ban, G. Bison, K. Bodek, Z. Chowdhuri, M. Daum, M. Fertl, B. Franke, P. Geltenbort, K. Green, M. G. D. van der Grinten, Z. Grujic, P. G. Harris, W. Heil, V. Hélaine, R. Henneck, M. Horras, P. Iaydjiev, S. N. Ivanov, M. Kasprzak, Y. Kermaïdic, K. Kirch, P. Knowles, H.-C. Koch, S. Komposch, A. Kozela, J. Krempel, B. Lauss, T. Lefort, Y. Lemière, A. Mtchedlishvili, O. Naviliat-Cuncic, J. M. Pendlebury, F. M. Piegsa, G. Pignol, P. N. Prashant, G. Quéméner, D. Rebreyend, D. Ries, S. Roccia, P. Schmidt-Wellenburg, N. Severijns, A. Weis, E. Wursten, G. Wyszynski, J. Zejma, J. Zenner, and G. Zsigmond, The European Physical Journal D **69**, 225 (2015).

[90] H.-C. Koch, G. Bison, Z. D. Grujić, W. Heil, M. Kasprzak, P. Knowles, A. Kraft, A. Pazgalev, A. Schnabel, J. Voigt, and A. Weis, The European Physical Journal D **69**, 202 (2015).

[91] B. Lauss (Neutron Electric Dipole Moment Workshop, Harrison Hot Springs, BC, Canada, 2017).

[92] C. Baker, G. Ban, K. Bodek, M. Burghoff, Z. Chowdhuri, M. Daum, M. Fertl, B. Franke, P. Geltenbort, K. Green, *et al.*, Physics Procedia **17**, 159 (2011).

[93] J.-C. Peng, Modern Physics Letters A **23**, 1397 (2008).

[94] S. K. Lamoreaux and R. Golub, Phys. Rev. A **71**, 032104 (2005).

[95] S. Clayton (Neutron Electric Dipole Moment Workshop, Harrison Hot Springs, BC, Canada, 2017).

[96] S. Degenkolb (Harisson Hot Springs, BC, 2017).

[97] A. P. Serebrov and P. Geltenbort (Harisson Hot Springs, BC, 2017).

[98] I. Altarev, E. Babcock, D. Beck, M. Burghoff, S. Chesnevskaya, T. Chupp, S. Degenkolb, I. Fan, P. Fierlinger, A. Frei, *et al.*, Review of scientific instruments **85**, 075106 (2014).

[99] I. Altarev, M. Bales, D. Beck, T. Chupp, K. Fierlinger, P. Fierlinger, F. Kuchler, T. Lins, M. Marino, B. Niessen, *et al.*, Journal of Applied Physics **117**, 183903 (2015).

[100] I. Altarev, P. Fierlinger, T. Lins, M. Marino, B. Nießen, G. Petzoldt, M. Reisner, S. Stuiber, M. Sturm, J. T. Singh, *et al.*, Journal of Applied Physics **117**, 233903 (2015).

[101] R. Picker (Neutron Electric Dipole Moment Workshop, Ascona, Switzerland, 2014).

[102] T. Andalib, J. W. Martin, C. P. Bidinosti, R. R. Mammei, B. Jamieson, M. Lang, and T. Kikawa, Nucl. Instrum. Meth. **A867**, 139 (2017), arXiv:1612.06047 [physics.ins-det] .

[103] A. P. Serebrov, E. Kolomenskiy, A. Pirozhkov, I. Krasnoschekova, A. Vassiljev, A. Polushkin, M. Lasakov, A. K. Fomin, I. Shoka, V. Solovey, *et al.*, JETP letters **99**, 4 (2014).

[104] A. Serebrov, S. Boldarev, A. Erykalov, V. Ezhov, V. Fedorov, A. Fomin, V. Ilatovskiy, K. Keshyshev, K. Konoplev, A. Krivshitch, *et al.*, Physics Procedia **17**, 251 (2011).

[105] K. Kirch, in *AIP Conference Proceedings*, Vol. 1560 (AIP, 2013) pp. 90–94.

[106] I. Altarev, D. Beck, S. Chesnevskaya, T. Chupp, W. Feldmeier, P. Fierlinger, A. Frei, E. Gutsmiedl, F. Kuchler, P. Link, *et al.*, Nuovo Cimento-C **35**, 122 (2012).

[107] R. Golub and S. K. Lamoreaux, Physics Reports **237**, 1 (1994).

[108] T. M. Ito, nEdm Collaboration, *et al.*, in *Journal of Physics: Conference Series*, Vol. 69 (IOP Publishing, 2007) p. 012037.

[109] R. Picker, in *Proceedings of the 14th International Conference on Meson-Nucleon Physics and the Structure of the Nucleon (MENU2016)* (2017) p. 010005.

[110] W. Schreyer, T. Kikawa, M. J. Losekamm, S. Paul, and R. Picker, Nuclear Instruments and Methods in Physics Research Section A: Accelerators, Spectrometers, Detectors and Associated Equipment **858**, 123 (2017).

[111] The TUCAN Collaboration, "Conceptual design report for the next generation ucn source at TRIUMF," (2018).

[112] B. Jamieson, L. A. Rebenitsch, S. Hansen-Romu, B. Lauss, T. Lindner, R. Mammei, J. W. Martin, and E. Pierre, The European Physical Journal A **53**, 3 (2017).

[113] B. Franke, *Investigations of the internal and external magnetic fields of the neutron electric dipole moment experiment at the Paul Scherrer Institute*, Ph.D. thesis, ETH Zurich (2013).

[114] S. Afach, G. Bison, K. Bodek, F. Burri, Z. Chowdhuri, M. Daum, M. Fertl, B. Franke, Z. Grujic, V. Hélaine, *et al.*, Journal of Applied Physics **116**, 084510 (2014).

[115] J. W. Martin, R. R. Mammei, W. Klassen, C. Cerasani, T. Andalib, C. P. Bidinosti, M. Lang, and D. Ostapchuk, Nuclear Instruments and Methods in Physics Research Section A: Accelerators, Spectrometers, Detectors and Associated Equipment **778**, 61 (2015).

[116] R. Burrough, "Bachelor's Thesis, University of Winnipeg," (2016).

[117] T. Bryś, S. Czekaj, M. Daum, P. Fierlinger, D. George, R. Henneck, M. Kasprzak, K. Kirch, M. Kuźniak, G. Kuehne, *et al.*, Nuclear Instruments and Methods in Physics Research Section A: Accelerators, Spectrometers, Detectors and Associated Equipment **554**, 527 (2005).

[118] W. C. Griffith, M. D. Swallows, T. H. Loftus, M. V. Romalis, B. R. Heckel, and E. N. Fortson, Phys. Rev. Lett. **102**, 101601 (2009).

[119] B. Patton, E. Zhivun, D. Hovde, and D. Budker, Physical review letters **113**, 013001 (2014).

[120] J. Voigt, S. Knappe-Grüneberg, A. Schnabel, R. Körber, and M. Burghoff, Metrology and Measurement Systems **20**, 239 (2013).

[121] F. Thiel, A. Schnabel, S. Knappe-Grüneberg, D. Stollfuß, and M. Burghoff, Review of scientific instruments **78**, 035106 (2007).

[122] Z. Sun, M. Reisner, P. Fierlinger, A. Schnabel, S. Stuiber, and L. Li, Journal of Applied Physics **119**, 193902 (2016).

[123] C. Bidinosti and J. Martin, AIP Advances **4**, 047135 (2014).

[124] L. Urankar and R. Oppelt, IEEE transactions on biomedical engineering **43**, 697 (1996).

[125] A. Knecht, *Towards a New Measurement of the Neutron Electric Dipole Moment*, Ph.D. thesis, Zurich (2009).

[126] "Finite Element Method Magnetics FEMM, version 4.2, available from `http://www.femm.info`. ," .

[127] R. H. Lambert and C. Uphoff, Review of Scientific Instruments **46**, 337 (1975).

[128] T. Sumner, Journal of Physics D: Applied Physics **20**, 692 (1987).

[129] R. Bozorth, "Ferromagnetism, american telephone and telegraph company, 1978," (1993).

[130] Wikibooks, "Electronics/transformer design — wikibooks, the free textbook project," (2018), [Online; accessed 3-December-2018].

[131] G. Couderchon and J. Tiers, Journal of Magnetism and Magnetic Materials **26**, 196 (1982).

[132] F. Pfeifer and C. Radeloff, Journal of magnetism and magnetic materials **19**, 190 (1980).

[133] Krupp VDM Magnifer 7904, *Material Data Sheet No. 9004*, Tech. Rep. (Krupp VDM, Aug. 2000).

[134] "Bartington Instruments Ltd., 10 Thorney Leys Business Park, Witney, Oxon, OX28 4GG, England." .

[135] "Stanford Research Systems, 1290-D Reamwood Ave., Sunnyvale, CA 94089." .

[136] E. Paperno, IEEE transactions on magnetics **35**, 3940 (1999).

[137] D. C. Jiles, Journal of Applied Physics **76**, 5849 (1994).

[138] D. C. Jiles and D. L. Atherton, Journal of applied physics **55**, 2115 (1984).

[139] D. C. Jiles and D. L. Atherton, Journal of magnetism and magnetic materials **61**, 48 (1986).

[140] W. F. Brown Jr and J. H. Sweer, Review of Scientific Instruments **16**, 276 (1945).

[141] H. A. Wheeler, Proceedings of the IRE **46**, 1595 (1958).

[142] E. M. Purcell, American Journal of Physics **57**, 18 (1989), https://doi.org/10.1119/1.15860 .

[143] R. Beth, "Brookhaven National Laboratory Report," (), BNL-10143 (1966).

[144] R. Beth, (), US Patent 3466499, September 9, 1969.

[145] C. Bidinosti, I. Kravchuk, and M. Hayden, Journal of Magnetic Resonance **177**, 31 (2005).

[146] R. Turner and R. M. Bowley, Journal of Physics E: Scientific Instruments **19**, 876 (1986).

[147] H.-T. S.S., Concepts in Magnetic Resonance Part A **36A**, 223, https://onlinelibrary.wiley.com/doi/pdf/10.1002/cmr.a.20163 .

[148] B. M. A., F. L. K., and C. Stuart, Concepts in Magnetic Resonance **14**, 9, https://onlinelibrary.wiley.com/doi/pdf/10.1002/cmr.10000 .

[149] L. K. Forbes and S. Crozier, Journal of Physics D: Applied Physics **36**, 68 (2003).

[150] V. V. Kuzmin, C. P. Bidinosti, M. E. Hayden, and P.-J. Nacher, Journal of Magnetic Resonance **256**, 70 (2015).

[151] Y. Masuda, T. Kitagaki, K. Hatanaka, M. Higuchi, S. Ishimoto, Y. Kiyanagi, K. Morimoto, S. Muto, and M. Yoshimura, Physical review letters **89**, 284801 (2002).

[152] Y. Masuda, K. Hatanaka, S.-C. Jeong, S. Kawasaki, R. Matsumiya, K. Matsuta, M. Mihara, and Y. Watanabe, Physical review letters **108**, 134801 (2012).

[153] S. Ahmed *et al.*, (2018), arXiv:1810.01001 [physics.ins-det] .

[154] N. Christopher, "Bachelor Thesis, An amalgamation of work on the ultra-cold neutron source and neutron electric dipole moment experiment at TRIUMF," (2016).

[155] M. Kawai, K. Kikuchi, H. Kurishita, J.-F. Li, and M. Furusaka, Journal of nuclear materials **296**, 312 (2001).

[156] R. Matsumiya, *Study of He-II Spallation UCN Source*, Ph.D. thesis, Osaka University (2013).

[157] F. Rehm, "Bachelor Thesis, Heat conductivity in superfluid helium and ultracold neutron source cryogenics, University of Coburg," (2018).

[158] S. Weitz, "Bachelor Thesis, University of Coburg," (2018).

[159] S. Vanbergen, "UCN cryostat controls development and maintenance manual," (2017).

[160] R. Brun and F. Rademakers, Nuclear Instruments and Methods in Physics Research Section A: Accelerators, Spectrometers, Detectors and Associated Equipment **389**, 81 (1997).

[161] L. Rebenitch, *Detecting High Rates of Ultracold Neutrons and Thermal Neutron Production*, Ph.D. thesis, University of Manitoba (2018).

[162] S. Pomme, R. Fitzgerald, and J. Keightley, Metrologia **52**, S3 (2015).

[163] F. Atchison, B. Blau, A. Bollhalder, M. Daum, P. Fierlinger, P. Geltenbort, G. Hampel, M. Kasprzak, K. Kirch, S. Köchli, *et al.*, Nuclear Instruments and Methods in Physics Research Section A: Accelerators, Spectrometers, Detectors and Associated Equipment **608**, 144 (2009).

[164] G. Ban, G. Bison, K. Bodek, Z. Chowdhuri, P. Geltenbort, W. C. Griffith, V. Hélaine, R. Henneck, M. Kasprzak, Y. Kermaidic, K. Kirch, S. Komposch, P. A. Koss, A. Kozela, J. Krempel, B. Lauss, T. Lefort, Y. Lemière, A. Mtchedlishvili, M. Musgrave, O. Naviliat-Cuncic, F. M. Piegsa, E. Pierre, G. Pignol, G. Quéméner, M. Rawlik, D. Ries, D. Rebreyend, S. Roccia, G. Rogel, P. Schmidt-Wellenburg, N. Severijns, E. Wursten, J. Zejma, and G. Zsigmond, The European Physical Journal A **52**, 326 (2016).

[165] M. Daum, B. Franke, P. Geltenbort, E. Gutsmiedl, S. Ivanov, J. Karch, M. Kasprzak, K. Kirch, A. Kraft, T. Lauer, B. Lauss, A. Müller, S. Paul, P. Schmidt-Wellenburg, T. Zechlau, and G. Zsigmond, Nuclear Instruments and Methods in Physics Research Section A: Accelerators, Spectrometers, Detectors and Associated Equipment **741**, 71 (2014).

[166] S. Wlokka, P. Fierlinger, A. Frei, P. Geltenbort, S. Paul, T. Pöschl, F. Schmid, W. Schreyer, and D. Steffen, (2017), arXiv:1701.07431 [physics.ins-det] .

[167] F. Atchison, M. Daum, R. Henneck, S. Heule, M. Horisberger, M. Kasprzak, K. Kirch, A. Knecht, M. Kużniak, B. Lauss, A. Mtchedlishvili, M. Meier, G. Petzoldt, C. Plonka-Spehr, R. Schelldorfer, U. Straumann, and G. Zsigmond, The European Physical Journal A **44**, 23 (2010).

[168] J. J. Rush, D. W. Connor, and R. S. Carter, Nuclear Science and Engineering **25**, 383 (1966), https://doi.org/10.13182/NSE66-A18558 .

[169] P. Schmidt-Wellenburg, J. Bossy, E. Farhi, M. Fertl, K. K. H. Leung, A. Rahli, T. Soldner, and O. Zimmer, Phys. Rev. C **92**, 024004 (2015).